DISSERTATION

Titel der Dissertation

"Increased structural order in nanocomposites: From weakly linked nanoparticles in polymers to highly cross-linked strands in feather keratin"

Verfasserin

Mag. Silvia Pabisch, Bakk.

angestrebter akademischer Grad

Doktorin der Naturwissenschaften (Dr. rer. nat.)

Wien, 2012

"So once you know what the question actually is, you'll know what the answer means."
– Deep Thought, The Hitchhiker's Guide to the Galaxy

Abstract

Combining inorganic-organic phases on the nanometer range lead to nanocomposites with fascinating new properties. As nature uses this principle for millions of years, recent research adopts this to produce materials with enhanced optical, mechanical or magnetic properties.

One first important step was the characterization of the nanoparticles size and shape, as these parameters have a high influence on the structural and mechanical properties of the nanocomposites. Then, the capping agent molecules were varied in their components, the spacer length and the end group, to enhance the dispersion of the surface-functionalized nanoparticles within a polymer matrix. However, the crucial part was the investigation of the interaction and control of the interface between particles and polymer.

The size and size distribution of spherical, amorphous SiO_2 and crystalline, irregularly shaped ZrO_2, were determined by five different experimental methods to obtain the "true" size of the particles. The shape also plays a crucial role for the arrangement of the capping agent molecules attached to the nanoparticle's surface: It could be proven that alkyl chains formed self assembled monolayers on the surface of the crystal-faceted ZrO_2, which furthermore controlled the agglomeration of the nanoparticles due to a "zipper" effect with a neighboring particle. The ordering was continually disturbed by co-capping agents, investigated by the spectroscopic method FT-IR and correlated with the decrease of the tendency to agglomerate measured by the structural method SAXS.

Controlling the components of the capping agent allowed to investigate the complex interplay of nanofiller, surface-functionalization and polymer matrix and therefore to find an optimized system of nanocomposites with a homogeneous distribution of the nanoparticles. The addition of polymerizable end groups led to enhanced dispersion of SiO_2 in thermoplasts such as polystyrene and PMMA, whereas ZrO_2 modified with physically acting diethylene glycol chains exhibited a homogeneous dispersion in crosslinked polymers such as epoxy resin.

Surprisingly, structural measurements of a natural composite by folding one single protein, feather keratin, revealed a comparable structural control on the nanometer level: A long, flexible C-terminus, a crystalline β-core and a probably stiff N-terminus link the molecule to optimize mechanical properties. SAXS experiments revealed the stable structure of the keratin along the whole feather length and $in-situ$ experiments under load enabled a revised model of the keratin.

Zusammenfassung

Die Kombination anorganischer und organischer Phasen im Nanometerbereich führt zu Nanokompositen mit faszinierenden, neuen Eigenschaften. Die Natur nutzt dieses Prinzip bereits seit Millionen von Jahren, während die Forschung seit kurzem ebenfalls versucht, Materialien mit verbesserten optischen, mechanischen oder magnetischen Eigenschaften herzustellen.

Ein erster wichtiger Schritt war die Charakterisierung der Nanopartikelgröße und -form, da diese Parameter einen großen Einfluss auf die strukturellen und mechanischen Eigenschaften der Nanokomposite haben. Danach wurden die Oberflächenmoleküle in ihren Bestandteilen bezüglich der Länge und der Endgruppe variiert, um die Verteilung der oberflächenmodifizierten Nanopartikel im Polymer zu erhöhen. Der entscheidende Teil der Arbeit war jedoch die Untersuchung der Wechselwirkungen und der Kontrolle der Grenzfläche zwischen Partikel und Polymer.

Die Größe und Verteilungsbreite der sphärischen, amorphen SiO_2 und kristallinen, anisotropen ZrO_2 wurden mittels fünf verschiedener experimenteller Methoden bestimmt, um die "wahre" Größe der Partikel zu ermitteln. Die Form hatte ebenfalls einen Einfluss auf die Oberflächenmoleküle, welche an der Partikeloberfläche befestigt wurden: Es konnte nachgewiesen werden, dass sich Alkylketten als selbstanordnende Monoschichten an der Oberfläche der kristallinen ZrO_2 bilden, was wiederum dazu führt, dass sich Nanopartikel aufgrund eines "Reißverschluss"-Effekts mit einem Nachbarpartikel zu Agglomerationen formen. Die Ordnung konnte kontinuierlich durch Co-Oberflächenmoleküle gestört werden, was mittels der spektroskopischen Methode FT-IR untersucht und mit dem Ansteigen der Agglomeration, gemessen mittels der strukturellen Methode SAXS, korreliert wurde.

Die Komponenten der Oberflächenmoleküle zu kontrollieren, erlaubte die Untersuchung des komplexen Zusammenspiels zwischen Nanopartikel, Oberflächenfunktionalisierung und Polymer und damit ein optimiertes System eines Nanokomposits mit homogen verteilten Nanopartikel zu entwickeln. Die Hinzugabe polymerisierbarer Endgruppen führt zu einer verbesserten Verteilung der SiO_2 in Thermoplasten wie Polystyrol und PMMA, während mit physikalisch agierenden Diethylenglykolketten modifizierte ZrO_2 in quervernetzenden Polymeren wie Epoxidharz homogen verteilt waren.

Überraschenderweise enthüllten strukturelle Messungen eines Verbundwerkstoffes aus der Natur, entstanden durch die Faltung eines einzigen Proteins, dem Federkeratin, eine vergleichbare strukturelle Kontrolle auf der Nanometerebene: Ein langer, flexibler C-Terminus, ein kristalliner β-Kern und ein wahrscheinlich steifer N-Terminus verbinden einzelne Moleküle, um die mechanischen Eigenschaften zu optimieren. SAXS Experimente enthüllten die stabile Struktur des Keratins entlang der gesamten Feder und in-situ Experimente unter Belastung ermöglichten ein modifiziertes Modell des Keratins.

Contents

Contents

1 Introduction

1.1 Outline

The introduction gives an overview on the two main classes of investigated materials, the polymer nanocomposites as a material for technical applications and the biological material peacock feather. For the polymer nanocomposites, the effect of the surface-functionalization of the nanoparticles on the structural properties of the composite is investigated and optimized. For the biological material, nature already had millions of years of evolution to optimize the structure and uses different or even similar strategies in structuring biomaterials by simple proteins or complex hierarchical levels.

The experimental methods used in this work and their theory can be found in chapter 2. Small-angle X-ray scattering (SAXS) is mainly used for the characterization of the materials, as this technique is perfectly suited to investigate structures in the nanometer range, such as the polymer nanocomposites as well as the feather keratin. Additionally, several techniques such as transmission and scanning electron microscopy, dynamic light scattering and others, are introduced as they were used as complimentary methods to support the conclusions derived from SAXS.

The chapters 3 and 4 cover the investigations of nanoparticles in detail. Both types of nanoparticles, silica and zirconia, are characterized in chapter 3 by five different experimental techniques with the aim to investigate the effect of the inter-particle interaction on the size determination and therefore to determine the "true" size of the nanoparticles. Thereby, the advantages and disadvantages of these five methods are discussed in detail. This chapter is based on the publication Pabisch et. al., Chemical Physics Letters [S1]. In chapter 4, different surface-functionalizations of zirconia nanoparticles were developed, which led to self assembled monolayers (SAM). The order of the alkyl chains, measured by Fourier transform infrared spectroscopy, could be perfectly correlated to the agglomeration behavior of the whole nanoparticles, measured by SAXS. This study is based on the publication of Feichtenschlager et. al., Langmuir (in print) [S2].

In chapter 5, the surface-functionalized nanoparticles are incorporated in three different polymer matrices: polystyrene (PS), poly(methyl methacrylate) (PMMA) and epoxy resin and mainly characterized by small-angle X-ray scattering and transmission electron microscopy. The influence of the surface-functionalization on the dispersion of the nanoparticles in the polymer matrix is discussed in detail (chapters 5.1 and 5.3) as well as selected results from mechanical and thermomechanical

investigations of some of these systems are presented (chapters 5.2 and 5.4). The last part of this chapter, 5.4, which describes the effect of the surface-functionalized nanoparticles on the bulk properties of epoxy resin, is already published (Sajjad et. al., Polymer International [S3]).

The structure of feather keratin is discussed in chapter 6. This protein can be divided into three parts, the N-terminus, the hydrophobic core and the C-terminus, but only the hydrophobic core is visible in SAXS patterns due to its crystalline structure. This is similar to the nanoparticles used with capping agent molecules on the surface being nearly invisible in the X-ray due to their low scattering contrast. A scan along the whole length revealed the stable structure of the feather keratin. To find a revised model of this protein including N- and C-termini, tension, compression and rotation tests were carried out. The first part of this chapter, 6.1, is theme of the paper Pabisch et. al. in Journal of Structural Biology [S4].

Chapter 7 summerizes the investigations and results for the technical material, the polymer nanocomposites, and the biological material, the avian feather. The final conclusions of this work complete the last chapter.

1.2 Inorganic-organic nanocomposites

Traditional materials such as metals, ceramics or polymers can be more and more substituted by novel composites with superior physical properties. Such novel materials can fulfill similar duties as the traditional ones, but comprise additional functionalities like optical, electronic or magnetic properties. A well-known example for the need of these novel material class is the replacement of heavy weight materials by novel light systems and therefore a reduction of the rather high energy consume in transportation industry (e.g. airplanes) [1]. Here, the promising class of inorganic-organic nanocomposites comes into play, which incorporates inorganic building nanoblocks in an organic matrix [2, 3]. The reasons for the recent increasing interest in polymer nanocomposites can be summarized as follows [4]:

1. In the most cases, nanofillers have properties which are different from the bulk properties of the same material. This effect allows to design polymer composites with unique properties.

2. Nanofillers can be seen as small defects compared to micrometer-scale fillers, which are similar in size to the critical crack size causing early failure [5]. On the contrary, the smaller nanofillers can prevent early failure leading to materials with enhanced toughness and ductility [6].

3. Nanocomposites have a large matrix volume, which interacts with the nanoparticles and differs from the pure bulk polymer. The interfacial region between nanofillers and polymer chains can strongly influence thermal, mechanical and electrical properties of the composite.

According to the last point, the main characteristic of polymer nanocomposites is the small size and therefore the huge interfacial area of nanofillers in nanocomposites. It therefore provides an opportunity for the development of multifunctional composites with interesting properties. Transparent conduction polymer composites containing nanotubes are of high interest for the use as solar cell electrodes [7] as well as hybrid materials for protective or decorative coatings for widespread applications in painting industry, weather-resistant and scratch-resistant coatings [3]. Further examples are the use of inorganic-organic hybrid materials as filling composites in dental applications [3, 8] or for microelectronics and micro-optics [3].

While there are techniques to tailor the surface chemistry and structure of the nanoparticles, the influence of the nanofillers on the morphology, dynamics and properties of the surrounding polymer chains is still difficult to predict, even for complex computer simulations such as molecular dynamics or Monte Carlo simulations. This uncertainty is one of the great challenges in developing polymer nanocomposites for advanced technology applications [4]. An assumption for improved inorganic-organic nanocomposites is the need of a homogeneous dispersion of the nanofillers in the polymer matrix. This can be difficult due to the incompatibility of the different compounds. Therefore, chemical surface tailoring of the nanoobjects is necessary to enhance the dispersion and to obtain a highly homogeneous material. The nanofillers can basically interact in two different ways with the surrounding polymer matrix: physically or chemically (Figure 1.1) [9]. Figure 1.1a is an example for only physical interaction between the inorganic and organic compounds, which leads to different final materials properties in contrast to a strong chemical interaction between the compounds by covalent bonds as sketched in Figure 1.1b.
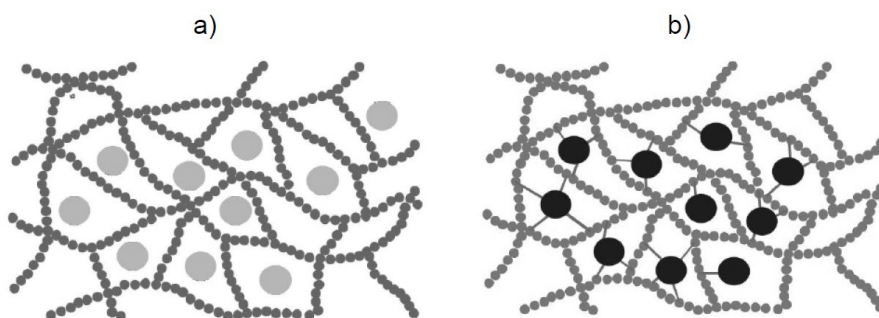

Figure 1.1: Inorganic nanoparticles (colored as light grey (left) and black (right)) are embedded in an organic polymer (grey chain). a) only physical interaction is present between the nanoparticle and the polymer chain, b) chemical interaction is given between the compounds via covalent bonds [9].

Coupling agent molecules are used for the chemical surface tailoring of nanofillers, which consist of an anchor group, an inert spacer and an end group as shown in Figure 1.2. The anchor group allows to stabilize the attachment of the organic moiety of this molecule to an inorganic surface. Examples for typical anchor groups and their corresponding substrates are alkoxy- and chloro silanes for SiO_2 (Figure 1.3, left) [10, 11, 12, 13], phosphonic acids for TiO_2, ZrO_2 (Figure 1.3, right) or Y_2O_3 [14, 15], carboxylic acids for Al_2O_3 [16] or sulfonic acids for SiO_2 or Fe_2O_3 [17] to name only the most common ones. The variety of anchor groups allows to control the strength of interaction to the surface of various inorganic compounds. The end group can be chemically inert or functional, which allows further chemical reactions [18]. For example, polymerizable end groups allow a covalent linkage between nanofiller and polymer chain and promote interfacial adhesion. The spacer between anchor- and end group can be varied in length to increase the compatability of the inorganic, in many cases hydrophilic, surface from oxide nanoparticles with hydrophobic media such as solvents or polymers. In many cases, alkyl chains are applied as the organic moiety for coupling agents.
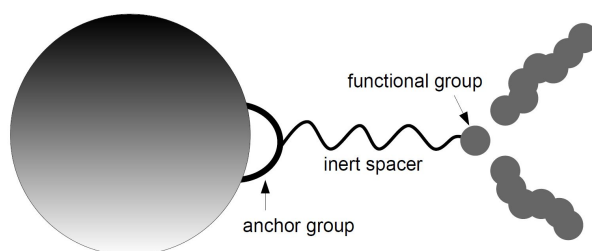
Figure 1.2: Scheme of a coupling agent molecule.
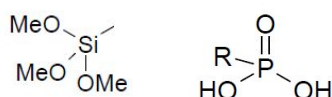
Figure 1.3: Anchor groups of trimethoxysilane for SiO_2 (left) and phosphonic acid for ZrO_2 (right).

1.3 Biological composites and biopolymers

Composite technology is also well-known in nature, as e.g. wood and bones are famous representatives of this materials class. These two biological materials possess the ability to adapt to possible changes in combination with the property of responsive behavior to their environment [19]. In summary, materials used by nature are limited in the availability of their constituents and their physical environment

during growth [20], which therefore also limits the number of adequate materials used by nature. Biopolymers, in many cases protein- and sugar-based polymers, several minerals and ions, or various crosslinking agents belong to nature's repertoire. Despite these limitations, biological materials possess a high variability in their properties: As example, toughness and stiffness are presented in Figure 1.4 [21], which are the result from various combination of biopolymers and minerals to form a composite material. Even if the constituents are entirely different, as it is the case for a number of materials such as cell walls, bone or keratin, both toughness and stiffness are high. This effect can be obtained through arranging or structuring the constituents at many hierarchical levels rather than chemical composition [22].

The biocomposites wood and bones are perfect examples for hierarchical structures in nature, from the molecular level to the tissue level. Wood starts with 2.5 nm thick cellulose microfibrils at the nanolevel, which are embeddded in a matrix of hemicellulose and lignin. This is the basic material of the cell wall, which is built up of several different layers.

In the case of bones, such as a human femur, this composite material consists on the nanoscopic scale of an organic phase, an inorganic mineral phase and water. The organic phase is built up of a protein in the form of a triple helix, the collagen type I, which is arranged in an aligned and staggered way and stabilized by covalent cross-linking between the collagen molecules [19]. The inorganic mineral phase, carbonated hydroxyapatite, is found in the form of platelets. In combination with the collagen, it builds up the mineralized collagen fibrils, which are glued together with a non-collagenous protein and proteoglycans.

But in nature, further hierarchical structures are used to fulfill a variety of different functions: Biopolymers [23]. Thereby, several building blocks (monomers) are provided as basis of biopolymers, which can be nucleotides, sugar and amino acids as shown in Figure 1.5. A well-known and well defined example of a linear biopolymer is DNA, built up by four individual nucleotides. One of the most versatile representatives of biopolymers are proteins, which are commonly composed of 20 different naturally occuring amino acids. Their specific arrangement allows to construct myriad of different proteins with unique properties. As proteins are poly(amino acid) chains, their amino acid sequence is known as primary structure (Figure 1.6) [23]. The local spatial arrangement of the polypeptide chains describes the secondary structure, which are α-helices and β-sheets in the most cases. The 3D arrangement of these secondary structures is defined as tertiary structure. In some cases, the assembly of individual proteins in supramolecular proteins leads to the quarternary structure.

For example, the well-known protein fiber collagen is a major component of skin, tendon and bone as mentioned above. Mammals have about 19 collagen varieties found in different tissues in the same individual. The mechanical properties of the materials are a direct consequence of collagen-content and -arrangement within the scaffold [24]. A further hierarchically structured protein, found almost exclusively
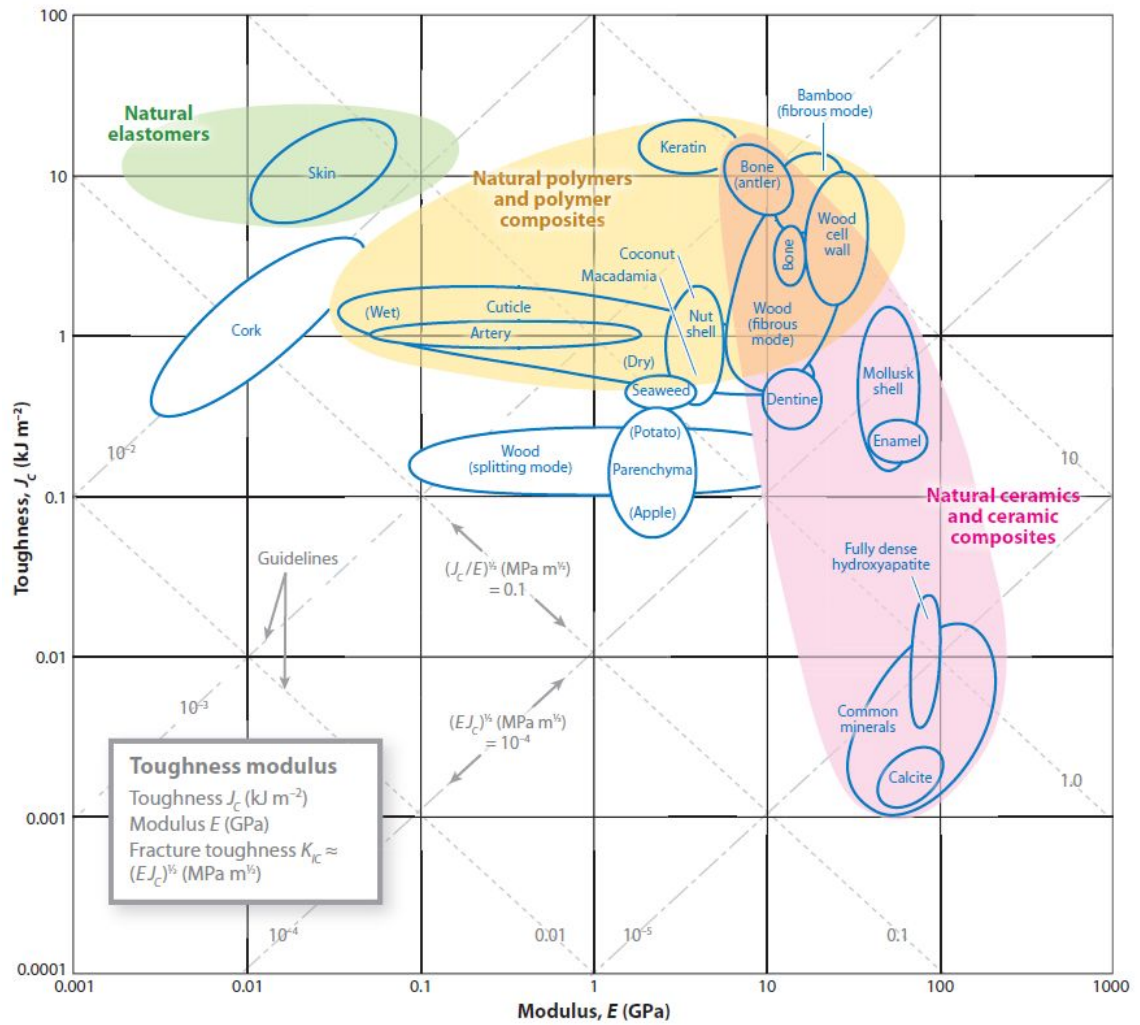
Figure 1.4: Relation between toughness and modulus for natural materials [21].

Figure 1.5: Common biopolymers and their appearence in nature as well as selected fibrous proteins [23].
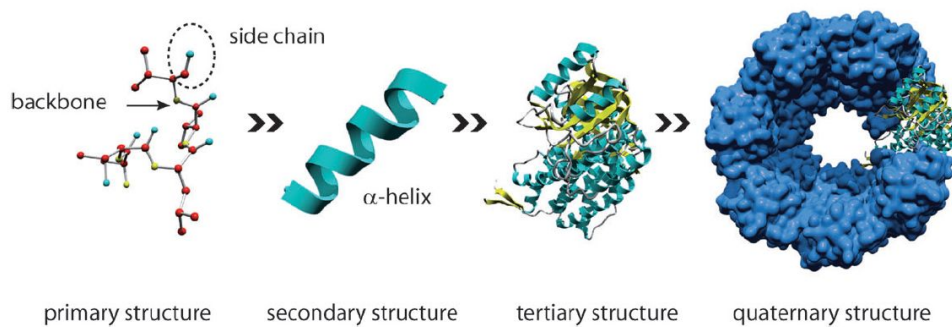
Figure 1.6: The hierarchical structure of proteins: Sequence of amino acid residues (responsible for subsequent folding processes) defines primary structure, local conformations such as α-helix or β-sheets are described by the secondary structure, the spatial 3D arrangement of an individual protein is its tertiary structure and the interaction of several proteins its quaternary structure (functional multimers) [23].

in mammals, is the proteinaceous fiber hair, where the helical protein keratin is the main component. As the α-form of the keratin is mainly found in mammals, where about 30 keratin variants expressed in a tissue-specific manner exist, the β-form can be seen as dominant secondary structure in the hard keratins of birds and reptiles [25, 26]. It is still debated whether α- and β-keratins are historically related or similar in structure and function. Their basic chemistry is similar, although the mechanisms differs and furthermore, β-keratins are smaller than α-keratins [27].

Protein secondary structure consists of the regular polypeptide folding patterns such as helices, sheets and turns [28]. The main chain of a protein, the backbone, includes the atoms that contribute to the peptide bonds, ignoring the side chains of the amino acids. The α-helix is right-handed and the arrangement of the backbone atoms, carbon, nitrogen, oxygen and hydrogen, results in a strong hydrogen bond as shown in Figure 1.7. Amino acid side chains are arranged around the backbone, projecting away from the helix, and thereby avoid steric interference with the polypeptide backbone and among themselves. The core of the helix is tightly packed, so that its atoms are in van der Waals contact. The α-helix, presented in Figure 1.7, is an example for this structure and explains a segment of sperm whale myoglobin. A further protein secondary structure, the β-sheet, also uses the full hydrogon-bonding capacity of the polypeptide backbone, however the hydrogen bonding occurs between neighboring polypeptide chains rather than within one polypeptide chain compared to an α-helix. Sheets can be found in two varities: the antiparallel β-sheet, where neighboring hydrogen-bonded polypeptide chains run in opposite direction, and the parallel sheet, where the hydrogen-bonded chains run in the same direction [28]. Figure 1.7 shows a six stranded antiparallel β-sheet from the jack bean protein *concanavalin A*.
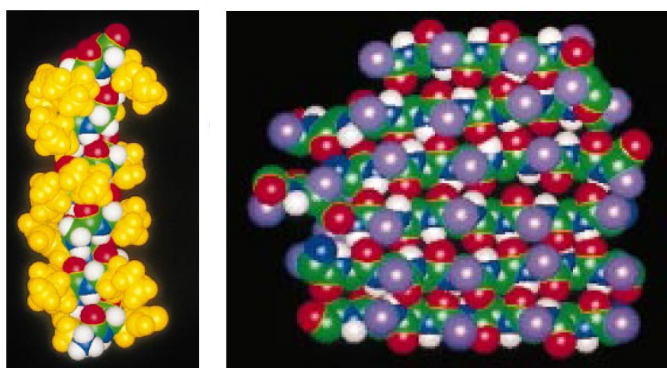
Figure 1.7: Space-filling models of an α-helix (left) and a β-sheet (right). The backbone atoms are colored with carbon in green, nitrogen in blue, oxygen in red and hydrogen in white. The side chains of the α-helix are yellow, whereas the R groups of the β-sheets are purple [28].

Historically, proteins have been classified as fibrous or globular, which depended

on their morphology. Fibrous proteins are characterize to often have a protective, connective or supportive role in living organisms. The already discussed collagen and keratin are highly elongated molecules, whose shapes are often presented by a single type of secondary structure. The springiness of hair and wool fibers is a consequence of the coiled coil arrangement of the α-keratin, as it tends to recover its original conformation after being untwisted by stretching [28].

Avian feathers are build up by a subclass of β-keratin, while avian claws and beaks are composed of another subclass, which is slightly larger than in feathers [27]. Although several studies were made about the structure of feather keratin [25, 29], the accurate arrangement of the keratin protein is still unknown.

1.4 Aim of this work

The aim of this work is to reveal the important role of a specific surface-functionalization to link a hard and a soft phase for mechanical and structural properties, both in technical composites such as polymers with nanoparticles or biological materials such as feather keratin.

For polymer nanocomposites, the characterization of the inorganic nanofillers shape and size is crucial, as these parameters play an important role in the composite system: Slight differences in size or shape can cause large differences in the structural or mechanical properties. After characterizing these parameters, the attention is turned to the surface-functionalization of the nanoparticles, especially the important role of the spacer length and the influence of polymerizable groups on the dispersion of the particles in different polymer matrices. The focus is therefore laid on the effect of different surface-functionalizations of nanoparticles on the structure of the polymer nanocomposites.

Additionally, mechanical and thermomechanical properties are determined to correlate them to the structure of the nanocomposites, which is proven by hardness tests and by the increase of the glass transition temperature.

For comparison with the insights obtained from the inorganic-organic nanocomposites, feather keratin with its crystalline hydrophobic core and its amorphous termini is characterized along the whole feather length by small-angle X-ray scattering to investigate the stability of the structure. The question has to be answered how the termini influence the structural and mechanical properties of the avian feather. Therefore, additional $in-situ$ experiments, tension and compression experiments as well as a rotation experiment, allow to define a revised model of the arrangement of the basic molecule to form an endless fiber in axial and different hierarchical levels in lateral direction.

2 Experimental section

Basic concepts of the experimental methods important for the work and their theoretical background are discussed in this chapter. Further, additional details to the methods and mathematical models for the respective material can be found in the chapters 3-6.

2.1 Wide angle X-ray diffraction

Structural analysis is based on diffraction techniques with X-rays, electrons and neutrons. In this work, it is focused on X-ray diffraction. Diffraction is produced by the interference of waves scattered by the periodic crystal and depends on the wavelength and the crystal structure. To determine the parameters of periodic lattices, two complementary theories can be used. The Bragg condition indicates that a maximum of intensity is achieved if every electron of the lattice plane becomes a source of a scattered wave and if the scattered waves positively interfere. Figure 2.1 shows a schematic drawing of the Bragg law, where the incident angle θ is consistent with the integer multiple of the path difference between the two beams [30].
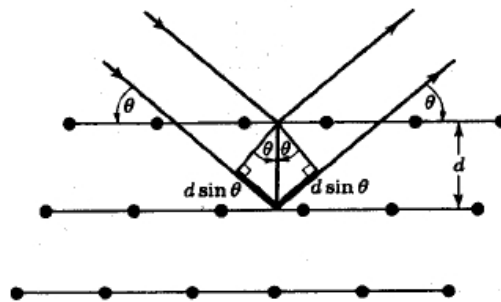
Figure 2.1: Scheme of the Bragg-reflection on the lattice plane [31].

From this follows Bragg's law

$$2d \cdot \sin\theta = m \cdot \lambda \tag{2.1}$$

with the lattice parameter d, the wave length λ and the integer number m. The Laue theory is independent of the imagination of lattice planes. In pursuance of

this theory the crystal is built up by identical microscopical objects like atoms or molecules, where the incident X-ray beam is scattered at these objects. Peaks are expected in certain directions and at constructively wavelengths, when the reflected waves of all lattice points interfere constructive. The condition for the constructive interference is derived by Laue and formulated as [31]:

$$\vec{q} \cdot (\vec{k} - \vec{k}_0) = 2\pi m \tag{2.2}$$

where $\vec{q}$ is the reciprocal lattice vector. Thereby, the difference between incident beam $\vec{k}_0$ and reflected beam $\vec{k}$ in Eq. 2.2, Δk, is equal a vector of the reciprocal lattice $\vec{q}$ (Eq. 2.3).

$$\vec{k} - \vec{k}_0 = \Delta\vec{k} = \vec{q} \tag{2.3}$$

This scattering condition is sketched in Figure 2.2 to illustrate the momentum transfer between photon and lattice, if the reciprocal lattice vector $\vec{q}$ is equal the difference of incident $\vec{k}_0$ and reflected beam $\vec{k}$ [31].
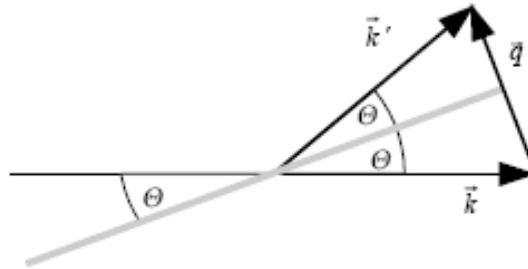
Figure 2.2: Momentum transfer between photon and lattice, if the scattering condition $\Delta\vec{k}=\vec{k}-\vec{k}_0=\vec{q}$ is fulfilled.

X-ray crystallography enables the determination of the arrangement of atoms within a crystal. In the case of powder X-ray diffraction (pXRD), the structural characterization of the powder sample is possible by the analysis of the angles and intensities of the diffracted beams. Usually, the diffracted intensity I is presented as function of the scattering angle 2θ or scattering vector q [32, 33]. To obtain the crystal structure of a material, the data function can be refined by the Rietveld method[1], where a theoretical diffraction pattern is generated to compare it with the observed data [34]. The height, width and position of the reflections gives information about several aspects of the materials structure. One example for a possible information obtained by the reflection is the crystallite size d as the diffracted beam

---

[1]The Rietveld method uses a least squares approach to refine a theoretical line profil to match the observed data.

is broadened when the particle size is small. Therefore, the correlation of the size d of crystallites with the peak broadening is given by the Scherrer equation [35]:

$$d = 0.9 \frac{\lambda}{\beta \cos \theta} \tag{2.4}$$

λ is the wavelength of the X-rays, θ the Bragg angle and β the calibrated breadth of a diffraction peak at half-maximum intensity, while 0.9 corresponds to the shape factor [32].

Diffraction contrast, using the Bragg condition, is also used in electron microscopes as a powerful tool e. g. for examining local strain fields in crystals.

2.2 Small angle X-ray scattering (SAXS)

Small-angle X-ray scattering (SAXS) is a powerful method to characterize the structure of materials at the nanoscale. It finds many applications in chemistry, [36] materials science, [37] or biology [38]. To detect larger lattice spacings, of the order of tens or hundreds of interatomic lattice distances, which is much larger compared to the X-ray wavelength, e. g. the CuK$_\alpha$-line with $\lambda = 0.1542$ nm, the angular range of the observable scattering has to be very small. As the scattering process is characterized by a reciprocity law, one obtains an inverse relationship between size and scattering angle [39]. The scattered intensity from the sample is typically measured in transmission as sketched in Figure 2.3, however, measuring the reflected intensity is also possible in GISAXS geometry, where the sample is almost parallel to the X-ray beam.
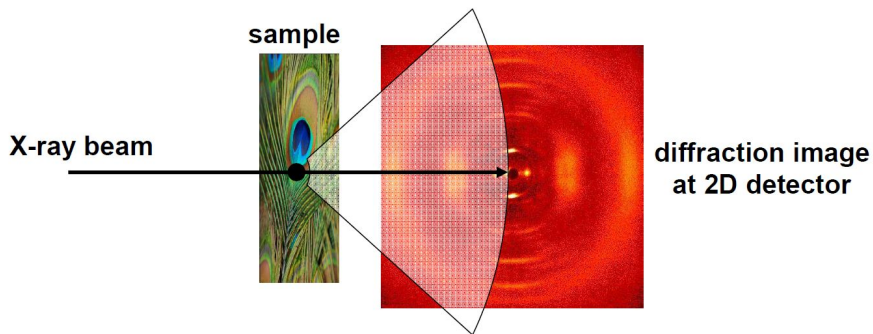
Figure 2.3: Scheme of a small-angle X-ray scattering experiment with a biomaterial in transmission.

SAXS pattern are typically presented as a function of the scattering intensity in dependence on the scattering vector

$$| \vec{q} | = \frac{4\pi}{\lambda} \sin \theta \tag{2.5}$$

with λ being the wavelength of the X-rays and 2θ the angle between incident X-ray beam and detector. The scattering process is caused by electron density inhomogeneities in the nanoscale within the sample [40]. The amplitude A of the scattering process, which cannot be measured experimentally due to the phase problem, is given by the scattering intensity $I(q)$

$$I(q,\chi) \propto |A|^2 \propto \left| \int \rho(\vec{r})e^{i\vec{q}\cdot\vec{r}}d\vec{r} \right|^2 \tag{2.6}$$

and contains the electron density $\rho(\vec{r})$. In the case of a two-phase material, the contrast leading to scattering arises from the difference of the electron densities of the two components $\Delta\rho$. Towards large q values, the scattering is caused by interface between the two phases and the intensity drops with the fourth power of q, assuming a sharp interface. This correlation is called Porod's law [40]:

$$I(q) = \frac{P}{q^4} \tag{2.7}$$

In the case of a two phase system with a fractal structure, the intensity slope can vary between q^{-1} to q^{-3} for a volume fractal or between q^{-3} to q^{-4} for a surface fractal. For a system consisting of a monodisperse collection of identical isotropic particles, the scattering intensity can be written as [36]

$$I(q) = I_0 N V_0^2 P(q) S(q) \tag{2.8}$$

where I_0 is a constant containing experimental parameters due to the setup of the experiment, N the number of primary particles, $V_0 = 4\pi r^3/3$ the volume of a primary particle, $S(q)$ the structure factor describing the particle-particle interaction and $P(q)$ the form factor of the particle. For very dilute systems, the structure factor is equal to 1. Then, the first approach to determine the particle size is the Guinier approximation [39]. The intensity at small q depends on the radius of gyration R_g of the particle and is described as [41]:

$$I(q) = I(0)e^{-\frac{(qR_g)^2}{3}} \quad \text{for} \quad q \to 0 \tag{2.9}$$

The form factor can be calculated by Fouriertransformation for a varity of different particle shapes. For a sphere with the radius R, the form factor can be analytically written as [39]:

$$P(q) = \left(3\frac{\sin qR - qR\cos qR}{(qR)^3} \right)^2 \tag{2.10}$$

The strong oscillations of the function by Eq. 2.10 are in general smeared out due to a size distribution of the particles. If the interaction of the particles cannot be neglected, a structure factor has to be introduced. In the literature, a hard-sphere

model with the expression for $S(q)$ calculated from the Percus-Yevick approximation [42] describes the interaction of particles with a hard-sphere radius R_{HS} and a hard-sphere volume fraction η:

$$S(q) = \frac{1}{1 + 24\eta G(A)/(A)} \qquad (2.11)$$

This equation was derived by Kinning and Thomas [43], where $A = 2R_{HS}q$ and $G(A)$ is given by:

$$\begin{aligned} G(A) = &\alpha \frac{\sin A - A\cos A}{A^2} \\ &+ \beta \frac{2A\sin A + (2 - A^2)\cos A - 2}{A^3} \\ &+ \gamma \frac{-A^4\cos A + 4((3A^2 - 6)\cos A + (A^3 - 6A)\sin A + 6)}{A^5} \end{aligned} \qquad (2.12)$$

with

$$\begin{aligned} \alpha &= \frac{(1 + 2\eta)^2}{(1 - \eta)^4} \\ \beta &= -6\eta \frac{(1 + \eta/2)^2}{(1 - \eta)^4} \\ \gamma &= \frac{\eta\alpha}{2} \end{aligned} \qquad (2.13)$$

For particle systems with anisotropy or polydispersity, other models have to be used. They are described in detail in chapter 3.

SAXS data can be evaluated either by direct modeling from fitting a mathematical model to the experimental intensities [39, 36] or indirect modeling as the Indirect Fourier Transformation (IFT) method introduced by Glatter [44, 45]. The latter one consists of the Fourier inversion of the experimental scattering curve, which provides the pair distance distribution function $p(r)$

$$p(r) = \frac{1}{2\pi^2} \int_0^\infty I(q) \cdot qr \cdot \sin qr \cdot dr \qquad (2.14)$$

The basic idea underlying this method is that it allows the evaluation of the particle-size distribution from the experimental data for uniformly shaped particles and offers also the possibility for the estimation of the radius of gyration comparable to the Guinier approximation [44].

2.3 Transmission electron microscopy (TEM)

Transmission electron microscopy (TEM) is a versatile tool for the characterization of materials with applications in materials science, biology, [46, 47] or nanotechnology [48]. An ultra thin specimen is investigated by a beam of electrons, which is

transmitted through the sample and thereby interacts with it. Figure 2.4 demonstrates the scheme of the complex buildup of a transmission electron microscope and its focusing mechanism. The wavelength of the electrons is given by the *de Broglie* wavelength as *de Broglie* showed that an electron can be treated as a quantum of an electron wave. As a consequence and due to the relation $E = h\nu$ for light quanta, which is also valid for electrons, the momentum $\vec{p} = m\vec{v}$ is also related by $\vec{p} = h\vec{k}$ to the wave vector $\vec{k}$ [49]. The limitations of the TEM image contrast are given by the adsorption of electrons in the material, due to the thickness and composition of the sample, as well as by technical limits such as the energy spread of the electron gun or the aberrations of the objective lens [49].
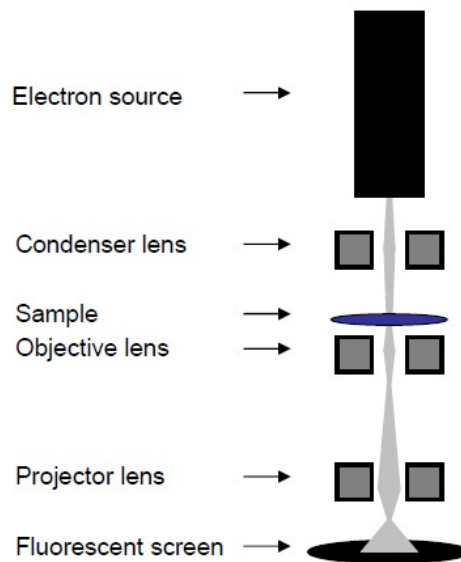
Figure 2.4: Scheme of the transmission electron microscope.

High-resolution transmission electron microscopy (HRTEM) uses the effect of a phase shift due to the interaction of the electron wave with the sample, as the incident beam is split up into a central beam and diffracted beams. This leads to a resolution at atomic scale and hence imaging individual atoms or crystalline defects can be observed [49].

It is also possible to obtain information from the diffraction of a selected area in crystalline materials (selected area diffraction - SAD). Conclusions about the crystalline structure can be made, as the diffraction patterns can be analysed analogous to X-ray diffraction patterns [49].

2.4 Scanning electron microscopy (SEM)

Scanning electron microscopy is used for the characterization of organic and inorganic materials from the scale of nanometer to micrometer. A scanning electron microscope (SEM) scans with a focused electron beam across the sample surface to collect images or focuses at one position for e. g. a chemical analysis. A schematic sketch of the buildup of a scanning electron microscope is presented in Figure 2.5. The interaction of the electron beam with the sample produces different types of signal, caused by the emission of secondary electrons, emission of characteristic X-rays or the backscattering of incident electrons [50]. The secondary electron emission, which results from the interactions of the electron beam with atoms at or near the sample surface, permits images at a resolution of nearly the size of the focused electron beam, which means in the size range of only a few nanometer. Back scattered electrons are beam electrons, which are reflected from the sample by elastic scattering, whereas characteristic X-rays are emitted in the case of a removed inner shell electron from the sample by the electron beam, which causes a higher energy electron filling the shell and releasing energy.
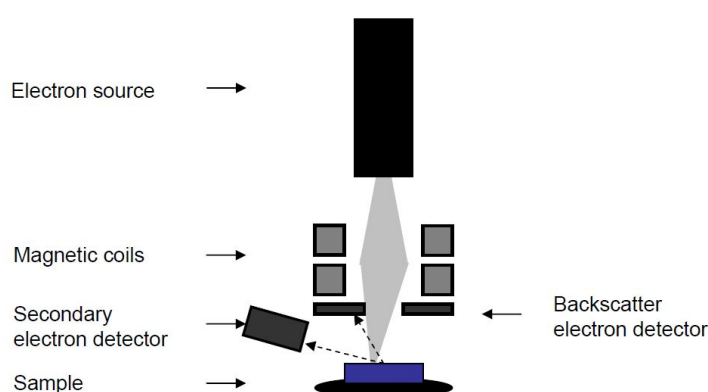
Figure 2.5: Scheme of a scanning electron microscope.

For imaging in the SEM, the samples have to be electrically conductive, at least at the surface, and electrically grounded to prevent accumulation of electrostatic charge at the surface. Nonconductive specimens such as biological materials tend to charge during the scan by the electron beam, which causes imaging faults. Therefore, these materials are coated with an ultrathin coating of electrically conducting material, which can be gold, gold/palladium alloy, graphite or others. Another possibility to avoid charging of a sample is measuring in near environmental conditions (ESEM).

2.5 Dynamic light scattering (DLS)

Dynamic light scattering allows a simple and fast determination of the radius of small particles in suspension or polymers in solutions [51]. This method has a broad range of further applications, but in this work the determination of the particle size distribution is of great interest.

A monochromatic light beam hits spherical particles, which rotate, translate and vibrate by virtue of thermal interactions. Because of this Brownian motion, the positions of the particles are constantlcy changing, so that the scattered intensity fluctuates in time [51]. Information about the dynamics of the particles is obtained from the autocorrelation of the intensity trace, which is defined as:

$$g_2(q, \tau) = \frac{\langle I(t)I(t+\tau)\rangle}{\langle I(t)\rangle^2} \tag{2.15}$$

Here, $g_2(q, \tau)$ is the autocorrelation function at a particular wave vector q and delay time τ and I is the intensity and measures the similarity between two signals $I(t)$ and $I(t+\tau)$. This function allows the determination of the size distribution [51]. By measuring the diffusion coefficient of the particle, the computation of the sphere size distribution and a description of the particle's motion in the suspension are possible. With the assumption of spherical particles, the Stokes-Einstein relation is used to calculate the hydrodynamic radius R_h:

$$D = \frac{k_B T}{6\pi\eta R_h} \tag{2.16}$$

D is the diffusivity, k_B the Boltzmann constant, T is the sample temperature in Kelvin and η the viscosity of the solvent.

2.6 Nitrogen sorption (BET)

The theory of Brunauer, Emmett and Teller [52] describes the physical adsorption of gas molecules on a solid surface and therefore is the basis for the measurement of the specific surface area of a material. The total surface area S_{total}

$$S_{BET,total} = \frac{\nu_m N s}{V} \tag{2.17}$$

and a specific surface area S

$$S_{BET} = \frac{S_{total}}{a} \tag{2.18}$$

ν_m ... monolayer adsorbed gas quantity (in volume units)
N ... Avogadro's number
s ... adsorption cross section of the adsorbing species

V ... molar volume of adsorbate gas
a ... mass of adsorbent (in g)

is evaluated from the experimental data. A particle radius can be calculated from the determined surface area with the assumption of a spherical shape. The technique of nitrogen sorption is also often used for porous solids to obtain information on the pore structure and pore diameters by measuring the sorption isotherms [53].

2.7 Fourier transform infrared spectroscopy (FT-IR)

Infrared spectra result from transitions between quantized vibrational energy states. Molecular vibrations can range from the motion of two simple coupled atoms of a diatomic molecule to the more complex motion of a large polyfunctional molecule. The number of vibrational modes of a molecule is given by the $3N$-6 degrees of freedom[2] [54]. The frequency of the oscillating motion around an equilibrium position is within the infrared region. This is the reason for using infrared radiation to excite vibrational motions resulting in a change in dipole moment [55]. Within the mid-infrared region (ca. 4000-400 cm^{-1}) first-order excitations of the vibrations of small parts of the molecule, the so-called functional group vibrations, can be found. For example, the stretching of the C-H bonds in a methyl or methylene group are included in the mid-infrared region containing the functional group vibrations.

2.8 Differential Scanning Calorimetry (DSC)

Differential scanning calorimetry (DSC) is a thermoanalytical technique using the difference in the amount of heat required to increase the temperature of a sample and reference when the sample undergoes a physical transformation such as a phase transition. Due to exothermic or endothermic processes changes in heat capacity are caused, which lead to more or less heat flow to the sample than to a reference sample to keep both at the same temperature. The difference in heat flow between sample and reference allows to measure the amount of heat absorbed or released during a phase transition and therefore to determine the heat capacity and hence the glass temperature T_g for polymeric materials.

---

[2]Molecules consisting of N atoms have 3N degrees of freedom minus three of the translational and three of rotational motion.

2.9 Hardness testing

The Vickers hardness test is an indentation method to measure the hardness of materials. It is based on the principle of the material's ability to resist plastic deformation from a standard source. The unit of the Vickers hardness test is known as the Vickers Pyramid Number (HV) and is determined according to the formula:

$$HV = \frac{1.854 \quad F}{d^2} \tag{2.19}$$

F   ... force
d   ... diagonal of the imprint

The corresponding unit of HV, kilograms force per square millimeter, can be converted into SI units by $9.81 \cdot HV[\frac{\text{kgf}}{\text{mm}^2}] = HV[\text{GPa}]$ to calculate Vickers hardness numbers.

3 Effect of interparticle interactions on size determination of zirconia and silica based systems – A comparison of SAXS, DLS, BET, XRD and TEM

The aim of this chapter is a systematic comparison of size characterization methods for two completely different model systems of oxide nanoparticles, i.e. amorphous spherical silica and anisotropic facet-shaped crystalline zirconia. Size and/or size distribution were determined in a wide range from 5 to 70 nm using small-angle X-ray scattering (SAXS), dynamic light scattering (DLS), nitrogen sorption (BET), X-ray diffraction (XRD) and transmission electron microscopy (TEM). A nearly perfect coincidence was observed only for SAXS and TEM for both types of particles. For zirconia nanoparticles considerable differences between different measurement methods were observed.

This chapter is based on the work Pabisch et. al. [S1].

3.1 Introduction

Nanoparticles are widely used in research and industry to tailor and improve materials properties, ranging from ceramics to polymers or biomedicine [1, 56]. An increasingly important research field is the incorporation of nanoparticles into an organic matrix to create inorganic-organic nanocomposites as a promising class of novel materials [2, 3]. Mechanical and physical properties of the resulting materials depend on the composition, shape, size and size distribution of the incorporated particles. Therefore, a precise determination of size and size distribution is a major challenge with regard to reproducibility and structure-property relations.

Among the methods used for the determination of the size and size distribution of nanoparticles, only a few are applicable in various chemical environments, i.e. small-

angle X-ray scattering (SAXS) and dynamic light scattering (DLS). One particular advantage of SAXS is that it can be used to analyze dispersions as well as powders or solids, whereas DLS is limited only to dilute solutions. Comparing SAXS with an image-guided method like transmission electron microscopy (TEM), SAXS benefits from a higher statistical quality in the size distribution determination within one measurement. Additionally, no high vacuum is required, which limits the samples many times to solid state samples [57]. On the other hand, TEM has its specific benefits as it delivers direct images and local information on size and shape of nanoparticles. Therefore, these two techniques are complementary and combining both methods can lead to superior information with regard to shape and size of nanoparticles in dispersions or powders [58]. An example for such combined studies is the kinetics of silica nanoparticle formation in various suspensions [59, 60]. Other types of particles investigated by SAXS, DLS and TEM were surface functionalized gold nanoparticles [61] and shell crosslinked nanoparticles [62]. These works further support the view that comprehensive information on particle size and shape require the use of more than one characterization technique.

A less common technique to obtain a particle size distribution is the analysis with nitrogen sorption. The evaluation according to BET theory (Brunauer-Emmet-Teller) [52] allows to obtain information on the size of non-agglomerated and dense particles [63, 64]. In many of the cited studies a good agreement between the different measurement techniques was found in particular for silica nanoparticles. Different to the high number of publications investigating silica, much less information is available for other oxides such as ZrO_2 nanoparticles. For this type of particles, DLS showed the stability of the aqueous suspension for several days and supplementary measurements by TEM and SAXS were performed to prove the structural composition of the ZrO_2 nanopowder [65]. The increase in size in dependence on the increasing calcination temperature was investigated for chemically coprecipitated zirconia powders with TEM, XRD, BET and SAXS [66]. As in most of the previous studies only one type of material was investigated, the idea of this chapter is to systematically compare a large number of characterization methods (SAXS, DLS, BET, XRD and TEM) in detail for two structurally completely different systems, one being amorphous spherical SiO_2 and the other crystalline irregularly shaped ZrO_2. The particles were synthesized under varying processing conditions to cover a wide size range from 5 to 70 nm.

3.2 Experimental Section

3.2.1 Materials

The solvents (HPLC grade) and chemicals were purchased from Sigma Aldrich and ABCR. Water was deionized before use. Methanol was purified using a PureSolv (Innovative Technology Inc.) solvent purification system. All chemicals were used

without further purification.

Synthesis of silica nanoparticles. Small silica nanoparticles were prepared applying a literature known procedure [67]. 100 mL Methanol were mixed with 29 mmol water and 0.17 mmol of 33 wt% aqueous ammonia solution. Afterwards 47.45 mmol tetraethyl orthosilicate were added dropwise under stirring in a 250 mL round bottom flask. The reaction mixture was then stirred at room temperature for 3 days. The solvent was evaporated and the remaining product was washed 3 times with n-hexane to destabilize the colloid within the washing step, separated by centrifugation at 4615 g and dried over P2O5 at 5 mbar resulting in 2.17 g white powder (each batch being in a diameter range between 5-10 nm according to SAXS). Larger silica nanoparticles were prepared by mixing 50 mL ethanol with 11 mmol water and 5 mmol of 33 wt% aqueous ammonia in a 250 mL round bottom flask [67, 68]. A solution of 50 mL ethanol mixed with 18.05 mmol tetraethyl orthosilicate was then added slowly under stirring. The reaction mixture was stirred at room temperature for 16 h. Then the solvent was evaporated and the remaining product was washed 3 times with n-hexane to destabilize the colloid, separated by centrifugation at 4615 g and dried over P2O5 at 5 mbar resulting in 0.86 g white powder (each batch being in a diameter range between 40-60 nm according to SAXS).

Synthesis of zirconia nanoparticles. Small zirconia nanocrystallites were prepared applying a literature known procedure [69]. 13 mL of a 4 M solution of ZrOCl2 were thermally decomposed in water in an autoclave with a 20 mL-teflon-inlay at 200°C. The reaction was carried out for 3 days and the particles were isolated by precipitation with acetone and centrifugation at 4615 g, washed with a mixture of water and ethanol (1:5) three times and dried over P2O5 at 5 mbar to yield 3.50 g of a white powder (each batch in a diameter range between 5-10 nm according to SAXS). Powder-XRD: 100% crystalline ZrO2, Baddeleyite phase (monoclinic). Larger zirconia nanocrystallites were prepared by a procedure described in literature [70] under hydrothermal conditions. A mixture of 19 mmol H2O, 7.3 mmol acetic acid and 2.25 mmol Zr acetate solution (16 wt% in acetic acid) was heated in an autoclave with 20 mL-teflon-inlay for 16.5 h at 170°C. The resulting stable particle-dispersion was then destabilized by removing two thirds of the volume by evaporation and adding 10 mL acetone. The product was separated and washed 3 times with a mixture of acetone:water = 10:1 (centrifugation at 6150 g), then dried over P2O5 at 5 mbar to give 0.71 g of a white powder (each batch in a diameter range between 20-30 nm according to SAXS). Powder-XRD: 100% crystalline ZrO2, Baddeleyite phase (monoclinic).

3.2.2 Measurement techniques

Powder-XRD-measurements were carried out on a Philips X'Pert Pro instrument at Cu K$_{alpha}$ - radiation with a Bragg-Brentano-arrangement with an angle speed of 6°/min where the sample was carried on Si-single-crystal-wafers under ambient

conditions. Crystallite size was calculated using the TOPAS software via refinement using 5 metric parameters. The average crystallite size D was determined from the broadening of the peaks by Scherrer's equation $D = 0.9\lambda/(\beta \cos\theta$, where λ is the wavelength of the X-rays, θ the Bragg angle and β the calibrated breadth of a diffraction peak (here the (111) reflection) at half-maximum intensity.

Nitrogen sorption measurements were performed on a Micromeritics ASAP 2020 instrument. The samples were degassed under vacuum at 60°C for at least 8 h prior to measurement. The surface area was calculated according to Brunauer, Emmett and Teller (BET) [52].

Dynamic light scattering (DLS) measurements were carried out by non-invasive backscattering on an ALV/CGS-3 compact goniometer system with an ALV/LSE-5003 and a multiple tau correlator at a wavelength of 632.8 nm (He-Ne Laser) and a goniometer angle of 90°. The dispersing media were purified before use with a syringe-filter (200 nm mesh). The determination of the particle size was carried out by the analysis of the correlation-function via the g2(t) method followed by a linearized number-weighting (n.w.) and mass weighting (m.w.) of the distribution function.

SAXS measurements were performed under vacuum using a rotating anode X-ray generator with a pinhole camera (Nanostar, Bruker AXS) with Cu K_{alpha} radiation monochromatized and collimated from crossed Goebel mirrors and detected by a 2D position sensitive detector (Vantec 2000). The sample-to-detector distance was varied from 13 cm to 108 cm to cover a wide range of the scattering vector q from 0.1-15 nm^{-1}. All SAXS patterns were radially averaged and corrected for background scattering to obtain the scattering intensities in dependence on the scattering vector $q = 4\pi/\lambda \sin\theta$, where 2θ is the scattering angle and $\lambda = 0.1542$ nm the X-ray wavelength.

TEM images were recorded on a JEOL JEM-100CX and on a FEI TECHNAI G20 transmission electron microscope at the University Service Center for Transmission Electron Microscopy, Vienna University of Technology. The particle powder samples were attached to Formvar copper grids by dispersing them in ethanol using a ultrasound cleaning bath, adding one drop on the copper grid and evaporating the solvent. The images were evaluated automatically by the software ImageJ [71] or manually in the case of a very low contrast. At least 50 particles were measured for each size and type of particle and spherical equivalent diameters were evaluated.

3.3 Theory

DLS primarily measures time-dependent fluctuations of scattered coherent light, i.e. the decay of the autocorrelation function, which is caused by diffusive motion of the particles. The experimentally measured diffusion coefficients can be converted to a hydrodynamic radius via the Stokes-Einstein equation 2.16 [72].

In contrast to dynamic light scattering, SAXS probes differences in electron den-

sities. To get information on the size and arrangement of nanoscaled objects from SAXS data, either direct methods (from fitting the purely mathematical Fourier transforms to the intensities) [36, 39] or indirect methods (which intend to restore the distribution function in real space from SAXS data) are available [73, 74, 75]. In this paper, we focus on the first ones, where the scattering intensities of weakly ordered structures are described in the monodisperse model by the product of form factor and structure factor, $I(q) = I_0 V_0^2 P(q) S(q)$, with q being the absolute value of the scattering vector, V_0 the volume of the particle, $S(q)$ the structure factor and $P(q)$ the form factor. I_0 contains experimental parameters such as the scattering contrast, the beam intensity and additional variables due to the setup of the experiment. In the case of polydispersity, the simplest approach is a formal factorization with a mean form factor and to replace the structure factor by a so-called effective one [76].

$$I(q) = I_0 V_0^2 \bar{P}(q, r) S_{eff}(q) \tag{3.1}$$

In the case of a Gaussian size distribution of spherical particles, the form factor is given by

$$\bar{P}(q) \propto \int \mathrm{d}\, R \left(\frac{4\pi}{3} R^3 \right)^2 exp \left(-\frac{1}{2} \frac{(R-r)^2}{\sigma^2} \right) \left(3 \frac{\sin qR - qR \cos qR}{(qR)^3} \right)^2 \tag{3.2}$$

In the case that the distribution is sufficiently small, the integral can be extended from minus infinity to infinity and its analytical solution is given in the section 3.7.

For hard spheres, the Percus-Yevick approximation [42] delivers a structure factor for weakly aggregated systems, which describes the interference of the scattering of particles with two parameters, a hard-sphere radius R_{HS} and a mean hard-sphere volume fraction η [43, 77]

$$S(q) = \frac{1}{1 + 24\eta G(2R_{HS}q)/(2R_{HS}q)} \tag{3.3}$$

with the function $G(2R_{HS}q)$ being defined by Kinning and Thomas [43]. The hard-sphere radius R_{HS} gives information on the correlation distance of particles within a cluster or an aggregate and the hard-sphere volume fraction η on the probability to find particles in vicinity to each other.

To describe the effect of a small anisotropy of the particles on the scattering intensity, their interaction can be assumed to be independent of their orientation and is given by their average size [74]. Therefore, the decoupling approximation can be used [78]

$$I(q) = I_0 V_0^2 P(q, r)(1 + \beta(q)(S(q) - 1)) \tag{3.4}$$

where $\beta(q) = \langle F(q) \rangle_0^2 / \langle F^2(q) \rangle_0$ with an orientational averaged form factor $P(q) = \langle F^2(q) \rangle_0$ [78]. In the case of polydispersity, the equations are similar, but the orientational average has to be replaced by an integral taken over the size [77, 78]. For including the effect of larger polydispersity, the local monodisperse approximation

is frequently used [77, 79]. It is based on the assumption that a particle of a certain size is always surrounded by particles with the same size. Therefore, the model consists of monodisperse sub-systems weighted by the size distribution

$$I(q) \propto I_0 \int dR V_0^2(R) F^2(q, R) S(q, R) \tag{3.5}$$

An overview on the different theoretical models is discussed in the literature [77].

Different to Eq. 3.2, an unified equation for the form factor has been proposed by Beaucage [80, 81, 82, 83], consisting of a Guinier like and a limited power law regime.

3.4 Results

Figure 3.1a shows the scattering intensities from XRD for silica nanoparticles with the strong short range order peak from the distance of the silica tetraeder, Figure 3.1b for the zirconia nanoparticles, with broad Bragg reflections typical for nanoparticles. Rietveld refinement revealed a composition of the zirconia nanoparticles of about 100 % crystalline monoclinic ZrO_2 (Baddeleyite). The crystallite size was determined to be 4.5 nm for small ZrO_2 and 2.9 nm for large ZrO_2 as evaluated from the Scherrer equation with an estimated standard error of ten percent. The surprisingly smaller value for the large ZrO_2 nanoparticles suggests that they are built up as aggregates from smaller particles, which is supported by the TEM-images (Figure 3.2).
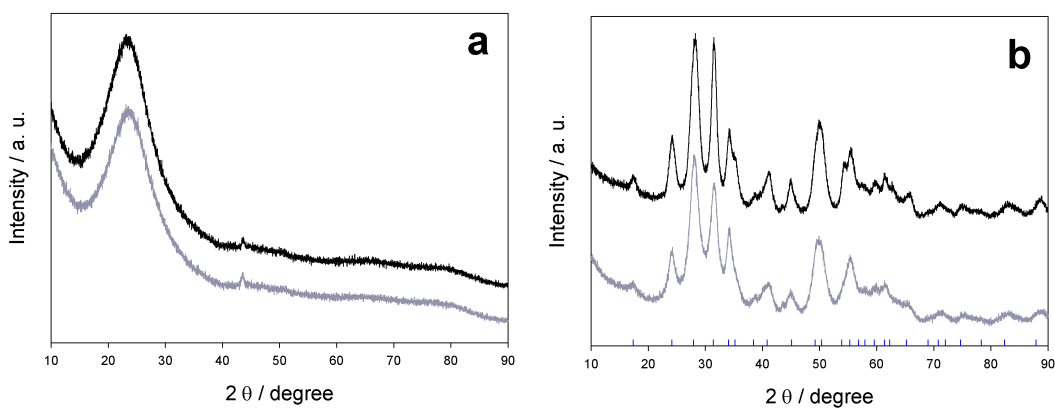

Figure 3.1: XRD of a) silica, (black: 4.3 nm and grey: 53.4 nm) and b) zirconia samples: 4.0 nm (black) and 33.8 nm (grey) nanocrystallites, diameter from SAXS evaluation.

In these TEM images it is clearly visible that small zirconia particles consist of crystal-facet-shaped nanocrystals (Figure 3.2a), whereas the large zirconia particles

(Figure 3.2b) are built up of aggregates of smaller units. The crystallinity is also observed in the inserts of Figure 3.2, the selective area diffraction (SAD-) images. Together with HRTEM images (Figure 3.3) the conclusion from XRD is further confirmed that small nanoparticles are single crystallites and larger ones are poly-crystalline aggregates, visible by the presence of different lattice fringes of every single crystallite in the aggregate (HRTEM images, Figure 3.3b). Different to the complex shape of zirconia, the silica nanoparticles exhibit a distinct spherical shape (Figure 3.2c). Small silica particles reveal a poor contrast to the carbon coated copper grid in the TEM micrographs and are therefore not shown.

Figure 3.2: Representative TEM micrographs of a) small ZrO_2 nanoparticles of a size of 3.8 nm, b) large ZrO_2 nanoparticles (15.2 nm) and c) large SiO_2 nanoparticles (53.5 nm), diameter from SAXS evaluation. Selective area electron diffraction images are displayed in a) and b) to confirm the crystallinity.
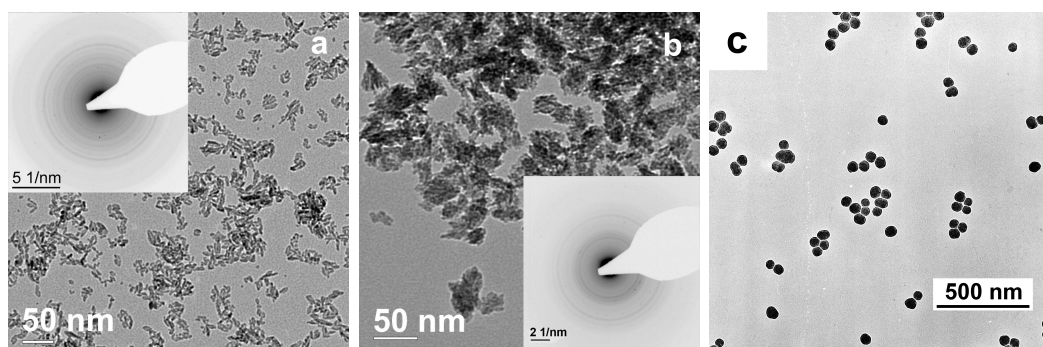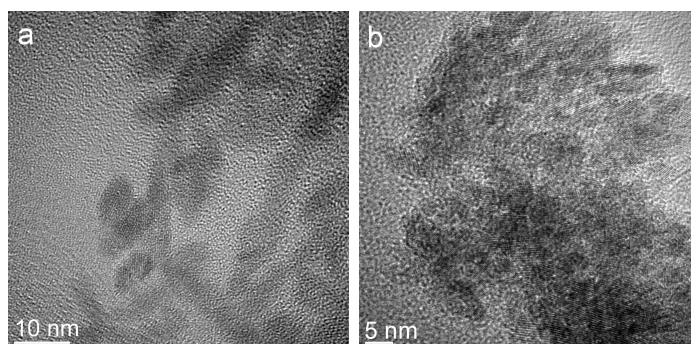

Figure 3.3: Representative HRTEM micrographs of a) small ZrO_2 nanoparticles of a size of 3.8 nm and b) large ZrO_2 nanoparticles (15.2 nm), diameter from SAXS evaluation.

DLS was used to determine the number-weighted and the mass-weighted particle size distribution of the nanoparticles dispersed in ethanol (SiO_2) and water (ZrO_2).

According to these DLS-measurements, the number-weighted size distribution of the nanoparticles is rather uniform as shown in Figure 3.4 (data and figure for mass-weighted evaluation are found in chapter 3.7). For the samples presented in Figure 3.4, particle diameters of 7.8 ± 2.3 nm for small and 64 ± 12.8 nm for large silica, furthermore 17.8 ± 3.6 nm for small and 54 ± 10.8 nm for large zirconia were measured with DLS.
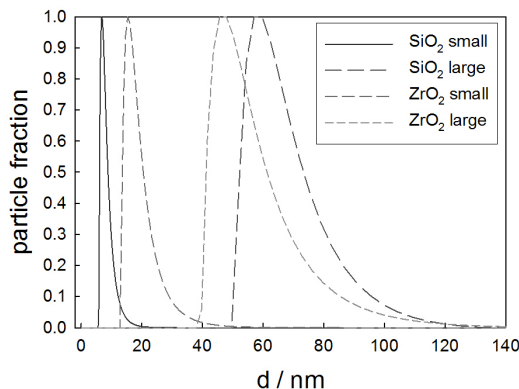

Figure 3.4: Typical number-weighted particle diameter distributions from DLS for the respective nanoparticle powder dispersed in ethanol (SiO_2, diameter from SAXS evaluation 4.4 and 53.4 nm) or water (ZrO_2, SAXS: 4.0 and 33.8 nm).

For comparison to nitrogen sorption, two batches for each oxide were measured. With the assumptions of a spherical shape and a complete coverage of the surface with nitrogen molecules, one may derive the particle size distribution. The value for the specific surface area was 710.6 ± 7.1 m^2/g for small and 76.2 ± 0.8 m^2/g for large SiO_2 nanoparticles. As a consequence of the lower specific surface of the large SiO_2 nanoparticles, this results in a smaller size of only 34 nm compared with the size of 53.4 nm from SAXS evaluation. Differently, the specific surface for large ZrO_2 nanoparticles is higher than for small ones, i.e. 171.1 ± 1.7 m^2/g in comparison to 140.3 ± 1.4 m^2/g. This would indicate a smaller size. However, taking into account the results from TEM and SAXS, this can also be attributed to polycrystalline aggregates, which build up the large ZrO_2 nanoparticles.

For each of the batches of nanoparticles prepared, SAXS patterns were collected and fitted by different models with the software Mathematica$^{\text{TM}}$. The form factor was obtained either by spheres with a Gaussian size distribution and an effective structure factor, Eq. 3.2 to Eq. 3.3, or the Beaucage model with a lognormal distribution (Eq. 3.6 to Eq. 3.7 shown in chapter 3.7). Using the decoupling (Eq. 3.4) or the local monodisperse approximation (Eq. 3.5) led to fit parameters, which did not differ considerably from the ones of the simple model with an effective structure factor (shown for selected examples of silica as well as zirconia nanoparticles in chap-

ter 3.7). For the Gaussian model, the number length-weighted, the number-weighted as well as the mass-weighted diameter mean, $d_{1,0}$, $d_{3,0}$ and $d_{4,3}$, were calculated [84]. For comparison of the methods, in the following diagrams the number-weighted mean $d_{3,0}$ was chosen and is denoted as d_{SAXS}. Numerical values are also listed in chapter 3.7: There are certainly some general trends - the relation $d_{4,3} > d_{3,0} > d_{1,0}$ holds due to the different weight of the distribution and the Beaucage model gives slightly larger values than the Gaussian sphere model - however, the deviation between different evaluation methods is within about 30 percent at maximum.

For large zirconia particles, two levels of hierarchy are visible as two characteristic humps in the scattering intensities and were therefore fitted with a system with two different radii, i.e. a bimodal size distribution. To our interpretation, the second maximum at large q-values arises from small crystallites building up a porous aggregate, as just mosaic crystals with grain boundaries would not have sufficient electron density contrast to give a second maximum. A typical short range order distance of 2.7 nm is observed in SAXS, which is similar to the size of 2.9 nm as obtained from XRD.

The stronger tendency to agglomerate is visible from the more pronounced scattering intensity maximum in particular for small silica (Figure 3.5a). This higher intensity leads to a higher numerical value for the volume fraction η in the hard-sphere model, Eq. 3.3. The higher the hard sphere volume fraction, the higher is the probability to find in the vicinity of a particle another neighbouring one.
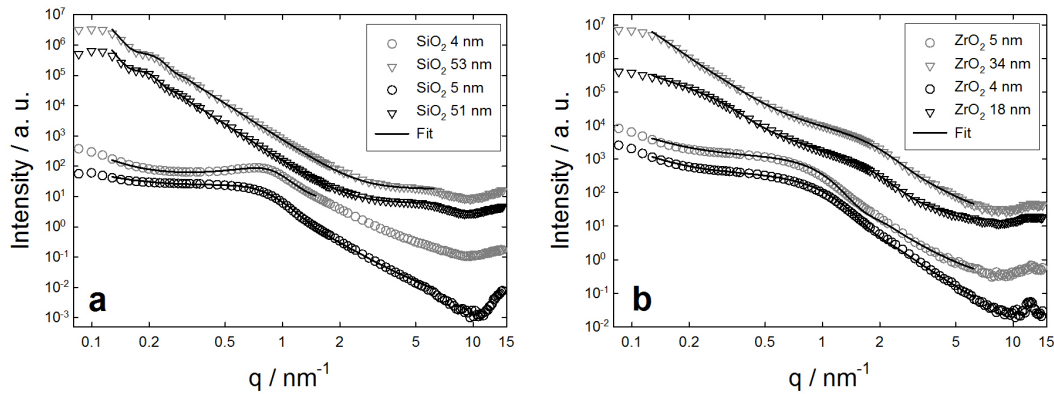
Figure 3.5: Experimental SAXS profiles $I(q)$ (symbols) and fitting curves (solid lines) of small and large a) silica and b) zirconia using the analytic approach with spheres and a Gaussian size distribution and an effective structure factor (Eq. 3.3). The profiles are shifted vertically for better visibility.

The results for the diameter and the distribution width (standard deviation) of the different nanoparticles obtained from the respective measurement technique are presented in Figure 3.6 (TEM, filled squares, DLS, circles, BET, triangles, XRD,

diamonds, only for zirconia), in dependence on the particle diameter $d_{3,0}$ obtained from SAXS. For BET and XRD, only the size but not the distribution width is given, but for both methods a measurement error of at least ten percent is estimated. A complete list of the numerical data is found in chapter 3.7.
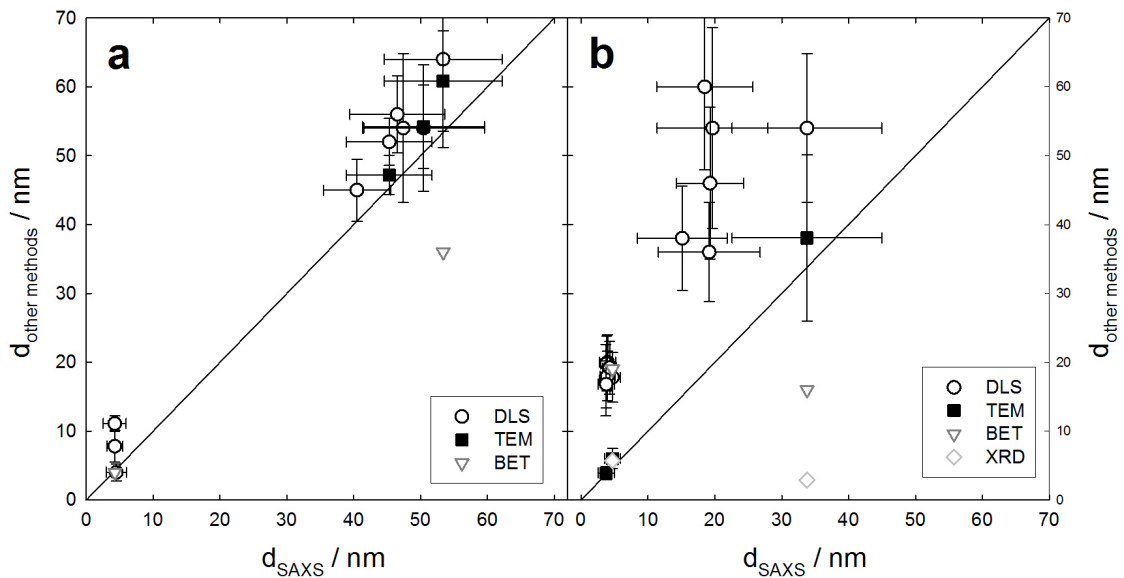
Figure 3.6: Particle diameter and distribution width (standard deviation) from DLS (circles), TEM (filled squares), as well as particle diameter from BET (triangles) and XRD (diamonds, only for zirconia) in dependence on the particle diameter obtained from SAXS, d_{SAXS}: a) silica and b) zirconia nanoparticles.

3.5 Discussion

Each of the techniques has its specific advantages: TEM delivers direct images, from which information on size and shape of nanoparticles is obtained, SAXS is able to measure powders, solids, and also particles in solution, DLS is a fast and cheap method to measure a high number of samples, and XRD and BET give the size of nanoparticles as a by-product from the main aim of the method, e.g. the determination of phases within a sample or the specific surface.

For silica nanoparticles, all presented experimental methods give a nearly perfect agreement (Figure 3.6a), with the exception of BET for large silica nanoparticles. A possible explanation could be microporosity, as micropores were sometimes found

in large Stöber silica particles [17]. DLS gives slightly larger values, but within the error bars, which is probably due to the hydrodynamic shell. None of the typical difficulties reported in the literature for TEM might have had an effect, such as aggregation by capillary forces between the particles during drying [85], or a collapse of highly hydrous and open-structured silica particles due to the dehydration and relaxation processes under high vacuum [59]. Whereas in TEM one has to take care about magnification, imaging type and analysis method, which can affect the resulting size distribution, especially in case of small nanoparticles [86], the difficulty in SAXS is that the method relies on mathematical modelling of scattering intensities, where the choice of the respective analytical or numerical approach is not always unique. The upper size limit of SAXS in the laboratory is about 50 nm, and larger objects require USAXS at a synchrotron radiation source. Nevertheless, SAXS agreed well with the other methods, as the typical oszillations in the scattering intensities from the narrow size distribution of silica nanoparticles allowed a precise measurement up to the 50 nm regime.

Differently, zirconia nanoparticles (Figure 3.6b) exhibited a considerable discrepancy. Whereas SAXS and TEM are close to each other, the size of zirconia nanoparticles from DLS exceeds SAXS and TEM by a factor of two to three. The significantly larger value from DLS might be attributed to the larger hydrodynamic shell, which probably is dependent not only on the composition (the larger coordination sphere of zirconia), but also on the shape and roughness of the particle. A complex shape of particles [87] as well as their interaction [88] could influence the numerical evaluation from DLS. Also even a small amount of 1-2 vol% of larger particles can significantly change the DLS derived particle size distribution, whereas SAXS measurements are less susceptible to the presence of larger aggregates [59].

Furthermore, a higher tendency to agglomerate was observed for silica in comparison to zirconia nanoparticles. A possible cause is that the surface energy and surface charge of silica nanoparticles is relatively high and agglomeration leads to a reduction of surface and gain in enthalpy. The enthalpy is one of the crucial parameters controlling the dispersion of nanoparticles in polymers [89]. As the aqueous dispersions of zirconia particles have a pH of 4 (large) and 2.9 (small), it is also proven that the zeta potential of the dispersion of zirconia particles is electrostatically stable until pH of 7 (see chapter 3.7). This electrostatic stabilization is responsible for the good dispersion quality of zirconia nanoparticles in water used in this work.

The results from BET coincide with the results from SAXS, TEM and DLS only for small silica nanoparticles and deviate for large ones, whereas for zirconia a considerable difference was found for small as well as large nanoparticles. This is attributed in the latter case mainly to effects of a rough and porous surface, which is obviously the case for the large zirconia particles. Furthermore, small nanoparticles lead to a high surface area and any mixture of particles of different size is dominated by the specific surface area of the small particles [66]. The existence of more than one type of porosities in large nanoparticles cannot be excluded, as the isotherm type can be

classified to be between type II and IV using the IUPAC classification of nitrogen sorption isotherms [90] and the hysteresis is not of uniform shape (H1-H2 mixed with H3). Differently, in small nanoparticles only mesopores are present, as they exhibit type IV behavior with H1 hysteresis (typical isotherms of nitrogen sorption are found in chapter 3.7). This might be the reason for the good agreement of the size from BET to the other methods for small as well as the huge difference for large nanoparticles.

XRD could only be applied to zirconia nanoparticles due to the crystallinity of the latter. It coincides only for small zirconia, which is attributed to the observation that large zirconia nanoparticles are built up of smaller crystalline units. It is therefore natural that the measured diameter from XRD reflects the size of the small crystallites and not the one of the nanoparticle aggregate.

3.6 Conclusion

Two oxide nanoparticle systems, amorphous SiO_2 and crystalline ZrO_2, were studied by DLS, SAXS, TEM, BET and XRD (only for crystalline ZrO_2). SAXS and TEM are in nearly perfect agreement for both materials in the whole measured range covering a nanoparticle diameter from 5 to 70 nm. BET shows large deviations in case of the large silica nanoparticles and is not applicable to zirconia due to the irregular shape and the high surface roughness of the latter. DLS leads to a slightly higher value for the size within the error bars for silica and considerably higher values for zirconia nanoparticles compared to TEM and SAXS. This is attributed to the influence of the hydrodynamic shell, and is more pronounced for facet-shaped zirconia than for spherical silica. XRD can only be used for crystalline materials and gave a reasonable size only for small zirconia, but clearly not for large zirconia nanoparticles, which were polycrystalline aggregates. In conclusion, one should be careful with the interpretation of numerical values of the size of nanoparticles from different methods, as not only the type of material, but also its shape and porosity might have a considerable influence. An approach using not only one single measurement method is favourable to obtain general information on size, size distribution and shape of nanoparticles.

3.7 Supplementary Information

Zeta potential for zirconia

The aqueous dispersions of zirconia particles had a pH of 4 (large) and 2.9 (small), which is well below the limit of stability of pH of 7, as shown by the zeta potential measurement in Figure 3.7.
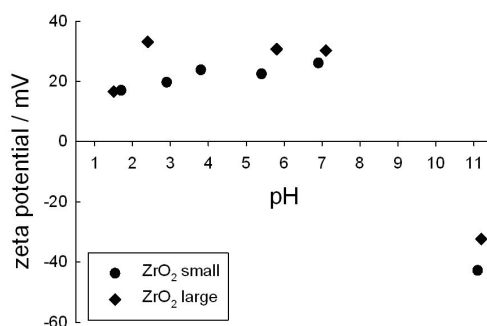
Figure 3.7: Zeta potential for small (circles) and large (diamonds) zirconia to determine the isoelectric point.

Isotherms of nitrogen sorption experiments

The isotherm type of the large nanoparticles (Figures 3.8b and 3.8d) can be classified to be between type II and IV, which is an indication that macro- and mesopores are present. Also the hysteresis is not from uniform shape (H1-H2 mixed with H3). This leads to the conclusion that in the case of the larger particles probably two types of porosity are present. Assuming that one type of porosity is created by the space between the packed particles, the other type should come from the particle itself. The isotherms for the small ZrO_2 and small SiO_2 (Figures 3.8a and 3.8c) were of type IV with H1 hysteresis. From the shape of these isotherms it can be concluded that only mesopores are present, and the existence of micro- or macropores can be ruled out. These mesopores result from the packing of the particles and are uniform in size.

Mass-weighted and number-weighted particle size distribution by DLS

The results for the nanoparticle size depend on the evaluation method, whether a mass-weighted (Figure 3.9) or number-weighted (Figure 3.4 of the article) particle size distribution is calculated. Mass-weighted evaluation is susceptible to larger particles or aggregates of particles whereas number-weighted evaluation takes account of the number of single particles at similar size and is less influenced by aggregates. Both methods show monodispersity. In general, there is the tendency that the size obtained from the mass-weighted evaluation is higher than the one from the number-weighted evaluation (see Table 3.1).

Complete list of data for the different methods

Diameter and distribution width (standard deviation) of the different nanoparticles obtained from the respective measurement technique are presented in Table 3.2. For
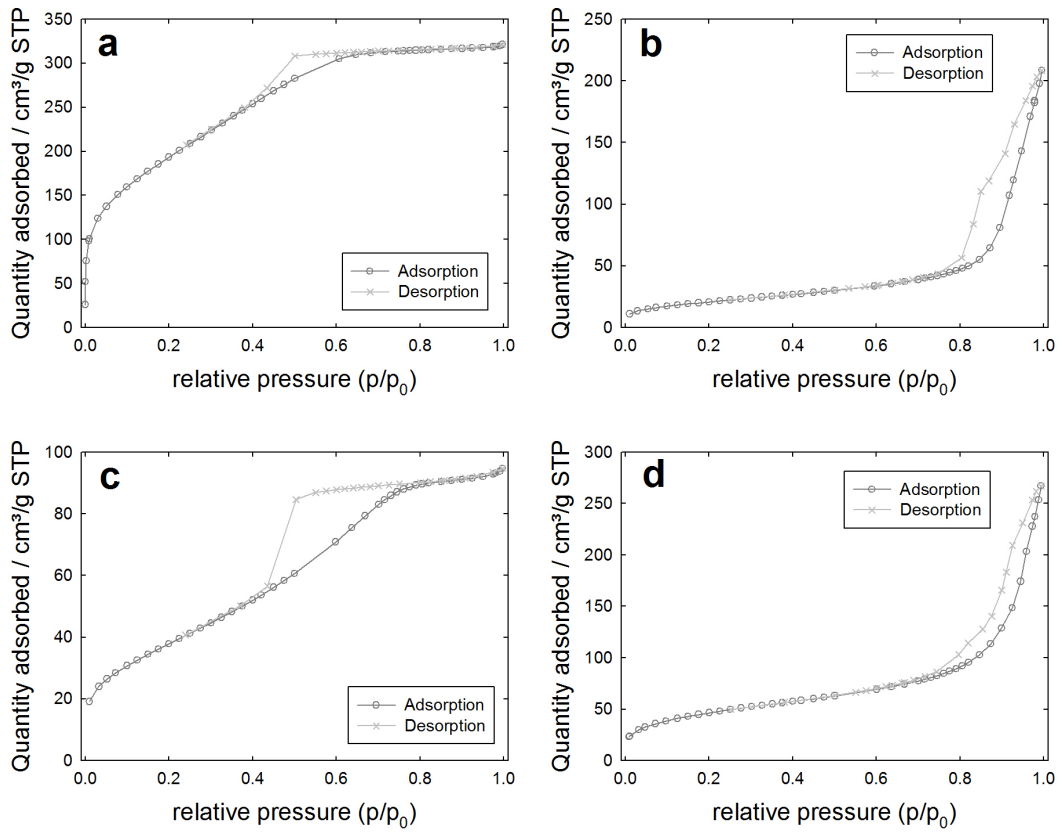
Figure 3.8: Isotherms of nitrogen sorption experiments at 77K for a) small silica, b) large silica, c) small zirconia and d) large zirconia.

Table 3.1: Particle size distribution of DLS by the mass-weighted (m.w.) and number-weighted (n.-w.) evaluation method

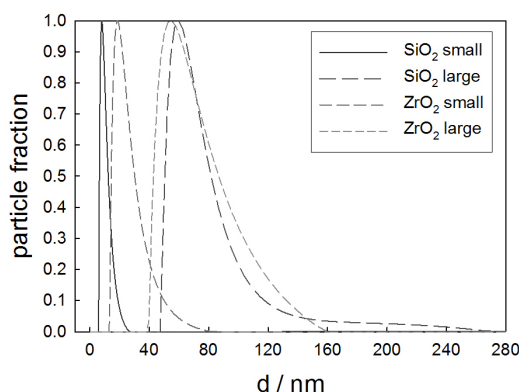| Particle	$d_{DLSn.-w.}$	Peak width n.-w.	$d_{DLSm.-w.}$	Peak width m.-w.
	nm	nm	nm	nm
SiO$_2$ small	7.8	2.3	9.4	2.7
	4.0	1.2	6.0	2.4
	11.1	1.1	13.5	1.1
SiO$_2$ large	45.0	4.5	50.0	4.0
	54.0	10.8	58.0	10.4
	52.0	5.2	58.0	5.8
	56.0	5.6	60.0	10.2
	54.0	9.2	62.0	11.8
	64.0	12.8	72.0	19.4
	80.0	8.0	80.0	8.8
ZrO$_2$ small	19.8	4.0	24.0	9.1
	17.4	5.2	24.0	9.8
	16.8	3.4	22.8	8.9
	18.0	3.6	24.0	9.4
	20.0	4.0	26.0	9.6
	19.2	3.8	26.0	12.0
	17.8	3.6	22.0	7.5
ZrO$_2$ large	38.0	7.6	37.0	16.5
	36.0	7.2	50.0	17.0
	54.0	14.6	80.0	35.2
	60.0	12.0	68.0	15.7
	46.0	9.2	64.0	23.7
	54.0	10.8	66.0	19.1

Figure 3.9: Mass-weighted particle diameter distribution from DLS for the respective nanoparticle powder dispersed in ethanol (SiO_2, diameter from SAXS evaluation: 4.3 and 53.4 nm) or water (ZrO_2, SAXS: 4.0 and 33.8 nm).

BET and XRD, only the size but not the distribution width is given, but for both methods a measurement error of at least ten percent is estimated.

Mass-weighted and number-weighted particle size distribution by SAXS

The nanoparticle diameter from SAXS has been calculated with respect to number- or volume weight. As an example, one may distinguish between the first moment of the Gaussian particle size distribution, the number-length weighted mean diameter $d_{1,0}$, and the third moment, the number-weighted diameter mean $d_{3,0}$, which was in general used for the figures in the paper. Both these values are number-weighted mean values, whereas the fourth moment divided through the third moment is denoted as the mass-weighted mean $d_{4,3}$ [84]. Table 3.3 shows the effect of the respective evaluation method, where the different weight of the distribution leads to the relation $d_{4,3} > d_{3,0} > d_{1,0}$.

Fits of SAXS patterns with a Gaussian size distribution of spheres or the Beaucage model with a lognormal distribution

The Beaucage model [81] is here formulated for an arbitrary number n of hierarchical levels

$$\bar{P}(q) \propto \sum_{i=1}^{n} \left(G_i e^{\frac{-q^2 R_{gi}^2}{3}} + B_i \left(\frac{\mathrm{erf}(qR_{gi}/\sqrt{6})^3}{q} \right)^{p_i} \right) \tag{3.6}$$

where G_i and B_i are the numerical prefactors, p_i are referred to as Porod exponents, R_{gi} are the gyration radii and $erf(x)$ is the error function. The particle radius r_{SAXS} of spherical particles is obtained by $r_{SAXS} = R_{gi}\sqrt{5/3}$. For a lognormal distribution of the size of particles with $p_i = 4$ (a sharp interface), the ratio B/G

Table 3.2: Particle diameter and distribution width (standard deviation) obtained from the different measurement techniques SAXS, DLS, TEM, BET and XRD

Particle	d_{SAXS}[nm]	d_{DLS}[nm]	d_{TEM}[nm]	d_{BET}[nm]	d_{XRD}[nm]
SiO$_2$ small	4.3± 1.2	7.8± 2.3			
	4.5± 1.5	4.0± 1.2			
	4.3± 1.7	11.1± 1.1			
SiO$_2$ large	40.5± 5.0	45.0± 4.5			
	47.4± 5.9	54.0±10.8			
	45.3± 6.4	52.0± 5.8	47.2 ±2.8		
	46.5± 7.1	56.0± 5.6			
	50.4± 9.1	54.0± 9.2	54.2 ±6.1		
	53.4± 8.8	64.0±12.8	60.8 ±7.3	36.0	
	51.0± 11.3	80.0± 8.0			
ZrO$_2$ small	3.8± 1.2	19.8± 4.0			
	3.7± 1.0	17.4± 5.2			
	3.8± 0.9	16.8± 3.4	3.9 ±0.9		
	3.9± 1.1	18.0± 3.6			
	4.0± 1.2	20.0± 4.0			
	4.3± 1.0	19.2± 3.8			
	4.7± 1.2	17.8± 3.6	6.0 ±1.4	19.0	4.5
ZrO$_2$ large	15.2± 6.7	38.0± 7.6			
	19.2± 7.6	36.0± 7.2			
	19.6± 8.3	54.0±14.6			
	18.5± 7.2	60.0±12.0			
	19.3± 5.0	46.0± 9.2			
	33.8± 11.2	54.0±10.8	38.1±12.1	16.0	2.9

Table 3.3: Particle size distribution of SAXS given by the number-length, number-weighted and mass-weighted mean

Particle	$d_{1,0SAXS}$ [nm]	$d_{3,0SAXS}$ [nm]	$d_{4,3SAXS}$ [nm]
SiO$_2$ small	3.9	4.3	4.9
	4.0	4.5	5.3
	3.6	4.3	5.3
SiO$_2$ large	39.9	40.5	41.6
	46.7	47.4	48.8
	44.4	45.3	47.1
	45.4	46.5	48.6
	48.8	50.4	53.5
	51.9	53.4	56.2
	48.5	51.0	55.6
ZrO$_2$ small	3.4	3.8	4.4
	3.4	3.7	4.2
	3.6	3.8	4.2
	3.6	3.9	4.5
	3.6	4.0	4.6
	4.0	4.3	4.7
	4.4	4.7	5.3
ZrO$_2$ large	12.6	15.2	19.5
	16.3	19.2	24.0
	16.5	19.6	25.0
	15.8	18.5	23.2
	18.0	19.3	21.6
	30.1	33.8	40.1

allows the calculation of the polydispersity index (PDI) [63]. From the PDI and the expected value (the mean) $\langle R_{gi} \rangle$, the standard deviation s.d. of the distribution is obtained by

$$\sigma = \left(\frac{\ln PDI}{12} \right)^{(1/2)} \quad \text{and} \quad s.d. = \langle R_{gi} \rangle \left(\exp\left(\sigma^2 - 1 \right) \right)^{(1/2)} \tag{3.7}$$

The form factor for spheres with a Gaussian size distribution is Eq. 3.2. In the case of a significantly small distribution, the integral can be extended from minus infinity to infinity and analytically solved:

$$\bar{P}(q, R, b) \propto \mid b \mid e^{(-2b^2q^2)} \frac{\sqrt{\pi/2}}{q^6}$$
$$(e^{(2b^2q^2)}(1 + q^6(b^2 + R^2)) + (-1 + q^2(-3b^2 - 4b^4q^2 + R^2))\cos(2qR)$$
$$- 2q(1 + 2b^2q^2)R\sin(2qR))$$
$$\tag{3.8}$$

SAXS patterns were fitted by these two models (spheres with a Gaussian size distribution and with the Beaucage model with a lognormal distribution). Both models lead only to a slight difference for the diameter and its distribution width, being shown in Table 3.4.

Table 3.4: Particle size distribution of large zirconia calculated with two sphere radii with a Gaussian size distribution and the model of Beaucage for multiple levels of hierarchy [81]. The value shown here is the large diameter (the aggregate diameter, as large zirconia nanoparticles are built up of small crystalline units). PDI is the polydispersity index, which allows the evaluation of the standard deviation of the lognormal distribution in the Beaucage model [63]

Particle	$d_{3,0 SAXS}$ [nm]	$s.d._{GAUSS}$ [nm]	$d_{BEAUCAGE}$ [nm]	$s.d._{BEAUCAGE}$ [nm]	PDI
ZrO$_2$ large	15.2	6.7	17.4	3.0	3.6
	19.2	7.6	19.8	3.7	4.6
	19.6	8.3	21.7	4.0	4.9
	18.5	7.2	26.3	6.6	13.4
	19.3	5.0	26.9	5.5	6.3
	33.8	11.2	34.1	6.5	5.3

Comparison of three different approaches for the structure factor

Three different approaches for the structure factor were compared, the simple model with an effective structure factor, the decoupling approximation and the local monodisperse approximation to include polydispersity [77, 78, 79]. For the fit, the software

SASFit [91] was used. Additionally the models were calculated with the software Mathematica [92] for comparison. No considerable differences between the respective models were observed. The results of SASFit are listed in Table 3.5 and shown in Figure 3.10.

Table 3.5: Particle diameter D and Gaussian distribution width b as well as hard-sphere volume fraction η and hard-sphere volume radius $2R_{HS}$ obtained from three different models for two selected examples.

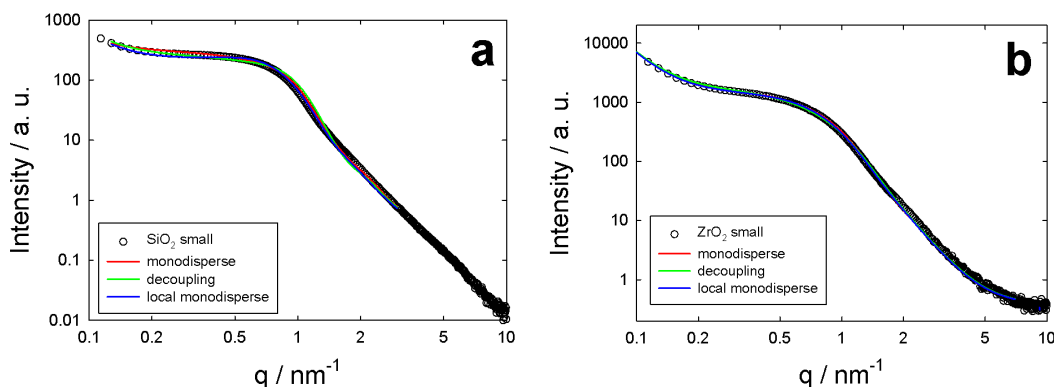| Particle	Model	D	b	η	$2R_{HS}$
		[nm]	[nm]		[nm]
ZrO$_2$ small	simple model	2.80	1.04	0.076	4.54
	decoupling	2.84	0.87	0.051	3.00
	local monodisperse	2.48	0.99	0.049	
SiO$_2$ small	simple model	4.84	0.98	0.193	5.46
	decoupling	4.40	0.58	0.138	6.20
	local monodisperse	4.58	0.79	0.157	

Figure 3.10: Fit of small (a) silica and (b) zirconia nanoparticles with different models, simple model with effective structure factor (red line, Eq. 3.1 of the paper), decoupling approximation (green line, Eq. 3.4 of the paper), local monodisperse model (blue line, Eq. 3.5 of the paper).

4 Nanoparticle assemblies as probes for self assembled monolayer characterization: The correlation between surface functionalization and agglomeration behavior

In this chapter, the ordering of dodecyl chains on the surface of zirconia nanoparticles has been investigated in different variation of mixed monolayers of phosphonic acid capping agents. Therefore, four co-capping agents, methyl-, phenyl-, pyryl- and tert-butyl phosphonic acid have been used in varying mixing ratios with dodecyl phosphonic acid. FTIR measurements study the effect of the disorder of the dodecyl chains due to an increasing amount of co-adsorbed capping agents. By disordering the dodecyl chains, the agglomeration of the particle decreases, as the interparticle bilayers, formed via long alkyl chain, are disturbed by co-adsorbed capping agents. The disturbance and hence disorder have been investigated by SAXS. Based on the correlation of the order of alkyl chains with the agglomeration behavior of the zirconia nanoparticles, the particles can be used as probes for self-assembled monolayer investigation by an indirect method (SAXS) and a routine spectroscopical method for chemical analysis of surface groups (FTIR).

This chapter is based on the publication Feichtenschlager et. al. [S2].

4.1 Introduction

The surface-modification of nanoparticles with coupling agents is mainly used to increase the compatibility between inorganic nanofillers and their environment [18]. Coupling agents consist of anchor groups to allow a stable attachment to the nanoparticle surface, a spacer to tune physical parameters and optionally a functional group to obtain further chemical interactions with the environment such as the copolymerization in the formation of nanocomposites [93]. Frequently the spacer is given

by a long alkyl chain to increase the compatibility of hydrophilic inorganic surface with non polar media such as common solvents, monomers or polymers. These long alkyl chains are able to form self-assembled monolayers (SAMs) on plane substrates [12, 16] on the crystal facets of nanoparticles or even on small facets of clusters [94, 95, 96, 97]. Ordered surface structures are expected to be responsible for the formation of alkyl chain bilayer structures between nanoparticles [98, 99, 100] leading to a formation of nanoparticle assemblies and thermodynamically very stable agglomerates [96, 101, 102]. This effect should be prevented as it is unfavorable in the development of homogenous nanocomposites.

Therefore, it has to be investigated how the thermodynamic driving force of such surface-aggregates can be reduced and how their formation affects the agglomeration of nanoparticles. To investigate the influence of self-assemled monolayer formation, one can disorder the surface bound long alkyl chains by other co-adsorbed molecules to form mixed monolayers. This was already investigated for macroscopic substrates by using mixed monolayers of different alkanethiols on gold surfaces to decrease the alkyl chain ordering [103, 104, 105, 106, 107, 108, 109]. The functionalization of metal oxide surfaces, e. g. by mixed phosphonic acid monolayers [110], is widely unknown. There is the question whether such a method is transferable to nanoscopic facets of transition metal oxide nanoparticles and how the mixed monolayer-formation affects the SAM ordering. Additionally, one can investigate a correlation between alkyl chain modified surfaces and particle agglomeration behavior. Recent works investigated mixed surface modification of nanoparticles mostly for mixed alkyl thiols on gold nanoparticles e.g. as emulsion stabilizing agent [111, 112], to control the spacing between deposited particles [113], to fine tune specific physical surface properties [114] or to dilute a surface bound functionality for biological applications [115]. For technologically highly relevant transition metal oxide nanoparticles, such as ZrO_2 (ceramics, nanocomposites), more knowledge on mixed surface modification and the underlying principles is necessary, as SAM@transition metal oxide nanoparticles play a significant role in tuning their dispersion behavior [116].

A systematic study of different organic moieties, such as aromatic systems and linear and branched alkanes, and their influence on the ordering of the particle surface SAM was carried out. Hydrothermally prepared ZrO_2 nanocrystals were used as model system in combination with organophosphonate capping agents. Dodecyl phosphonic acid was choosen as the self-assembling system because of its non-crystalline behavior at room temperature [117, 118] contrary to the usually applied octadecyl capping agents. Feichtenschlager et. al. presented in their work on the formation of SAMs at nanoparticles that crystalline octadecyl phosphonic acid systems are qualitatively similar to the non crystalline dodecyl system with respect to a possible SAM-disordering by a mixed modification with a phenyl-co-capping agent [119]. Therefore the results obtained by this study can be transfered for other long alkyl chain systems. For co-adsorbing molecules, methyl-, phenyl-, pyryl- and tert-

butyl phosphonic acid were used in different mixing ratios with dodecylphosphonic acid to vary sterical (molecular) properties of the co-capping agent. The monolayer formation and the agglomeration tendency were investigated by the spectroscopic method FTIR and the structural method small-angle X-ray scattering (SAXS).

4.2 Experimental Section

Materials. All solvents (HPLC grade) and chemicals were purchased from Sigma Aldrich. Methanol was purified using a PureSolv (Innovative Technology inc.) solvent purification system. Phenylphosphonic acid was recrystallized from acetonitrile. All other chemicals were used as received.

Instrumental Analysis. Fourier transform infrared spectroscopy (FTIR) measurements were performed on a Bruker Tensor 27 Spectrometer under ambient air (64 scans at a resolution of 1 cm^{-1}) in transmission mode using KBr (Aldrich) disks as a sample matrix.

Transmission electron microscopy (TEM) images were recorded on a JEOL JEM-100CX and on a FEI TECNAI G20 transmission electron microscope. High resolution TEM (HRTEM) images were recorded on a FEI TECNAI F20 microscope. The samples were attached to Formvar copper grids by dispersing them in ethanol using an ultrasound cleaning bath, adding one drop on the copper grid and evaporating the solvent.

Small angle X-ray-scattering (SAXS) measurements were performed under vacuum in transmission geometry using a rotating anode X-ray generator equipped with a pinhole camera (Nanostar, Bruker-AXS). Cu K$_\alpha$ radiation was monochromatized and collimated from crossed Goebel mirrors and detected with a 2D position sensitive detector (Vantec 2000). Measurements were carried out at two different distances (13 cm and 108 cm) to cover a wide q range. All SAXS patterns were radially averaged and corrected from background scattering to obtain the scattering intensities in dependence on the scattering vector q $= 4\pi/\lambda \sin\theta$, where 2θ is the scattering angle and $\lambda =$ 0.1542 nm the X-ray wavelength.

A detailed description of the synthesis of dodecylphosphonic acid and 1-pyryl phosphonic acid is found in the publication Feichtenschlager et. al. [S2] as well as the thesis of Bernhard Feichtenschlager [120].

Preparation of zirconia nanocrystals. The preparation and characterization of ZrO$_2$ nanocrystals with a 22 nm spherical equivalent diameter, from mass weighted distribution, (18 nm number weighted) according to a literature known procedure [69] is described in the publication Sajjad et. al. [S3].

Zirconia nanoparticle surface modification reactions were performed as described in Feichtenschlager et.al. [119], analogous to the well known process for titania surface functionalization [15]. First 5 mL of 10 g/L aqueous nanoparticle dispersion was prepared by dispersing the zirconia nanoparticle powder for 30 min in an ultrasonic bath. Afterwards HCl conc. was added dropwise to the dispersion to adjust

the pH to 2. The phosphonic acid, e.g. 18.7 mg dodecylphosphonic acid for a 7.5 mM total capping agent concentration, was dissolved in 5 mL methanol, added to the particle dispersion and stirred for 2 days. The particles were then isolated via centrifugation at 6000 rpm, washed three times with ethanol (centrifugation at 6000 rpm) and dried over P_2O_5 at 5 mbar for 24h.

More details about the characterization of the synthesized and modified zirconia nanoparticles with nuclear magnetic resonance (NMR) and thermogravimetric analysis (TGA) are summerized in the thesis of Bernhard Feichtenschlager [120].

4.3 Theory

The agglomeration behavior of the mixed monolayer endcapped nanoparticle powders was studied via small angle X-ray scattering (SAXS) using the following model to describe the agglomerated particle system:

A unified equation for the scattering intensity $I(q)$ has been proposed by Beaucage [80, 81, 82] to describe two functions, one based on Guinier's law and the other on the structurally limited power law 4.1

$$I(q) = \left(Ge^{\frac{-q^2 R_g^2}{3}} + B \left(\frac{\text{erf}(qR_g/\sqrt{6})^3}{q} \right)^p \right) S(q) \tag{4.1}$$

Here G and B are numerical prefactors, p is referred to as $Porod$ exponent, R_g is the gyration radius and $erf(x)$ the error function. The size of spherical particles r_{SAXS} is related to the radius of gyration by $r_{SAXS} = R_g\sqrt{5/3}$. For weakly agglomerated systems, the structure function $S(q)$ [43, 77]

$$S(q) = \frac{1}{1 + 24\eta G(2R_{HS}q)/(2R_{HS}q)} \tag{4.2}$$

describes the interference of the scattering of particles, containing the function $G(2R_{HS}q)$ being defined by Kinning and Thomas [43]. Two additional parameters are used, the hard-sphere radius R_{HS}, which gives the correlation distance of particles within a cluster, and a mean hard-sphere volume fraction η, which gives the probability to find neighboring particles. The expression for $S(q)$ was derived from the Percus-Yevick approximation [42]. Fitting was performed by the software Mathematica^{TM}. The hard sphere volume fraction η is a numerical value describing the degree of agglomeration of the modified zirconia nanoparticles - the higher η, the stronger the tendency to agglomerate. The Beaucage model applied in this work combines the form factor of spherical particles with a wide size distribution and a structure factor describing the effect of the capping molecules on the degree of agglomeration of the nanoparticles.

4.4 Results

Hydrothermally grown ZrO_2-nanocrystals have been used as model systems for SAM-formation on nanoscopic crystal facets. Characterization by TEM and HRTEM (Figure 4.1) reveals the single-crystal-nature of the particles. Equivalent spherical particle diameters of 6 nm are obtained by TEM and SAXS.
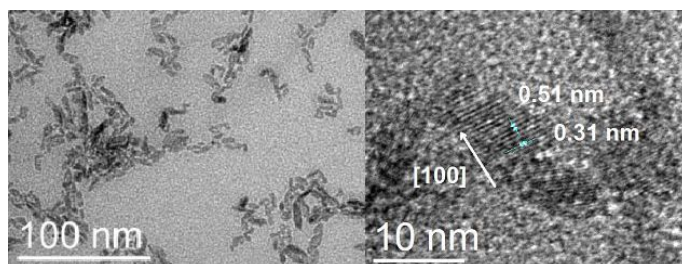

Figure 4.1: Representative TEM-image of ZrO_2 nanocrystals (baddeleyite) and HRTEM-detail showing the single-crystalline nature of exemplary two nanoparticles.

Self-assembled monolayer formation on the nanoparticle surface

The disorder in dodecyl phosphonic acid SAMs correlating with an increasing mixing ratio of co-capping agents can be observed by a typical shift of the methylene C-H-vibration of the C12-chain-segments to higher wavenumbers in IR-spectroscopy. The organophosphonates used in this chapter are summerized in Table 4.1. The influence of the sterical demand of the co-adsorbing molecules was investigated applying methyl and tert-butyl phosphonic acid as co-adsorbing capping agents. Aromatic capping molecules were used to study the effect of potential p-p stacking phenomena (pyryl- and phenylphosphonic acid) on the C12 chain ordering.
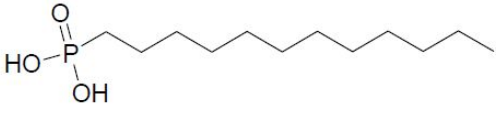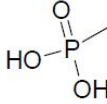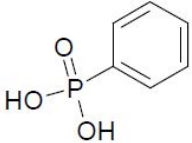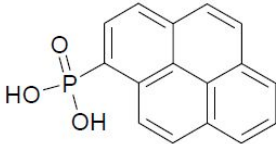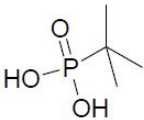
The functionalization reaction of the ZrO_2 nanoparticles with a mixture of DPPA and further capping agent to form a mixed monolayer on the nanoparticle surface was carried out by mixing the capping agents in a certain molar ratio (10 mol%, 30 mol%, 50 mol%, 70 mol% and 90 mol% DPPA) to obtain a total concentration of 7.5 mM which is the threshold concentration for a monolayer coverage within this specific system [119].

FTIR investigation on the mixed self-assembled monolayer structure

The degree of ordering of the surface DPPA molecules has been investigated applying FTIR spectroscopy. Self-assembled monolayer formation was detected via the shift of the long alkyl chain methylene group C-H-vibrations to lower wavenumbers with decreasing number of gauche defects in the alkyl chain. This indicates a higher ordering and thus a more dense chain packing in the SAM [121, 122] with the asymmetrical CH-stretching mode being the most sensitive and significant [123]. Four

Table 4.1: List of the studied surface modifying agents.

capping agent formula	capping agent name	abbreviation
	dodecyl phosphonic acid	DPPA
	methyl phosphonic acid	MPPA
	phenyl phosphonic acid	PhPPA
	1-pyryl phosphonic acid	PyPPA
	tert-butyl phosphonic acid	tBuPPA

sample series were obtained with DPPA and MPPA, PhPPA, PyPPA, or tBuPPA as co-capping agent in different ratios. FTIR-spectra of the C-H-stretching region are presented in Figure 4.2. The asymmetric methylene chain C-H stretching resonance is visible around 2920 cm^{-1} and the symmetric stretching resonance around 2850 cm^{-1}, the other two resonance peaks are assigned to methyl-CH-resonances. The resonance frequencies of the asymmetric methylene C-H-stretching vibration for the dodecyl-chain in the SAM for every molar percentage of a certain disturbing capping agent are listed in Table 4.2.

Table 4.2: Methylene C-H-vibration ν_{as} of the dodecyl chain for different percentage of co-capping agent at the zirconia nanoparticle surface.

Mol% DPPA	rest MPPA ν_{as} cm^{-1}	rest PhPPA ν_{as} cm^{-1}	rest PyPPA ν_{as} cm^{-1}	rest tBuPPA ν_{as} cm^{-1}
100	2921.9	2921.9	2921.9	2921.9
90	2922.6	2922.0	2922.7	2922.6
70	2923.4	2922.0	2923.1	2922.6
50	2923.1	2922.6	2923.7	2923.7
30	2923.0	2923.6	2923.8	2924.6
10	2924.4	2924.9	2924.1	2926.3

SAXS-Investigations on the agglomeration behavior of mixed modified nanoparticles

The scattering curves of the four different mixed surface layer on the nanocrystal facets are shown in Figures 4.3a to 4.3d, one diagram for each disturbing co-capping molecule. The shoulder around q = 1 nm^{-1}, representing the nanoparticle dimension, clearly shows the trend to be more pronounced with an increased packing of particles per volume fraction. The peak at q = 12.3 nm^{-1} originates from the diffraction at the ZrO$_2$ (100) crystal planes. XRD could not be used to determine the degree of order, as one would expect a short range order signal from the alkyl chains in the range from about q =11 to 13 nm^{-1} [16, 124], which is unfortunately masked by the much stronger crystalline zirconia peak. The hard sphere volume fraction η as a numerical parameter calculated from the scattering curves for the degree of agglomeration and fitted by the Beaucage Model (Eq. 4.1) is listed in Table 4.3 for all series. The fit parameters, the radius of gyration R_g, the equivalent spherical radius R_s, the hard-sphere radius R_{HS} and the Porod exponent p as well as the hard-sphere volume fraction η compared with the actual volume fraction η_s are listed in Table 4.4.
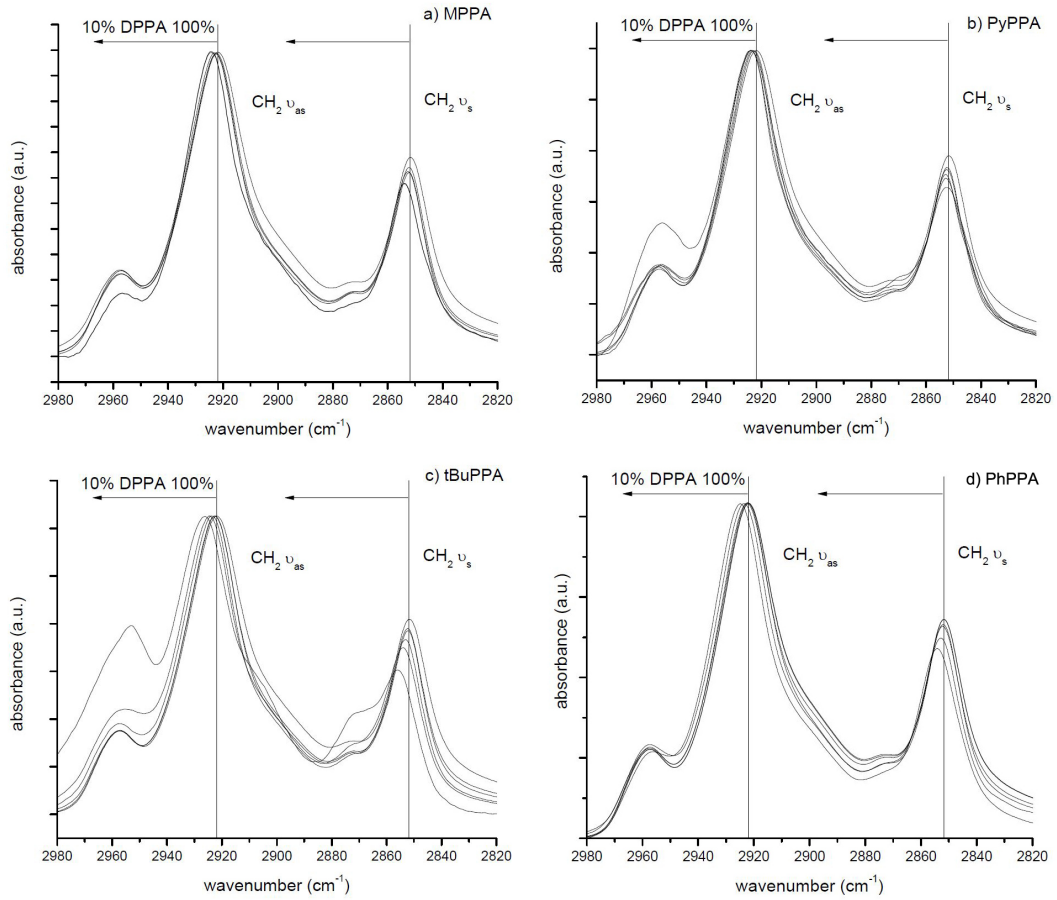
Figure 4.2: Infrared spectra of DPPA mixed with a) MPPA, b)PyPPA, c) tBuPPA
and d) PhPPA @ZrO$_2$: Methylene C-H shifts to higher wavenumber
at increasing co-capping agent surface concentration. This is indicated
by the arrows, going from right (highest DPPA-content) to left (lowest
DPPA content) [S2].

Table 4.3: Hard sphere volume fraction η of zirconia nanoparticle powders with dif-
ferent percentage of co-capping agent at the surface.

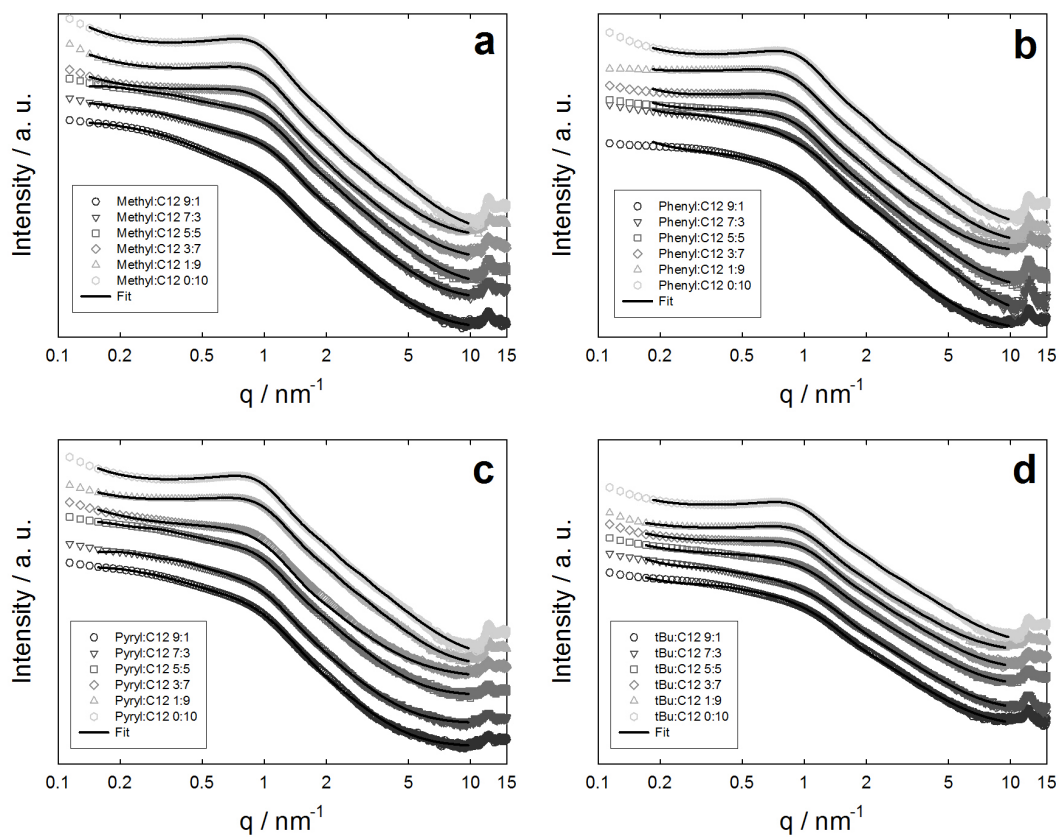| Mol% DPPA	rest MPPA	rest PhPPA	rest PyPPA	rest tBuPPA
	η	η	η	η
100	0.128	0.128	0.128	0.128
90	0.116	0.105	0.112	0.117
70	0.096	0.107	0.082	0.103
50	0.097	0.079	0.104	0.050
30	0.078	0.055	0.100	0.049
10	0.036	0.035	0.050	0.040
0	0.025	0.025	0.025	0.026

Figure 4.3: Scattering intensities from SAXS measurements for a) MPPA, b) Ph-PPA, c) PyPPA and d) tBuPPA @ZrO$_2$.

Table 4.4: List of the fit parameters obtained by the Beaucage model and the equivalent spherical radius R_s as well as the actual volume fraction η_s

	p	R_g [nm]	R_s [nm]	R_{HS} [nm]	η	η_s
DPPA/PhPPA 9:1	4.1	2.50	3.23	3.31	0.105	0.098
DPPA/PhPPA 7:3	4.0	2.50	3.23	3.31	0.107	0.100
DPPA/PhPPA 5:5	4.0	2.51	3.24	3.20	0.079	0.082
DPPA/PhPPA 3:7	4.1	2.43	3.14	3.15	0.055	0.055
DPPA/PhPPA 1:9	4.1	2.53	3.29	3.10	0.035	0.042
DPPA/PhPPA 0:10	4.1	2.56	3.30	2.98	0.025	0.034
DPPA/MPPA 9:1	4.1	2.28	2.94	3.01	0.116	0.109
DPPA/MPPA 7:3	4.1	2.22	2.87	3.00	0.096	0.084
DPPA/MPPA 5:5	4.0	2.21	2.85	2.86	0.097	0.096
DPPA/MPPA 3:7	4.0	2.24	2.89	2.82	0.078	0.084
DPPA/MPPA 1:9	4.0	2.39	3.09	2.74	0.036	0.052
DPPA/MPPA 0:10	4.0	2.48	3.20	2.95	0.025	0.032
DPPA/PyPPA 9:1	4.1	2.30	2.97	2.98	0.112	0.111
DPPA/PyPPA 7:3	4.0	2.37	3.06	2.92	0.082	0.095
DPPA/PyPPA 5:5	4.1	2.43	3.14	3.05	0.104	0.113
DPPA/PyPPA 3:7	4.0	2.36	3.05	3.01	0.100	0.103
DPPA/PyPPA 1:9	4.1	2.46	3.18	3.34	0.050	0.043
DPPA/PyPPA 0:10	4.1	2.46	3.18	2.41	0.025	0.020
DPPA/tBuPPA 9:1	4.1	2.27	2.93	2.97	0.117	0.112
DPPA/tBuPPA 7:3	4.1	2.28	2.94	2.87	0.103	0.111
DPPA/tBuPPA 5:5	4.1	2.23	2.88	3.00	0.050	0.044
DPPA/tBuPPA 3:7	4.1	2.26	2.92	3.15	0.049	0.040
DPPA/tBuPPA 1:9	4.1	2.34	3.02	3.05	0.040	0.039
DPPA/tBuPPA 0:10	4.0	2.31	2.98	3.00	0.026	0.026
DPPA	4.1	2.33	3.01	3.05	0.128	0.123

4.5 Discussion

Investigation on mixed self-assembled monolayer structure

FTIR investigations (Figure 4.4) showed that for each type of disturbing molecule (MPPA, PhPPA, PyPPA, tBuPPA), the ordering of dodecyl chains decreases with increasing percentage of these co-capping agents. This is concluded from the shift of its methylene vibrational resonance to higher wavenumbers [119]. Though each of the various molecules lead to a decrease of the alkyl-chain-ordering with increasing molar percentage, the degree varies from molecule to molecule. All four curves consist of an approximately linear area in the middle mixing ratio, which means a content of co-capping agent of 30-70%. At lower and higher percentages, the behavior is different so that the whole array of curves appears sigmoidal-shaped. One can observe that the molecules tBuPPA and PyPPA lead to a relatively high disordering already at low co-molecule percentages, whereas molecules like tBuPPA and PhPPA show (compared to a linear trend) a relatively increase in disordering in the higher co-molecule percentage region.
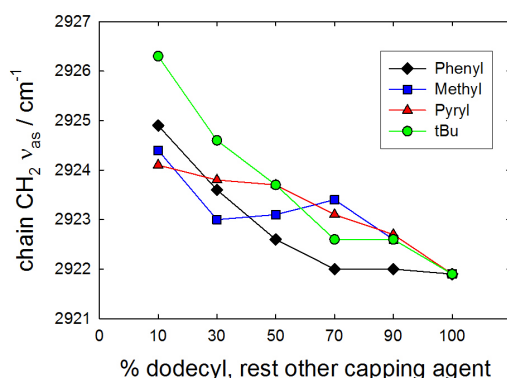

Figure 4.4: Methylene C-H-vibration ν_{as} of DPPA@ZrO$_2$ representing the alkyl chain ordering degree at different percentages of DPPA in the mixed monolayer at the nanoparticle surface, the rest to 100% coverage is the capping agent mentioned in the diagram. Lines are drawn to guide the eye.

A first conclusion from the maximum of the frequency shift from the FTIR-experiments (Figure 4.4) is that bulky molecules like tBuPPA have a stronger effect on disturbing the alkyl-monolayer-ordering in comparison to smaller molecules such as MPPA. However, the shape of the curve in Figure 4.4 can only be explained by identifying the structure of each mixed monolayer. Thereby two structure types are assumed to be present within these mixed monolayers, already reported in the literature for non-fully covered long alkyl chain monolayers [14, 125, 126]. The first type

describes the randomly mixing of different molecules to form collective monolayers. This is analogous to incomplete coverage of substrates, which was already observed for C18 phosphonates [123] and organosilane capping agents [14]. The second type describes the formation of the molecules to island structures. This was observed e.g. for octadecylphosphonic acids on mica [126] and has been intensely investigated for mixed monolayers of thiols on gold surfaces [109]. A formation of preordered structures in solutions, which adsorb to the nanoparticle surface, also might be responsible for the separation and can be observed for organosilanes but also for organophosphonates [123, 127]. However, a gradual mixture of these extreme cases is more probable for the systems investigated in this work. Furthermore, a general lower tendency to strong island formation is expected within the investigated systems, because the C12-chains used in this chapter do not show the same pronounced high ordering tendency as C18-chains [128]. Island growth seems to be preferred, if the interactions between molecules are more favored compared to interactions between two different molecules: Examples for such higher interaction forces can be the sum of van-der-Waals interactions over a long chain, p-p-interactions of extended aromatic systems, strong polar or ionic interaction or hydrogen bonds [12, 16].

Taking these structural models into account, the difference in the ordering behavior depending on the mixing ratio can be explained as followed: Small and weak interacting molecules such as MPPA show a linear like disordering behavior with increasing molar percentage because of the presence of a randomly mixed SAM for all mixing ratios. Additionally, Offord and Griffin have suggested for mixed organosilane-surface layers, that the longer alkyl chains can form ordered structures around these small molecules, where the chain packing is not dramatically effected at lower disturbing molecule surface concentration [129]. Another example of a system behaving like that is the mixture of short and long alkylthiol molecules on gold [103, 104, 106, 108]. The described behavior would not be the case for the sterically far more demanding molecule, tBu-PPA. Thus, it can be observed, that this molecule leads to a sharp increase in disordering at higher molar ratios. The larger but plane molecule PyPPA does not show a very strong increase of disordering of alkyl chains with increasing mixing ratio PyPPA/DPPA. However, the slope of the PyPPA trend curve at lower concentrations is the highest compared to all other molecules. A probable explanation is the existence of randomly mixed monolayers at low concentrations. The bulky molecules can effectively disturb the C12-SAM-formation changing to an island like regime for higher concentrations of PyPPA while the C12-chains can be still moderately ordered in DPPA@ZrO$_2$ island regions. A similar result was observed and discussed by Whitesides et al. for mixed monolayers of alkylthiols with different chain length on gold. They showed that the ordering disturbing is most effective for randomly mixed systems [109]. Similarly, Prado and Neves showed for mixed C8 and C18 chain phosphonates that a complete molecular homogeneous layer is formed, and the chains above a length of 8 carbon-atoms are expected to be disordered [110]. In an other example, Ver-

celli et al. have proven a close packed island structure via cyclic voltammetry for a system where hexylferrocenyl phosphonic acid and dodecyl phosphonic acid where adsorbed to ITO [130]. The latter is very likely to happen also in the investigated DPPA/PyPPA mixed layers at higher PyPPA concentrations because strong p-p-interactions are energetically beneficial between neighboring PyPPA molecules. Finally, the PhPPA-molecule represents a mixture of all these effects.

Until now, mostly the effect of mixing alkyl chain capping agents of different chain length on the long alkyl chain ordering has been investigated [103, 104, 105, 106, 107, 108, 109]. It has been demonstrated that a variety of non alkyl-chain moieties can also be applied for this disordering approach, even on the facets of small nanoparticles, where in most of our investigated cases random mixture is expected because of the high effectiveness of disturbing the ordering by the co-capping agent.

Agglomeration behavior of mixed monolayer modified nanoparticles

The hard sphere volume factor obtained from SAXS describes the agglomeration behavior of the nanocrystals. It decreases by nearly one order of magnitude with increasing concentration of co-capping agent, regardless of which capping agent was used (Figure 4.5). The trend appears to be in general linear for the various molecules, but differs for the respective mixed SAM system. The behavior at very low and very high mixing ratios is rather similar for each co-molecule, but considerable deviations are observed at a 1:1-mixing ratio. At 50% co-capping agent addition, tBuPPA shows the highest tendency to avoid agglomeration, followed by PhPPA. PyPPA and MPPA (Figure 4.5).
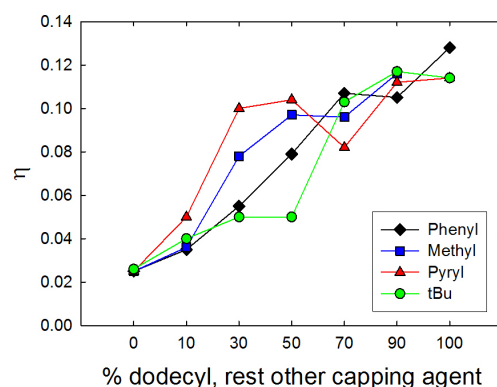

Figure 4.5: Hard sphere volume fraction η representing the agglomeration of the mixed modified zirconia nanoparticles using different capping agents for mixed monolayer formation, applied in various mixing ratios. The residual percentage to 100% coverage is the capping agent mentioned in the diagram legend. Lines are drawn to guide the eye.

The TEM-images of nanopowders capped with 100% DPPA@ZrO$_2$ powder (Figure 4.6) give an impression of the degree of agglomeration for a η-value of 0.13. The crystals are closely packed and a spacing of approximate 1-2 nm between the particles is visible, which may origin from the interparticle bilayers (Figure 4.7). Mixed modified particles are less agglomerated in the macroscopic powder assembly and thus considered to be easier dispersed using common approaches like soft ultrasound. This redispersibility enhancement is from high technological relevance and has been shown in the work of Feichtenschlager et.al. [119]. The surface-properties, such as wettability with different solvents and hydrophobicity, also change with co-adsorbing other molecules. Therefore an optimum composition has to be found for the dispersion of particles in a specific environment.
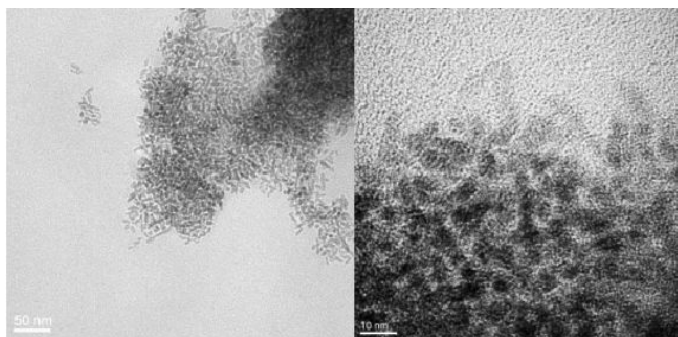
Figure 4.6: TEM-Images of agglomerates of 100% DPPA@ZrO$_2$ nanocrystals, right: detail.
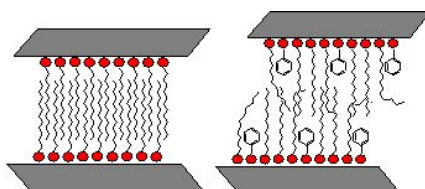
Figure 4.7: Schematic drawing of two particle facets in particle agglomerates of 100% DPPA@ZrO$_2$ (left) and mixed modified particles (right).

The fact that nanoparticles with higher content of long alkyl chains at the surface are more strongly agglomerated can be explained by the so called "zipper-effect" of the surface bound long alkyl chains. Until now, this "zipper-effect" has been investigated in literature mostly for thiols@gold-nanoparticles [94, 100, 131] and is hardly known for oxidic nanopowders. One example was published by Sahoo et al. [116] who attached hexadecyl phosphonic acid to magnetite nanoparticles. For inorganic nanoparticle systems, a mixed modification approach is mostly used to tune surface properties like polarity [111]. As shown in the scheme of Figure 4.7, a

bilayer-structure is formed between two particles. The system is nearly close packed and thus the agglomerates are difficult to break. This is a well-known phenomenon for C18 capping agents but it also occurs for C12 chains [118]. The alkyl chain packing significantly effects the dispersibility of these particle powders and dispersion stability [119]. The hypothesis that a decreasing alkyl-chain-"zipper-effect" is responsible for a decrease in agglomeration with the formation of a mixed monolayer is also supported by the observation from SAXS. The particles modified with 100% co-capping agent all show nearly the same agglomeration behavior. Regardless of the sterical demand of the used capping agent (MPPA or PyPPA), the η values are nearly identical at this point. Therefore it can be excluded that the observed change of the hard sphere volume fraction in the mixed samples just results from different distances of the particles in the agglomerates. It seems that a general property is changed, which determines the strength of the interaction between two crystal facets of two different particles "zipped" together. This effect has been investigated in detail for (non mixed) alkanethiols of different chain length on Au-clusters by Terrill et al [100]. They show a correlation between the degree of chain packing and particle agglomeration behavior using DSC, SAXS and AFM-data concluding that a zipper-effect can also be strong for smaller particles because of their tendency for surface energy minimization. This effect is also described for gold-nanoparticles with a surface area of approx. 100 m^2/g by Lennox et al. [94, 131] where they describe an agglomeration structure with higly ordered interparticle alkyl-chains compared to the dangling chains which are not participating to the "zipper" mechanism. For larger facets this effect is considered also to be strong as over larger facets, the number of interacting alkyl chains is higher. A further question is, why the trend of a decreasing "zipper-effect" is different for the different used molecules. The difference in the hard sphere volume fraction between the different series is the highest at a 50% mixing ratio. In addition, a tendency to a linear trend for disordering with molar percentage of co-capping agent would be expected for a total randomly mixed surface layer, but deviations can be observed. This fact can as well be explained by accounting for two mixing regimes (island like and randomly mixed), where molecules like PyPPA have a higher tendency to an island-like-SAM and molecules like tBuPPA tend to a randomly mixed layer.

Correlation of surface-SAM-ordering and particle agglomeration behavior

The main aim is to correlate the molecular parameter, namely the gauche-defects observed by IR, and the macroscopic parameter, namely particles per volume unit as investigated by SAXS. This correlation is plotted in Figure 4.8. All series follow a general trend: With decreasing wavenumber, which means less gauche defects within the alkyl chains due to higher ordering in the surface-SAM, the agglomeration of the particles increases. This indicates that these phenomena are linked together underlining the "zipper-effect"-theory of an interparticle bilayer formation. However, some data points do not show a strong correlation. In the case of the PyPPA series

correlation even a stronger agglomeration is observed at higher alkyl-disordering. Reproduction of these outlying points confirmed their significance. This may origin from strong interaction of pyrene molecules within the bilayer in these regions of the diagram as pyrene moieties from one particle could interact strongly with others on the neighbor-particle, which is very likely to occur due to the high tendency for strong p-p-interaction in such systems. Also the tBuPPA series does not fit into the scheme at the point of very high disordering (2926.3 cm^{-1}). The agglomeration there is nearly identical to other molecules with this mixing ratio. This would mean that at a certain point of disordering or alkyl chain dilution, the agglomeration behavior does not change, no zipper effect is present and thus further disordering of the alkyl chains does not further reduce the particle packing.
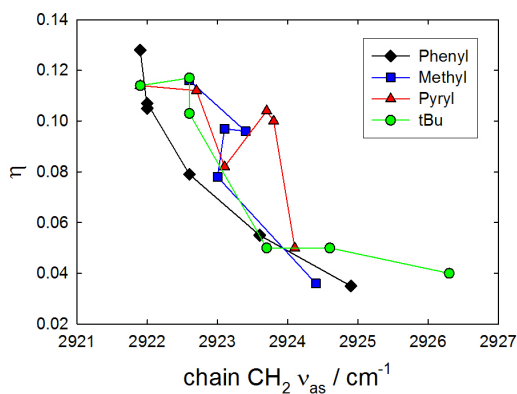
Figure 4.8: Correlation of hard sphere volume fraction η from SAXS and attached DPPA-methylene chain asymmetric vibration from FTIR of mixed modified ZrO$_2$ nanoparticle powders. Lines are drawn to guide the eye.

From the correlation of FTIR and SAXS one can conclude that the structural phenomenon of agglomeration of alkyl chain modified nanoparticles is strongly related to the nanoscopic phenomenon of surface ordering, which can be controlled on a molecular level.

The SAM, consisting of 100% dodecyl-chains, showed moderate ordering with no full crystallinity of the layer as it would be the case for C18 [119] but far more ordered than in a liquid state. This is expected and desired in terms of dispersion behavior of the nanoparticles. With increasing amount of adsorbed co-capping agent, the ordering of the dodecylchains decreased significantly. This effect was quantitatively different for different co-adsorbed molecules (Figure 4.9). From this study, one could deduce that with increasing degree of co-capping agent within one series the particle agglomeration decreased over nearly one order of magnitude, and thus the redispersibility properties of the nanoparticle powders are improved (Figure 4.9).
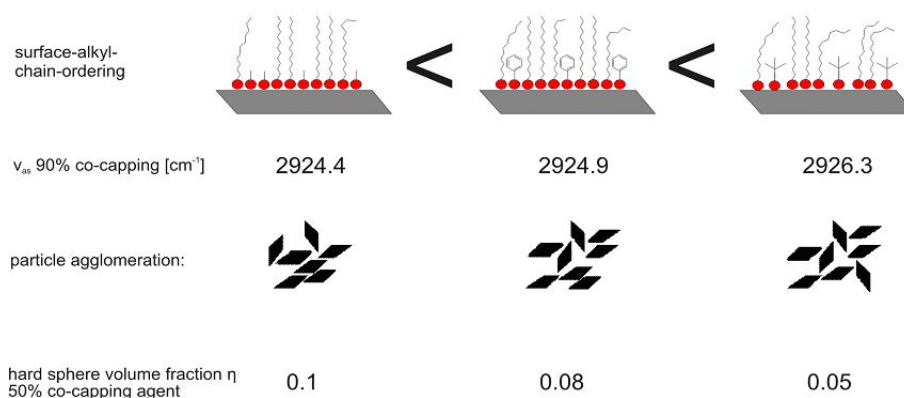
Figure 4.9: Scheme of the surface SAM-disordering and mixed modified particle agglomeration behavior depending on the nature of the organic moiety of the used co-capping agent.

4.6 Conclusion

The ordering of dodecyl chains in mixed monolayers of phosphonic acid capping agents on zirconia nanocrystal(facet)s, prepared by a co-adsorbing approach, has been investigated by SAXS and FTIR. Different phosphonic acid co-capping molecules to disturb the long alkyl chain ordering have been studied, namely the small methyl-, the bulky and planar pyryl-, the sterical demanding tert-butyl-, and the intermediate phenyl-moiety.

In FTIR-studies, the C-H vibrational resonances of the dodecyl-chain-methylene-units were used to detect the degree of alkyl chain packing in the self-assembled monolayer (SAM) via a blueshift with increasing gauche defects. Some moieties as the small methyl-group showed less tendency to disorder the C12 chains and bulky moieties like tert-butyl resulted in the highest chain disordering. The fact that the alkyl chain disordering does change with the mixing ratio with the same trend for all different co-capping molecules, can be explained by the presence of different regimes of ordering and disordering: Namely SAM structure types between the two extrema of a homogeneously mixed monolayer and a island like layer, where the two molecules are phase separated. Phase separation within the SAM is considered to be very strong for molecules such as pyrene phosphonic acid, having the tendency to homo-interact given by the natural p-electron rich molecular structure. For this reason, this bulky molecule has less influence on the ordering degree of the alkyl chain e.g. as compared to the smaller phenyl-capping agent.

The agglomeration behavior of the prepared, mixed modified, nanoparticle powder series has been studied with small angle X-ray scattering (SAXS), calculating a hard sphere volume fraction number from the scattering curves as a value for the density of nanoparticle packing. For all different co-capping agent molecule series, a good

correlation between the agglomeration behavior of the nanoparticles and the degree of ordering of the surface bound long alkyl chains could be found. This observation allows the conclusion that for the investigated system a stronger alkyl chain ordering causes higher agglomeration of the particles. This can be explained by a "zipper-effect" where the nanoparticles agglomerate via alkyl-bilayers between their crystal facets (Figure 4.7). Pyrene-moieties on the surface show a weaker correlation of alkyl chain ordering and particle agglomeration, which can be due to a competing pyrene-pyrene-interparticle-bilayer-formation at the pyrene island regions, leading to more agglomeration.

These results point out that the well known chemistry of mixed monolayer formation on macroscopic substrates can be expanded to nanoscopic (metal oxide) crystal facets resulting in tunable physical surface properties. Until now there has been a lack of systematic studies on the "zipper-effect" connected to surface functionalization of technologically highly relevant metal oxide nanoparticles (nanocomposites, ceramics). With this study it has been shown how surface tuning on molecular level impacts nanoscopic surface ordering properties and thus the macroscopical phenomenon of particle agglomeration behavior. The next step would be to apply this knowledge to inorganic-organic-nanocomposite technology with the additional parameter of a polymer matrix.

Additionally, accounting for the correlation between SAM-ordering and particle agglomeration, the characterization of SAMs at nanoparticles by two fundamentally different methods could be carried out: Nanoparticles can be used as probes for SAM-investigations by applying an indirect method (SAXS), which allows to draw agreement on the SAM-structure from the agglomeration behavior of the nanoparticles. The scattering results are in coincidence with the direct method of FTIR-spectroscopy, which directly probes the molecular surface structure. It is surprising that a structural approach (SAXS) shows a comparable sensitivity as a spectroscopic approach (FTIR).

5 Influence of varying surface-functionalizations on the homogeneity in nanocomposites

In this chapter, the influence of the chemical parameters of the inorganic-organic building block surface-functionalization on the macroscopic properties of the materials was investigated to give novel insights into the importance of surface-functionalization. Two types of nanoparticles, SiO_2 and ZrO_2, were synthesized in two different particle sizes, one in the lower nanometer length scale (5-15 nm in diameter) and one in the upper nanometer length scale (30-60 nm in diameter). The compounds prepared and surface-functionalized were incorporated in three different polymer matrices: polystyrene (PS), presented in chapter 5.1, poly(methyl methacrylate) (PMMA) in the chapters 5.1 and 5.2 and epoxide resin in the chapters 5.3 and 5.4. Structural characterization of the resulting nanocomposites is performed by small angle X-ray scattering (SAXS): From the SAXS intensity, information on the size of nanoparticles and their agglomeration behavior is obtained. The chapters 5.1 to 5.3 focus on the agglomeration behavior of nanoparticles with different surface-functionalization and different size embedded in the three different polymer matrices. To study the influence of the modified nanoparticles on the nanocomposite properties, mechanical experiment such as hardness tests are presented for the ZrO_2/PMMA system (chapter 5.2) and further mechanical as well as thermomechanical experiments (differential scanning calorimetry) are described in detail in chapter 5.4.

5.1 Control of agglomeration behavior by surface-functionalization of silica nanoparticles in polystyrene and poly(methyl methacrylate) nanocomposites

The chemical parameters of inorganic-organic building block surface-functionalization affect homogeneity of polymer nanocomposites and their macroscopic properties like mechanical characteristics. Therefore, a detailed study of their influence gives novel insights into the importance of surface-functionalization. SiO_2 nanoparticles are synthesized in two different sizes, one in the lower nanometer length scale (5-10

nm in diameter) and one in the upper nanometer length scale (50-60 nm in diameter). The compounds prepared and surface-functionalized are incorporated in two different polymer matrices: polystyrene (PS) and poly(methyl methacrylate) (PMMA). Structural characterization of the resulting nanocomposites is performed by small angle X-ray scattering (SAXS) and transmission electron microscopy (TEM). From the SAXS intensity, information on the size of nanoparticles and their distribution is obtained. This allows to characterize the influence of varying surface-functionalizations on the structural arrangement of nanoparticles in different polymer matrices. An adapted interface tailoring with respect to polymer type and nanoparticle type utilizing specific coupling agents leads to an enhanced homogeneous distribution, which is discussed in detail in this chapter.

5.1.1 Introduction

Polymer nanocomposites and their improved mechanical and structural properties due to the incorporated inorganic nanoparticles are of great interest for many applications. Therefore, it is crucial to understand the impact of nanofillers on the composite properties for the successful development of novel materials and their application. The answer of how the chemistry and morphology of the polymer matrix reacts with the size, shape and surface chemistry of the nanoparticles to define mechanical and structural properties is followed by a large number of researchers in the past few years [2, 132, 133].

Surface-functionalization enables to influence the interaction between the inorganic and organic components and is therefore a helpful tool to obtain homogeneous distribution of the nanofiller and adhesion, e.g. via a covalent linkage between filler and polymer [134]. The type of polymer and the incorporated nanofiller can vary over a wide range, such as zirconium oxo clusters in styrene, [135] well-defined polymer-grafted-nanoparticles mixed with free chains of polystyrene (PS), [136] various nanoscale inorganic particles in poly(methyl methacrylate) (PMMA), [137] spherical magnetic nanoparticles of maghemite in PS [138] or ligand-functionalized gold nanoparticles in thermally responsive bulk polymer films [139]. Many studies about nanocomposites with silica as nanofillers were done as silica nanoparticles are a well known system. Jouault et. al. studied the polymer chain conformation in model silica/PS nanocomposites for a better overview of adsorption or chain mobility modifications effects [140]. The influence of silica nanoparticles reinforced in PDMS-based nanocomposites on the nanocomposite strength was determined by tensile tests, which proves the effect on the mechanical properties [141]. In both previous studies, small-angle X-ray scattering (SAXS) and transmission electron microscopy (TEM) were used to determine the nanocomposite structure. SAXS can be chosen as complementary method to TEM as it enables the measurement of a probe volume in the mm^3-range, which is representative for the bulk material, whereas TEM images in the nm^3-range only a small area.

In this work, a systematic study of the various effects of the surface-functionalization on the structural materials properties of PS and PMMA was done by SAXS and TEM. The authors concentrate on two crucial parameters, first the influence of an additional polymerizable group at the coupling agent, allowing the crosslinking with the polymer matrix, and second the size of the nanoparticle and its effect on the dispersion. Furthermore, the influence of the amount of the incorporated nanoparticles on the dispersion within the polymer matrix was investigated.

5.1.2 Experimental

Materials. Trialkoxysilane coupling agents were purchased from ABCR, except 10-(trimethoxysilyl)decyl methacrylate, which has been self prepared. All other reagents and solvents (HPLC grade) were purchased from Sigma Aldrich. Water was deionized before use. Methanol was purified using a puresolv (innovative technology inc.) solvent purification system. All other chemicals were used without further purification.

Synthesis of silica nanoparticles. The preparation of small and large SiO_2 nanoparticles was carried out applying the Stöber-process and is described in chapter 3 as well as in the publication of Sajjad et. al. [S3].

The prepared colloidal dispersions were further used for nanoparticle surface functionalization or isolated as unmodified powders as described in the work of Sajjad et. al. [S3].

Surface functionalization of silica nanoparticles. The SiO_2 nanoparticles were surface modified with organosilane coupling agents by utilizing a method described in literature [13], a quasi $in-situ$ modification. Thereby, the nanoparticle sols with removed NH_3, prepared as described in our previous publication [S3] have been directly used. First, 0.1 mL NH_4OH conc. were added to the freshly prepared silica sol under stirring, followed by the addition of the trimethoxysilane coupling agent (e.g. dodecyltrimethoxysilane) to result in a 7.5 mM solution which was stirred for 48 h. The particles were then isolated by concentrating the dispersion via solvent removal and centrifugation at 8000 rpm. Afterwards, they were washed three times with ethanol (centrifugation at 8000 rpm) and dried over P_2O_5 at 5 mbar for 24 h.

The synthesis of 10-(trimethoxysilyl)decyl methacrylate and preparation of 10-(trimethoxysilyl)decyl methacrylate (MA-C10-TMS) are described in detail in the thesis of Feichtenschlager [120].

Preparation of nanocomposites

For the preparation of polystyrene nanocomposites via $in-situ$ bulk polymerization, 3 mL styrene, for each sample, was mixed with 27 mg dibenzoyl peroxide (DBPO), to obtain a 1 wt% initiator containing solution. Then, the particles were added and stirred for 1 h for particle surface wetting. Afterwards, the mixtures were ultrasonificated for 5 min in an ultrasound cleaning bath and heated to 80°C for 16 h to obtain

the nanocomposite materials. After removal from the glass vessel, nanocomposite material samples in form of disks with 2.4 cm diameter and 1.0-1.5 cm height could be yielded. Characterization details of the polymer matrix obtained by differential scanning calorimetry (DSC) and gel permeation chromatography (GPC) are listed in the thesis of Feichtenschlager [120].

For the preparation of PMMA nanocomposites via $in-situ$ bulk polymerization, 2.5 mL methyl methacrylate, containing 0.05wt% of the initiator azo-bis-isobutyronitrile (AIBN) (from a freshly prepared stock solution) were put into the reaction vessels. Then, the particles were added to this solution and it was stirred for 1 h for surface wetting of the particles. Afterwards, the mixtures were ultrasonificated for 5 min in an ultrasound cleaning bath and heated to 55°C for 16 h as a pre-polymerization phase. Then, the reaction mixtures were heated at 80°C for 24h to obtain the final materials. After removal from the glass vessel, nanocomposite material samples in form of disks with 2.4 cm diameter and about 1.0 cm height could be yielded. Characterization details of the polymer matrix obtained by differential scanning calorimetry (DSC) and gel permeation chromatography (GPC) are listed in the thesis of Feichtenschlager [120].

Methods

SAXS measurements were performed under vacuum conditions using a rotating anode X-Ray generator with a pinhole camera (Nanostar, Bruker AXS) with Cu K_α radiation monochromatized and collimated from crossed Goebel mirrors and a 2D position sensitive detector (Vantec 2000). The sample to detector distance was varied from 13 cm to 107 cm to cover a range of the scattering vector q of 0.05-15 nm^{-1}. All SAXS patterns were radially averaged and corrected for background scattering to obtain the scattering intensities in dependence on the scattering vector $q = 4\pi/\lambda \sin\theta$, where 2θ is the scattering angle and λ =0.1542 nm the X-Ray wavelength.

Ultra microtome-thin-cuts with a thickness of about 100 nm were performed on "Ultra cut E" (Leica) instrument at room temperature. TEM images were recorded on a JEOL JEM-100CX and on a FEI TECHNAI G20 transmission electron microscope.

5.1.3 Theory

For the calculation of the particle sizes from the SAXS profile, a simple approach is a product of a mean form factor and a so-called effective structure factor [36].

$$I(q) = I_0 V_0^2 \bar{P}(q,r) S_{eff}(q) \tag{5.1}$$

For the mean form factor, a theoretical approach for spherical particles with a Gaussian size distribution can be used.

$$P(q) \propto \int dR \left(\frac{4\pi}{3}R^3\right)^2 exp\left(-\frac{1}{2}\frac{(R-r)^2}{\sigma^2}\right)\left(3\frac{\sin qR - qR\cos qR}{(qR)^3}\right)^2 \qquad (5.2)$$

The interference of the scattering of particles contributes a structure factor for weakly aggregated system, in this work delivered by the hard-sphere model by the Percus-Yevick approximation [42]. Two parameters, the hard-sphere radius R_{HS} and a mean hard-sphere volume fraction η [43, 77] are included in the structure factor

$$S(q) = \frac{1}{1 + 24\eta G(2R_{HS}q)/(2R_{HS}q)} \qquad (5.3)$$

with the function $G(2qR_{HS})$ being defined by Kinning and Thomas [43]. The hard-sphere diameter $2R_{HS}$ gives information on the correlation distance of particles within a cluster or an aggregate and the hard-sphere volume fraction η defines a dimension for the probability to find particles in vicinity. Therefore, η describes the degree of agglomeration of the modified nanoparticles - the lower η, the higher the homogeneity. Fitting was performed by the appropriate software "Mathematica".

5.1.4 Results
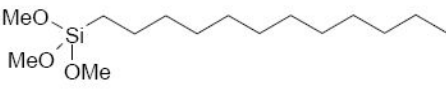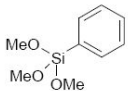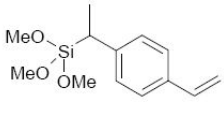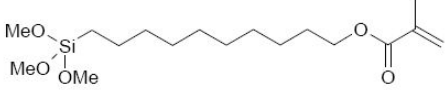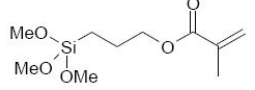
Nanoparticles

In this chapter, SiO_2 nanoparticles in two different size ranges with varying surface-functionalization were applied to study the nanoparticle dispersion structure in PS and PMMA. To investigate a possible influence of nanoparticle size and curvature on the agglomeration tendency, a significantly different size with a ratio of about 1:10 was synthesized, i.e. particles with a size of about 5 nm for small and 50 nm for large silica nanoparticles.

Chemical tailoring of the nanoparticle surface with coupling agents. For each polymer system, specific organic moieties were attached to the inorganic particle surface and their effect on the particle-polymer-interface was investigated. Five chemical types of organic moieties were used for the interface tailoring in the nanocomposites (three of them for PS and four for PMMA) to obtain a highly homogeneous dispersion of the particles in the matrix. The organic moieties were modified using trimethoxysilane as anchor group. All coupling agents and their corresponding abbreviations are listed in Table 5.1.

Table 5.1: List of the studied surface modifications.

capping agent formula	capping agent name	abbreviation
	Dodecyl trimethoxysilane	DTMS
	phenyl trimethoxysilane	PhTMS
	(1-(4-vinylphenyl)ethyl) trimethoxysilane	Styr-TMS
	(10-methacryloyl)oxydecyl trimethoxysilane	MA-C10-TMS
	(3-methacryloyl)oxypropyl trimethoxysilane	MA-C3-TMS

The idea was to use hydrophobizing reagents such as DTMS to adapt the polar nanoparticle surface to the less polar matrices. Furthermore, the use of chemical moieties, which resemble structurally to the matrix such as Ph- and Styr- for PS and MA- for PMMA, should enable a good compatibility of the interface. Furthermore, the use of polymerizable end groups (Styr-, MA-) enables a covalent linkage between matrix and particles and surface grafting through allows a strong interfacial compatibility through tethered polymer chains [142]. Finally, the variation of the spacer chain length (MA-C3-TMS vs. MA-C10-TMS) should allow a fine-tuning of the particle surface hydrophobicity. The goal is to find out general rules how these chemical surface parameters influence the nanoparticle dispersion behavior.

Nanocomposites

Characterization of nanocomposites by TEM. PS and PMMA nanocomposites have been prepared via $in-situ$ polymerization by dispersing the nanopowders in monomer and subsequent free radical bulk polymerization.

Photographs of typical thus obtained bulk samples with a 10-15 mm thickness are shown in Figure 5.1. Where the pristine matrices are transparent, the nanofiller containing samples are non-transparent. This is a clear indication on the presence of nanoparticle agglomerates. Some samples were pressed into films (30°C above T_g) for a more unique comparison of the amount of transparency: Figure 5.2 shows that

for 0.25 mm thick films, the MA-C10-TMS-modified particle containing samples are transparent, whereas the unmodified particle samples are non-transparent and large agglomerates are even visible to the unaided eye. This single example already gives a clue on the importance of the chemical surface group for the homogeneity of the final nanocomposite.
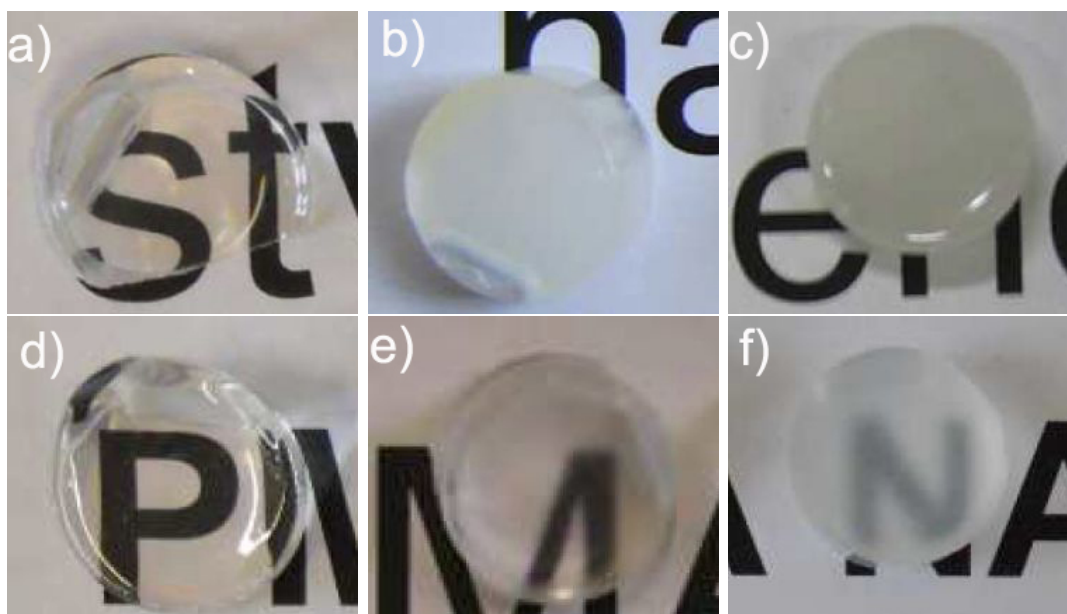

Figure 5.1: Photographs of nanocomposites containing unmodified and modified small silica nanoparticles leading in some cases to less transparent or even opaque materials. Upper row: a) PS blank, b) 5 wt% SiO$_2$ unmodified, c) 5 wt% Styr-TMS@SiO$_2$ in PS. Lower row: d) PMMA blank, e) 5 wt% SiO$_2$ unmodified, f) 5 wt% MA-C10-TMS@SiO$_2$ in PMMA.
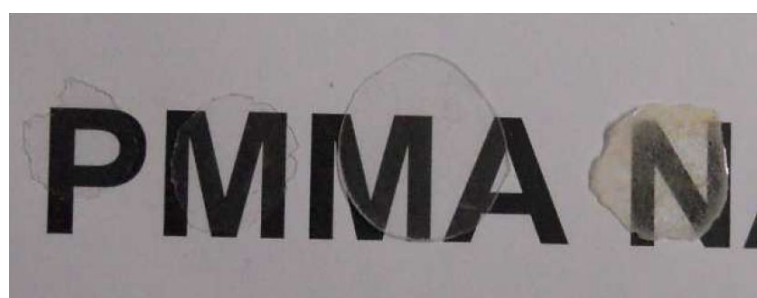
Figure 5.2: Photograph of PMMA nanocomposite films (0.25 mm thickness) containing (from left to right) 0 wt%, 3 wt% MA-C10-TMS@SiO$_2$ small, 5wt% MA-C10-TMS@SiO$_2$ small and 5wt% unmodified SiO$_2$ small nanoparticle filler.

Furthermore, representative TEM images of ultramicrotome thin cuts visualize the specific influence of the respective surface group on the dispersion quality of the nanocomposites (Figure 5.3). For PMMA and PS nanocomposites a general trend is visible: Unmodified large nanoparticles build micron sized agglomerates distributed over the whole material. Smaller agglomerates were obtained when a surface modification has been applied to hydrophobize the hydrophilic SiO_2 surface (DTMS). A still smaller amount of agglomeration (agglomerate size less than one micron) could be obtained for the PhTMS modification. In this case the phenyl group modified particles are embedded into the structurally similar PS polymer matrix. When the surface modification additionally contained polymerizable (methacrylate- or styryl-) end groups, the dispersion quality was further enhanced significantly. Hardly any agglomeration could be detected by TEM in this case.

Structural investigations using SAXS. The PS and PMMA nanocomposites filled with 3 wt%, 5 wt% and 10 wt% of surface modified nanoparticles have been investigated by SAXS. Typical scattering curves are shown for 5 wt% filler content as an example, together with the corresponding fit curves using Eq. 5.2 and Eq. 5.3. are shown in Figure 5.4 for PS and Figure 5.5 for PMMA. The upper limit in the diagrams is q=5 nm^{-1}, as the only distinct feature up to 20 nm^{-1} is the short range order peak of the silica tetraeders within the silica nanoparticles.

From these scattering data, an indicator for the quality of dispersion of nanoparticles, the hard-sphere volume fraction η, was calculated by combining the form factor for spheres with a Gaussian distribution and a structure factor as described. A complete list of the results can be found in Table 5.2.

The hard-sphere volume fractions for different surface-modified silica in PS are presented in Figure 5.6 and for PMMA in Figure 5.7 to better visualize the influence of the surface functionalization on the agglomeration behavior: A lower hard sphere volume factor was observed for the Styr-TMS@SiO_2 nanocomposite system for both size ranges (Figures 5.6 a,b). The improvement in dispersion compared with the similar PhTMS is significant for both the small and the large SiO_2/PS system, as PhTMS and Styr-TMS are only distinguishable by the polymerizable group. Differently, DTMS leads even has a negative effect and leads to a higher tendency to agglomerate.

Silica particles modified with DTMS and PhTMS were also used for PMMA nanocomposites. Additionally, coupling agents with different alkyl chain length and a polymerizable group, MA-C3-TMS and MA-C10-TMS, were prepared and incorporated in PMMA to investigate the effect of polymerizable groups. Figure 5.7 shows that the polymerizable group leads to a better dispersion of the nanoparticles in PMMA, i.e. a lower hard sphere volume fraction for small as well as large SiO_2 nanoparticles.

It is further visible that the length of the alkyl chain controls the agglomeration behavior: A short alkyl chain with methacryloyl seems to be advantageous for the SiO_2/PMMA systems, independent from the nanoparticle size. If the long alkyl
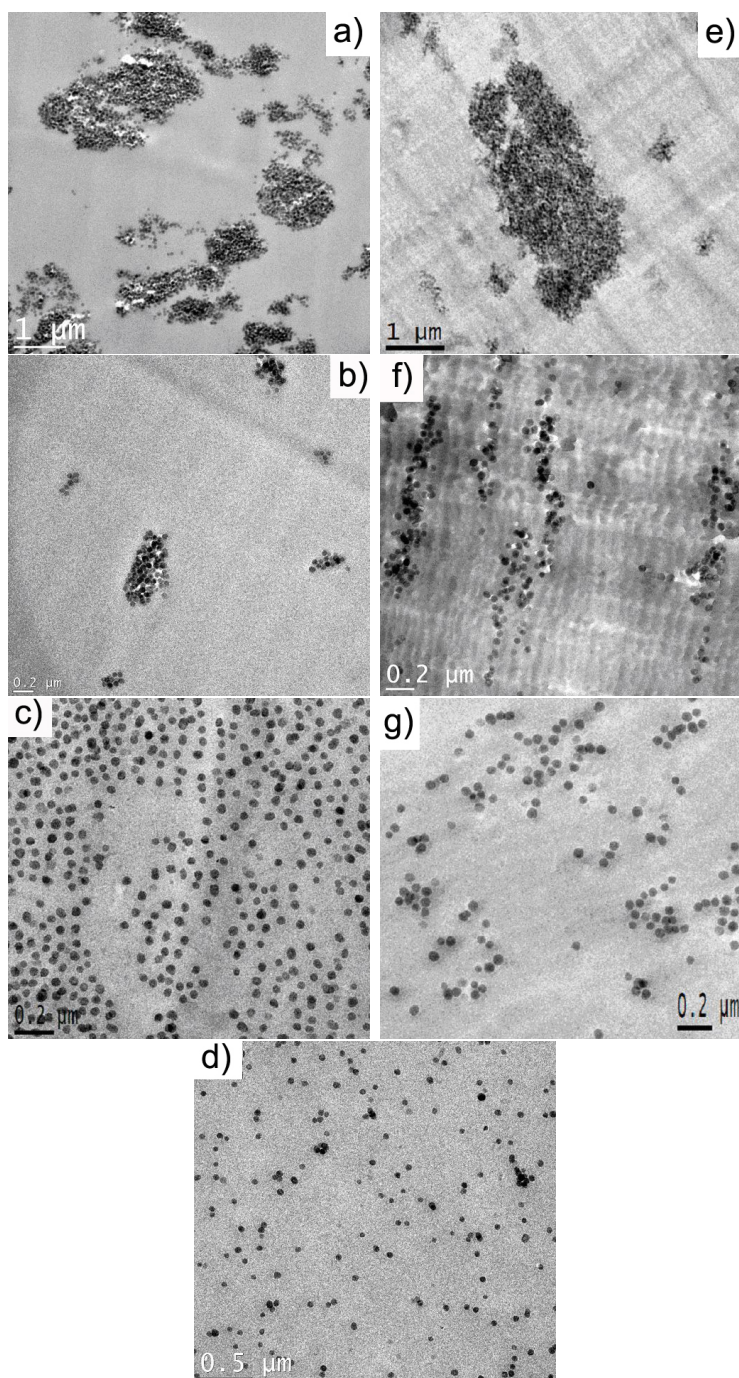
Figure 5.3: Representative TEM-images of ultramicrotome-cuts (100-300 nm thickness) of 5 wt% large SiO_2 nanoparticle, with different surface modification embedded in PS and PMMA. a) 5 wt% SiO_2 unmodified, b) 5 wt% DTMS@SiO_2, c) 5 wt% MA-C10-TMS@SiO_2, d) 5 wt% MA-C3-TMS@SiO_2 in PMMA and e) 5 wt% SiO_2 unmodified, f) 5 wt% DTMS@SiO_2, g) 5 wt% Styr-TMS@SiO_2 in PS.
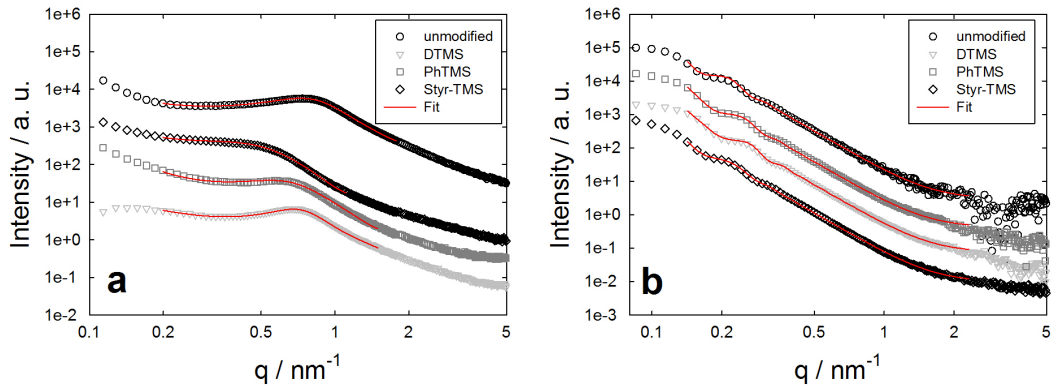
Figure 5.4: SAXS scattering curves, exemplarily shown for 5 wt% inorganic nanofiller content of PS nanocomposites containing a) small SiO_2 and b) large SiO_2.
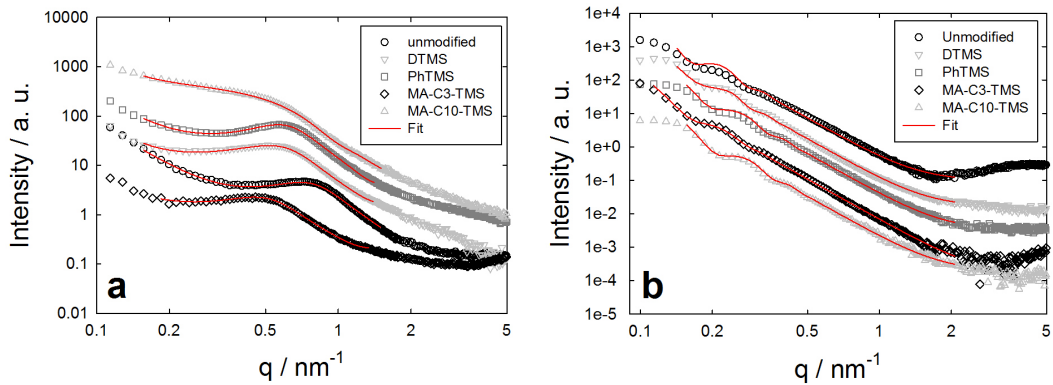
Figure 5.5: SAXS scattering curves, exemplarily shown for 5 wt% inorganic nanofiller content of PMMA nanocomposites containing a) small SiO_2 and b) large SiO_2.

Table 5.2: Hard sphere volume fraction values η for different amount (in wt%) of surface modified SiO_2 nanoparticles in PS and PMMA.

	size	wt%	hard-sphere volume fraction η			
			unmodified	DTMS	PhTMS	Styr-TMS
PS	small	3	0.166	0.257	0.168	0.153
		5	0.205	0.238	0.152	0.087
		10	0.186	0.239	0.159	0.084
	large	3	0.266	0.405	0.308	0.268
		5	0.364	0.404	0.327	0.255
		10	0.308	0.418	0.311	0.239
		wt%	unmodified	DTMS	PhTMS	MA-C3-TMS	MA-C10-TMS
PMMA	small	3	0.254	0.128	0.149	0.136	0.165
		5	0.237	0.171	0.200	0.166	0.176
		10	0.184	0.112	0.170	0.079	0.179
	large	3	0.248	0.379	0.283	0.128	0.294
		5	0.192	0.351	0.301	0.190	0.271
		10	0.230	0.285	0.292	0.112	0.275
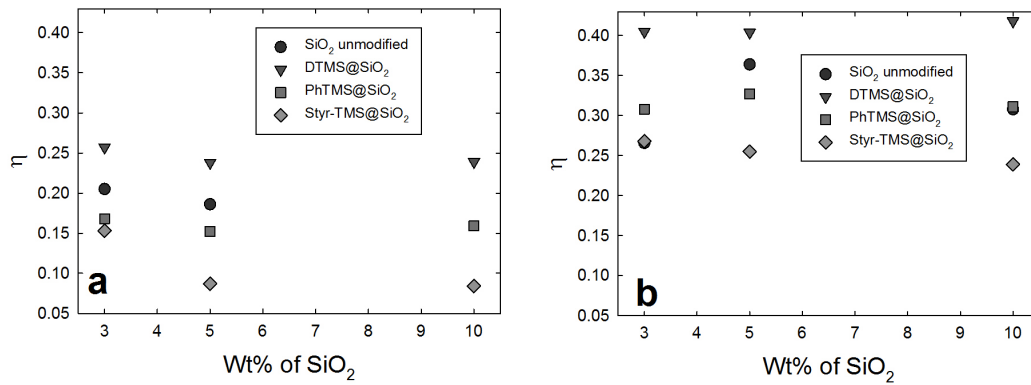
Figure 5.6: Hard-sphere volume fraction η of a) small and b) large SiO_2 nanoparticles with different surface-functionalizations embedded in PS with different weight percentages.

chains does not have a polymerizable group, as is the case for DTMS, high values for η can be observed for the large DTMS@SiO$_2$/PMMA systems.
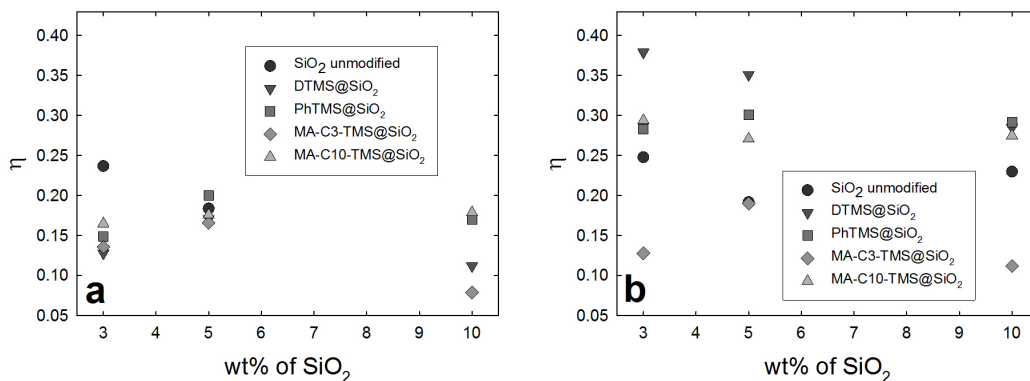

Figure 5.7: Hard-sphere volume fraction η of a) small and b) large SiO$_2$ nanoparticles with different surface-functionalizations embedded in PMMA with different weight percentages.

5.1.5 Discussion

The effect of surface-functionalization on the dispersion of nanoparticles is directly visible in the TEM images (Figure 5.3). Whereas PS and PMMA nanocomposites with unmodified silica nanoparticles show micron sized agglomerates (Figure 5.3a and 5.3e), samples with modified silica show smaller (Figure 5.3b and 5.3f) or hardly any agglomerates (Figure 5.3c, 5.3d, and 5.3g). The coupling agents DTMS and PhTMS reduced the size of the agglomerates, however, agglomeration could not be completely avoided. A further improvement was the use of polymerizable groups together with surface-functionalization of nanoparticles, where within the observed volume of a few nm^3, highly dispersed large silica nanoparticles could be observed (Figure 5.3c, 5.3d, and 5.3g). A possible interpretation is that cross-linking of the nanoparticles with the polymer matrices was achieved. This overcomes a concurrent effect, the minimization of surface energy by denser packing of nanoparticles themselves. Enthalpy can thereby play a strong role for higher agglomeration as it is an important parameter for the dispersion of nanoparticles in polymers [89]. The amount of dense packing is described numerically by the hard sphere volume fraction, but is also directly visible in the SAXS curve by a characteristic hump being more pronounced the denser the packing (Figures 5.4 and 5.5). The polymerizable group significantly reduces the amount of agglomeration in the case of Styr-TMS in the SiO$_2$/PS system (Figure 5.6). Here, the chemical linkage is probably very effective and leads to a good dispersion of the nanoparticles, which is also visible in the TEM images in Figure 5.3. The highest value of η, which indicates the highest

agglomeration, is found in the DTMS modified systems. It is observed in PS and for PMMA nanocomposites for small as well as for large nanoparticles. A possible interpretation of this effect is that the long alkyl chains order on the nanoscopic surface of the particles, which leads to the formation of interparticle bilayers as studied in the published work of Feichtenschlager et. al. [119] and enhances the interaction of nanoparticles. This effect is even more pronounced in comparison to unmodified silica nanoparticles (Figure 5.6).

The formation of bilayers is inhibited by the curvature of nanoparticles, which is one explanation for the stronger interaction and agglomeration of large nanoparticles in the system DTMS@SiO$_2$ in PS and PMMA. However, in the literature, also the importance of the ratio of particle radius to radius of gyration of the polymer $r_{particle}/R_g$ was pointed out [143, 144]. If $r_{particle}$ is too large compared to R_g (depending on the molecular weight of the polymer matrix), the matrix macromolecules cannot surround the particles and mixing of the two components is hindered [137, 144]. These are possible reasons to explain the observed effect that large nanoparticles exhibit a higher tendency to agglomerate than small ones.

Similar to Styr-TMS@SiO$_2$ in PS, a comparable improvement of the dispersion quality was obtained in the SiO$_2$/PMMA system by attaching methacryloyl as polymerizable group to the alkyl chain of the coupling agent (Figure 5.7). The length of the alky chain seems to be decisive: Whereas no improvement was found for the long alkyl chain, this was definitely the case for short alkyl chains with methacryloyl as polymerizable group in the PMMA matrix. Probably, the long chains are able to order themselves [143], and despite the polymerizable group this increases the tendency to agglomerate in comparison to the short alkyl chains, which are advantageous in this case. Differently, PhTMS has nearly no effect on the quality of the dispersion.

No specific effect by increasing the amount of nanoparticles on the hard-sphere volume fraction and thus the agglomeration behavior could be found, though it was varied between 3 and 10 wt%. A possible increases agglomeration at higher weight percentages may be speculated, but was not investigated in this work.

5.1.6 Conclusion

The dispersion of surface-functionalized silica nanoparticle was investigated in two different size ranges incorporated in two different polymer matrices, polystyrene and poly(methyl methacrylate) by TEM and SAXS.

Surface functionalization can increase the tendency to agglomerate as shown for the DTMS@SiO$_2$ system in Figure 5.6 for PS and Figure 5.7) in PMMA, probably by the order of long alkyl chains on the surface of the nanoparticles. Surface functionalization can also decrease the tendency to agglomerate and thus improve the dispersion behavior, in particular, if polymerizable end groups are attached, which interact with the polymer (shown for DTMS and PhTMS with polymerizable groups

such as Styr- for PS and methacryloyl for PMMA).

The tendency to agglomerate is in general slightly higher for large than for small nanoparticles. This origin could either be enthalpic reasons, which lead to a stronger interaction between particles than between particle and polymer, or the order of surface functionalization at the surface of nanoparticles, which is decreased by the high curvature of small nanoparticles.

Therefore, the optimum choice of the end group of the surface functionalization is crucial for improving the dispersion of nanoparticles in polymers. This concerns not only the end group itself, but also the length of the spacer, the size of the nanoparticle and the radius of gyration of the polymer. In general, polymerizable groups at coupling agents are advantageous to obtain a higher dispersion quality than the use of non-polymerizable groups.

5.2 The influence of varying surface-functionalization of zirconia nanoparticles on the dispersion quality in PMMA nanocomposites

An overview is given for Poly(methyl methacrylate) (PMMA) containing surface-functionalized zirconia nanoparticles prepared by $in-situ$ polymerization of zirconia dispersions in methyl methacrylate (MMA). To investigate the influence of nanoparticle sizes on the dispersion, two different sizes of zirconia nanoparticles, one in the lower nanometer range of about 5 nm and one in the upper nanometer range of about 30 nm, were prepared. The zirconia nanoparticles were surface-functionalized with two different coupling agents, consisting of an anchor group, a spacer of an alkyl chain in varying length (C2 and C10) and a methacrylic end group. Structural investigations were carried out using SAXS and TEM. Homogeneous dispersion of the zirconia nanoparticles could be observed at lower wt% content with a lost of transparency at higher wt% due to small agglomerates. SAXS studies verified that shorter spacer lead to higher dispersion of the nanoparticles in the polymer matrix. Furthermore, nanoindentation tests were made to study the influence of nanoparticle size, surface-functionalization and nanofiller content on the hardness.

5.2.1 Introduction

Poly(methyl methacrylate) (PMMA) is a widely used transparent amorphous polymer in research and industry [145, 146]. The use of PMMA as an construction material has several advantages such as flexibility, high strength or stability [137, 142]. However, it has limiting properties including a lack of toughness [147] and low heat resistance [148]. Various inorganic nanofillers, e. g. silica [142], zirconia [146]

or titania [149], have been used for inorganic-organic PMMA nanocomposites to enhance several thermomechanical or mechanical properties. The great challenge has always been a homogeneous dispersion of the inorganic phase throughout the polymer matrix to obtain nanoparticle related reinforcement effects [150]. This problem can be solved by using coupling agent molecules attached to the surface of the nanoparticles, which show structural and chemical similarities to monomer and polymer and therefore allow an enhanced dispersion due to an optimum interaction with the organic phase. An example for anchor groups is phosphonic acid, forming strong covalent bonds between the metal oxide nanoparticle substrate and the organic moiety. An advantage of this anchor group, contrary to silane coupling agents or carboxylic acids, is the adoption for almost every transition metal oxide, such as TiO_2, [15] ZrO_2, [14, 151, 152] Y_2O_3, [153] or Fe_3O_4 [116] as discussid in literature. If a chemical linkage between organic and inorganic part can be obtained, e.g. via methacrylate endgroup, homogeneity can be further improved due to the higher possibility of a chemical linkage between polymer chain and surface-modified nanoparticle during the $in-situ$ polymerization [142, 146].

Therefore, organophosphorus coupling agents methacrylic acid end groups should provide good grafting through properties to the inorganic surfaces and thus enable homogeneity and interfacial adhesion. These molecules have been studied to be used for ZrO_2 dental fillers and seem to be highly promising [8]. Furthermore, the variation of the alkyl spacer chain length should allow a finetuning of hydrophobicity of the nanoparticle surface and thus of interfacial properties within the nanocomposite material [154].

In this chapter, PMMA nanocomposites filled with surface-modified zirconia, containing strongly bond methacrylate surface groups, were studied by SAXS, TEM and hardness tests. The surface of the nanoparticles was modified using phosphonic and phosphoric acid as anchor groups. The aim is the optimization of the dispersion structure and mechanical properties by investigation of the role of chemical interface design in nanocomposite materials.

5.2.2 Experimental

The solvents (HPLC grade) and chemicals were purchased from Sigma Aldrich and ABCR. Water was de-ionized before use. Methanol was purified using a PureSolv (innovative technology inc.) solvent purification system. All other chemicals were used without further purification.

Nanoparticles

Small zirconia nanoparticle powder was prepared according to a literature known procedure [69] and as mentioned in chapter 3.2.

Diethyl-methacryloxyethylphosphonate was synthesized by a known process described by Francová et. al. [127]. The synthesis of 2-Mmthycryloyloxy-1-ethylphos-

phonic acid and 1-methacryloyloxy decyl-10-phosphoric acid monoester are described in the thesis of Bernhard Feichtenschlager [120].

Preparation of the nanocomposites

For the preparation of PMMA nanocomposites via $in-situ$ bulk polymerization, 2.5 mL methyl methacrylate, containing 0.05 wt% of the initiator azo-bis-isobutyronitrile (AIBN) (from a freshly prepared stock solution) were put into small 15 mL flat bottom reaction vessels. Then, the particles were added to this solution and it was stirred for 1 h for surface wetting of the particles. Afterwards, the mixtures were ultrasonificated for 5 min in an ultrasound cleaning bath and heated to 55°C for 16 h as a pre-polymerization phase. Finally, the reaction mixtures were heated at 80°C for 24h to obtain the final materials. After removal from the glass vessel, nanocomposite material samples in the form of discs with 2.4 cm diameter and about 1.0 cm thickness were obtained.

5.2.3 Characterization methods

Transmission electron microscopy (JEOL JEM-100CX and on a FEI TECHNAI G20 transmission electron microscope at the University Service Centre for Transmission Electron Microscopy, Vienna University of Technology, Austria) was used to investigate on the dispersion structure of the nanocomposites. Ultra thin sections of about 80-150 nm thickness were cut using an ultra microtome "Ultra cut E" (Leica) instrument at room temperature.

Small angle X-ray-scattering (SAXS) measurements were performed under vacuum in transmission geometry using a rotating anode X-Ray generator with a pinhole camera (Nanostar, Bruker-AXS) with Cu KK$_\alpha$ radiation. The beam was monochromatized and collimated from crossed Goebel mirrors and analyzed by a 2D position sensitive detector (Vantec 2000). The sample to detector distance was varied from 13 cm to 107 cm to cover a range of the scattering vector q of 0.1-15 nm^{-1}. All SAXS patterns were radially averaged and corrected from background scattering to obtain the scattering intensities in dependence on the scattering vector q = $4\pi/\lambda\sin\theta$, where 2θ is the scattering angle and $\lambda = 0.1542$ nm the X-ray wavelength. For the calculation of the particle sizes and strength of agglomeration from the SAXS profile, a theoretical model for spherical particles with a Gaussian size distribution was used for the form factor [36] in combination with the hard-sphere model for the structure factor to account for the agglomeration. The Percus-Yevick approximation [42] allows the quantification of the agglomeration behavior with a mean radius of hard spheres R_{HS} and the hard-sphere volume fraction η giving the probability to find particles in vicinity [43, 77]. Fitting was performed by the software "Mathematica".

Hardness was measured with the conventional Vickers hardness tester using a square-based pyramid diamond indenter with an angle of 136° between the opposite

faces at the vertex, which was pressed into the surface of the test piece using a small force of HV1. The force was maintained for 30 s and subsequently the diagonal lengths were measured. The values were converted to Vickers hardness number. An average of 10 indents was taken as the representative value for the material.
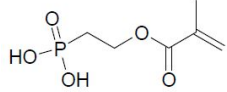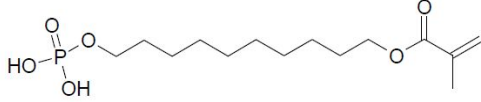
5.2.4 Results and Discussion

For the preparation of these nanocomposites, coupling agents with additional methacrylate end groups were used, MA-C2-PPA and MA-C10-PA (Table 5.3). MA-C10-PA is the only used organophosphoric acid used for zirconia as anchor group in this work, as all the other coupling agents have organophosphonic acid. The reason to choose a phosphoric acid group was the facileness of the synthesis via phosphoric acid mono esterification. The result of the attachment of phosphoric acid monoester molecules is similar to phosphonic acids [155, 156].

To visualize the influence of polymerizable end groups on the dispersion, TEM images of MA-C10-PA modified ZrO_2 are compared with DPPA@ZrO_2 in Figure 5.8, which is of a similar spacer length apart from the methacrylate end group, both nanoparticles systems embedded in PMMA. DPPA is only shown for demonstration reasons, as the high tendency for large agglomeration due to SAM formation, which was discussed in the previous chapters 4 and 5.1, is clearly visible comparing to the MA-C10-PA@ZrO_2 system. There are small agglomerates visible for the MA-C10-PA@ZrO_2/PMMA system, however, in generall the distribution is rather homogenous.

The nanocomposites, filled with 3, 5 and 10 wt% of surface modified nanoparticles have been additionally investigated by SAXS. The dispersion quality of the nanoparticles in the polymer matrix is described by the hard-sphere volume fraction η which gives information about the probability to find particles in vicinity. The lower the value for η, the better the particles are dispersed. As shown in Figure 5.9 nanocomposites with MA-C2 modified zirconia are better dispersed compared with MA-C10 modified zirconia in both size ranges in PMMA. This result can be explained by the different length of the alkyl chain spacers. The short alkyl chains achieve an enhanced dispersion of the nanoparticles in the PMMA, probably due to a better interfacial adhesion with the surrounding matrix. There is also a higher probability for longer alkyl chains on the surface of nanoparticles to interact with the alkyl-chains of the neighbouring particles, which could lead to a higher tendency to agglomerate [S2]. Not only the surface-modification but also the size of the zirconia influences the dispersion quality. A significant difference of the value for η between large and small nanoparticles is visible in Figure 5.9. Large zirconia are generally better dispersed than small zirconia, which can be caused by the ratio of particle radius to radius of gyration of the polymer $r_{particle}/R_g$ [143, 144]. It can be summerized that the distribution of the particles within the polymer first depends on their size and second on the length of the polymer chains. A further effect, vis-

Table 5.3: Organophosphorus coupling agents used for the surface modification of ZrO$_2$.

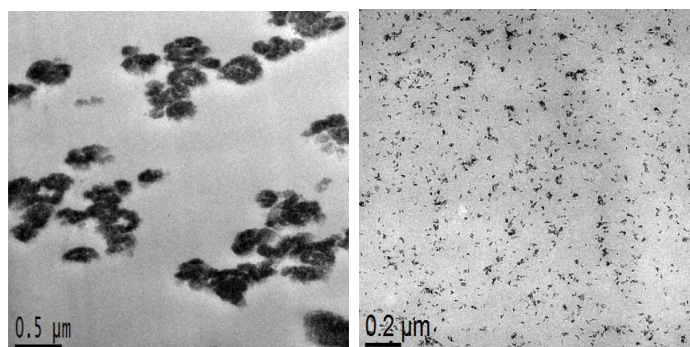| capping agent formula	capping agent name	abbreviation
	2-(methacryloyloxy)ethyl phosphonic acid	MA-C2-PPA
	10-(phosphonooxy)decyl methylacrylate	MA-C10-PPA

Figure 5.8: Representive TEM micrographs of ultra thincuts (about 100-300 nm thickness) of PMMA/ZrO$_2$ large nanoparticle nanocomposites, containing 5 wt% inorganic filler; left: DPPA@ZrO$_2$, right: MA-C10-PA@ZrO$_2$.

ible in Figure 5.9, is the decrease of η for large zirconia at high filler content of 10 wt%. This can be explained by a possible interplay of viscosity shear force effects and interparticle interactions in the suspension. Kamibayashi et. al. observed that the viscosity can increase drastically at high filler contents of above 7 wt%, which depends on the nanoparticle size and the polymer radius of gyration [157]. Therefore, due to the increasing viscosity and increasing shear forces, agglomerates can break, which can result in a homogeneous material. This effect seems to occur for large nanoparticles whereas the small nanoparticles are rather uneffected and nearly do not vary in their η values. This was also explained by Kamibayashi et al. as different nanoparticle sizes result in different viscosities of the suspensions, which could change the agglomeration behavior [157]. Furthermore, it is surprising that in this study large nanoparticles are in general better dispersed than small ones. An assumption is that the large asymmetric nanoparticles like zirconia are in an optimum size range for an enhanced correlation with the surrounding polymer. Smaller particles could have a higher tendency to accumulate between the polymer chains.
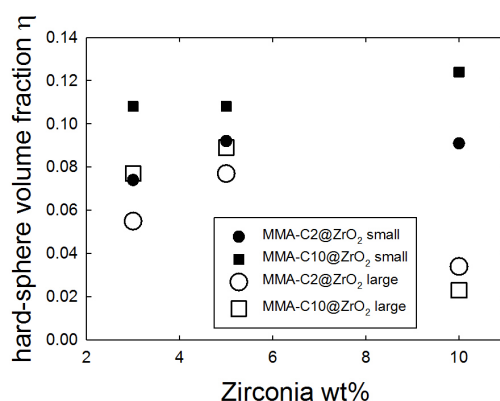
Figure 5.9: Hard sphere volume fraction η for modified ZrO_2 embedded in PMMA.

The ability of the material to resist local surface deformation, the hardness, was investigated by indentation tests for neat PMMA as well as Zirconia/PMMA nanocomposites with different wt% of nanofiller content. The results are presented in Figure 5.10. The four systems, varying in size (small and large) and cappling agents (MA-C2-PPA and MA-C10-PA), show significant different trends in increasing hardness of the PMMA nanocomposite. PMMA containing small MA-C10-PA@ZrO_2 result in a high hardness, even constant between 3 and 10 wt% nanofiller content, followed by large MA-C2-PPA@ZrO_2. In the case of large MA-C10-PA@ZrO_2, which show hardly any increase of the hardness between 3 and 5 wt%, an initially opposite behavior compared with small MA-C10-PA@ZrO_2 is visible. Small MA-C2-PPA@ZrO_2 give a slight linear increasing trend in hardness. At 10 wt% a nearly identical hardness for all systems was obtained. Neither size nor surface-modification or agglomeration behavior seems to have an exclusive influence on the improvement

of the hardness. It can be assumed that the hardness improvement is a result of a complex interplay of the various parameters. Hu et. al. described in their work the effect of 4 nm ZrO_2 nanoparticles on the hardness of the PMMA nanocomposites by a pendulum hardness test. They observed three evolutional regions of hardness development depending on the nanofiller content. The first two regions, where the pendulum hardness quickly increases and then stays nearly constant, were attributed to crosslinking-dominated effects, where nearly all PMMA chains are restricted by the nanoparticles, but the zirconia content is not high enough to cause a distinct increase of hardness. The third region, a continous raise of the pendulum hardness with increasing filler content, was attributed to a nanoparticle-dominated effect, where now a correlation between high ZrO_2 content and increasing pendulum hardness is observed. [158]. It has to be investigated in future how surface-functionalization and nanoparticle size can influence the increasing trends of hardness due to crosslinking- and nanoparticle-dominated phases. One can assume that at a nanofiller content of 10 wt% or higher, the nanofiller content is crucial for hardness improvement, independentof the size or the surface-functionalization.
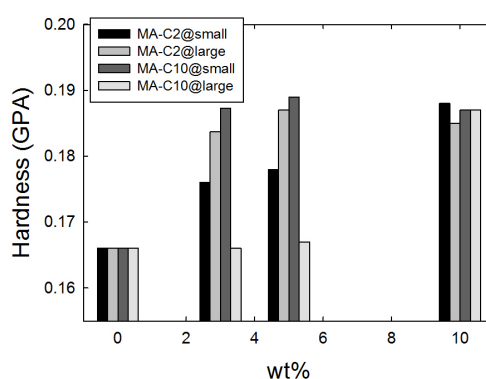
Figure 5.10: Hardness of PMMA nanocomposites with modified zirconia nanoparticles.

5.2.5 Conclusion

PMMA nanocomposite samples containing zirconia nanoparticles, which were prepared in two different size ranges and surface-functionalized with two different coupling agents, were obtained by $in - situ$ polymerization. Organophosphoric and organophosphonic added coupling agents were used, containing C2 or C10 alkyl chain spacers with a methacrylate end group, to enhance the dispersibility of the nanoparticles within the polymer matrix. A nearly homogenous distribution could be obtained for the zirconia nanoparticles modified with methacrylate end groups as shown by TEM photographs. The dispersion quality was investigated by SAXS, where the advantage of a shorter C2 alkyl chain in contrary to the longer C10 alkyl

chain could be observed for small as well as large nanoparticles. Longer C10 alkyl chains can tend to raise the interparticle interaction due to possible SAMs at the particle surface, which leads to the formation of agglomerations. The effect of the surface-modified nanoparticles on the hardness of the material was influenced by a complex relation between size, surface-functionalization, agglomeration behavior and viscosity shear forces. At a nanofiller content of 10 wt%, the hardness of all investigated systems became nearly the same, which can indicate, that at higher filler content only the amount of zirconia, independent by size or surface-functionalization, is crucial for the hardness enhancement.

5.3 The influence of interface chemistry on the dispersion behavior in epoxy resin nanocomposites

Amorphous spherical silica nanoparticles in two size ranges - one around 6 nm and the other around 50 nm - and crystalline non-spherical zirconia nanoparticles of a size of around 5 nm were used in this chapter to study the effect of surface modification on the homogeneity of epoxy resin nanocomposites. Trimethoxysilane coupling agents have been applied for the surface modification of the SiO_2 particles and phosphonic acid coupling agents were used for the ZrO_2 surface modification. For the systematic variation of the interaction strength between the nanoparticles and the polymer matrix, different end groups have been applied: diethyleneglycol monomethylether (DEG), 1,2-diol and epoxide. Their effect on the interface as well as on the dispersion quality were investigated by TEM and SAXS in dependence on different inorganic nanofiller contents of 3 wt%, 5wt% and 10 wt%. It could be proven that an optimization by variation of the coupling agent end group leads to an enhancement of the dispersion quality and therefere, to an homogeneous and transparent nanomaterial. The relation of particle-matrix interaction to particle-particle interaction has an enormous influence on the resulting material and can be controlled by the surface groups and by the nanoparticle type as well as size.

5.3.1 Introduction

Reinforced epoxy resins are widely used in technical applications, such as coating, because of their ability for good adhesion on various surfaces or the use in composites for light weight engineering materials, which was of great interest for the last decades [159]. Inorganic nanobuilding blocks such as nanoparticles or 1D nanoscopic layered systems [160] were investigated for the reinforcement in polymers to improve these materials [132]. However, a great challenge is the interfacial incompatibility of inorganic and organic compounds to mix homogeneously and therefore to achieve novel mechanical and optical effects [132, 161]. Transparent properties of the ma-

terial can be retained, even at different refractive indices of polymer and nanofiller, if the nanofillers are homogeneously dispersed in the polymer matrix [161], which is important for epoxy resin materials as coating applications.

In literature, high quality inorganic nanoparticles distributions in organic matrices are shown, which are obtained by powders or suspensions [162, 163, 164, 165]. In some cases, unmodified nanoparticles can be well dispersable with low effort, however, a specific organic modification leads to enhanced interfacial match and thus dispersion quality [136, 166]. Kang et. al. have studied an epoxy/silica system varying in different nanoparticle surface groups such as epoxides, amino groups or isocyanate groups resulting in materials with different dispersion quality and interfacial adhesion properties [166]. The need for an interfacial match in epoxy resin nanocomposites was then pointed out in previous studies by Haworth et. al. and Becker et. al. [160, 167].

The question is how a homogeneous dispersion can be obtained by a chemical tailoring of the inorganic-organic interface to maximize the particle-matrix interaction and minimize the particle-particle interaction. Then only low shear forces within the component mixture (e.g. magnetic stirring in the laboratory) would be necessary to obtain a high quality of dispersion, which has already been demonstrated in literature [164].

In this chapter, SAXS and TEM investigations were applied to follow the influence of the different chemical nanoparticle surface modifications on the dispersion behavior. On the one hand the well-known system of SiO_2 nanoparticles, which are widely used in industry, [163, 164, 165, 167, 168, 169] and allow to control the size, on the other hand, a hard material such as ZrO_2 nanoparticles with high optical density and a number of technical applications [152, 162, 170, 171] were cured $in-situ$ in the epoxy resin material. The coupling agent end groups were varied for a systematical study to investigate strong (covalent) interaction at the interface (epoxy or OH- groups), medium strong interaction (e.g. hydrogen bonding via OH groups), and weaker interactions (ethyleneglycol derivatives, polar interactions). The aim is a correlation of the physico-chemical composition of the inorganic-organic interface with the results of the dispersion quality observed by SAXS and TEM. The knowledge about this correlation can facilitate the development of novel nanocomposite systems.

5.3.2 Experimental section

Materials. All solvents (HPLC grade) and chemicals were purchased from Sigma Aldrich and ABCR. Water was deionized before use. Methanol was purified using a PureSolv (Innovative Technology inc.) solvent purification system. All other chemicals were used without further purification.

Instrumental analysis. Transmission electron microscopy (TEM) images were recorded on a JEOL JEM-100CX and on a FEI TECHNAI G20 transmission elec-

tron microscope. The powder samples were attached to Formvar copper grids by dispersing them in ethanol using an ultrasound cleaning bath, adding one drop on the copper grid and evaporating the solvent.

Small-angle X-ray-scattering (SAXS) measurements were performed under vacuum in transmission geometry using a rotating anode X-Ray generator with a pinhole camera (Nanostar, Bruker-AXS) with CuK_α radiation monochromatized and collimated from crossed Goebel mirrors and a 2D position sensitive detector (Vantec 2000). Measurements were carried out at two different distances (13 cm and 108 cm) to cover a wide q range. All SAXS patterns were radially averaged and corrected from background scattering to obtain the scattering intensities in dependence on the scattering vector $q = 4\pi/\lambda \sin\theta$, where 2θ is the scattering angle and λ =0.1542 nm the X-Ray wavelength.

The trimethoxysilane- and phosphonic acid coupling agent molecules with diethyleneglycol monomethylether moiety have been prepared as described in the published work of Sajjad et. al. [S3]. The preparation and characterization of the used capping agents can be found in detail in the thesis of Bernhard Feichtenschlager [120]. The nanoparticle synthesis is described in detail in chapter 3.

Silica nanoparticles were modified applying an $in-situ$ approach, directly from the prepared sols. Zirconia nanoparticles were modified using a post-modification approach as described in literature for titanium dioxide nanoparticles [15]. More details about the chemistry behind the surface modification can be found in the thesis of Feichtenschlager [120].

Amine cured bisphenol-F-based epoxy resin nanocomposites were prepared by a common procedure described in literature [172]. 2.0 g (7.03 mmol) bisphenol-F-diglycidylether was molten at 70°C and the particle powder was added, followed by magnetic stirring at 750 rpm for 2 h. A total of 0.2 g (1.94 mmol) diethylenetetramine were afterwards added to the reaction mixture which was immediately cast on a silicone grease coated stainless steel plate and cured at 120°C for 16 h to give sample plates of 1.2-1.5 mm thickness and 3-5 cm diameter.

5.3.3 Theory

The agglomeration behavior of the mixed monolayer endcapped nanoparticle powders was studied via Small Angle X-ray Scattering (SAXS).

Scattering intensities of weakly ordered structures are described by the simplified approach of the product of a mean form factor and a structure factor, $I(q) = I_0 V_0^2 \bar{P}(q) S(q)$. For the calculation of the particle sizes from the SAXS profile, a numerical approach for spherical particles with a Gaussian size distribution can be used for the form factor [36].

$$\bar{P}(q) \propto \int dR \left(\frac{4\pi}{3}R^3\right)^2 exp\left(-\frac{1}{2}\frac{(R-r)^2}{\sigma^2}\right)\left(3\frac{\sin qR - qR\cos qR}{(qR)^3}\right)^2 \qquad (5.4)$$

In the hard-sphere model, a structure factor for weakly aggregated systems is delivered by the Percus-Yevick approximation [42], which describes the interference of the scattering of particles with two parameters, a hard-sphere radius R_{HS} and a mean hard-sphere volume fraction η [43, 77]

$$S(q) = \frac{1}{1 + 24\eta G(2R_{HS}q)/(2R_{HS}q)} \tag{5.5}$$

with the function $G(2R_{HS}q)$ being defined by Kinning and Thomas [43]. The hard-sphere diameter $2R_{HS}$ gives information on the correlation distance of particles within a cluster or an aggregate and the hard-sphere volume fraction η on the probability to find particles in vicinity. Therefore, η describes the degree of agglomeration of the modified nanoparticles - the higher η, the stronger the agglomeration. Fitting was performed by the appropriate software "Mathematica".

5.3.4 Results

The surface-modified nanoparticle model systems use coupling agents to introduce a specific organic moiety to the nanoparticle surface and study the effect of the organic moiety at the particle-polymer-interface. Three chemical types of organic moieties attached to the inorganic particle surface for the interface tailoring in the epoxy nanocomposites were studied. A highly homogeneous dispersion of the particles in the matrix by enhancing the particle-matrix interaction have to be obtained for transparent nanocomposites. Therefore the following coupling agents were applied:

- (i) the diethyleneglycol (DEG) moiety which should allow an enhanced physical interaction of the modified particle surface with the organic matrix as DEG and matrix are both polar and (oligo)ethyleneglycols are highly miscible with epoxy resins [173].

- (ii) the widely used epoxide end groups which show physical properties to link the inorganic and organic surfaces [11] and, as they can chemically react with the formed polymer resin during the applied $in-situ$ curing approach, covalently link the particles to the organic matrix [167]. This should result in an enhanced dispersion.

- (iii) diol end groups as less reactive analogon to the used epoxide end groups which are the alcohol-end groups, which can also form a covalent bond to the epoxy resin during the curing process. Interactions via hydrogen bonds with the polar organic component are possible, [169] resulting in a intermediate strong interacting group (between DEG and epoxide).

For SiO_2 nanoparticle surface modification, the organic moieties were attached with a trimethoxysilane anchor group and the ZrO_2 nanoparticles were modified using phosphonic acid coupling agents. The applied coupling agents are listed in

Table 5.4. For practical synthetic reasons of the coupling agent molecule, instead of a glycydoxy-moiety phosphonic acid, a 3-epoxy coupling agent was used. Diol-TMS is not used as a free coupling agent as it is formed via post-hydrolysis of surface attached Gly-TMS.

The nanoparticle model system was dispersed in the molten monomer bisphenol-F-diclycidylether with filler contents of 3 wt%, 5 wt% and 10 wt%. During the curing procedure, several reactions of the nanoparticle surface with the reaction mixture, which influence the dispersion structure in the resulting nanocomposite, are possible: Hydroxygroups from the nanoparticles surface can react with epoxides of the resin mixture but also epoxide groups from the nanoparticle surface can be attacked by the hardener molecule to form covalent bonds between the nanoparticles and the matrix. In other cases, at least strong polar interaction between particle and resin (DEG) or hydrogen-bond formation (OH) can occur and influence the later dispersion structure.

Figure 5.11 present photographs of the different materials prepared with an identical thickness of 1.4 mm to visualize the transparency. Obviously, the materials containing unmodified nanoparticles appeared translucent whereas combinations of surface modifications and nanoparticle type appeared transparent like DEG-PPA@ZrO_2 or Gly-TMeOs@ZrO_2 in the epoxy resin.
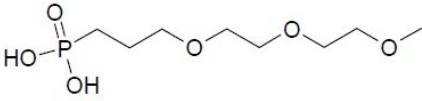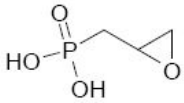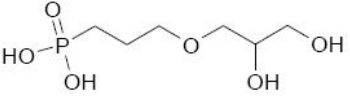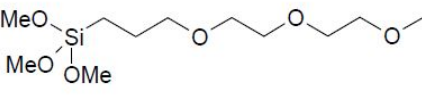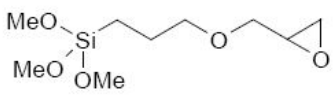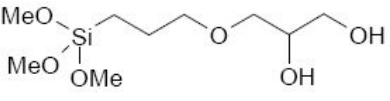
For a better insight into the dispersion behavior, representative TEM-images of ultramicrotome-thincuts (100 to 300 nm thickness) of the nanocomposite materials containing 5 wt% nanoparticles with different surface modifications are presented. Figure 5.12 shows TEM micrographs of ZrO_2/Epoxy resin nanocomposites and Figure 5.13 shows TEM images of larger SiO_2 particles/epoxy resin nanocomposites, each with epoxy-, diol- and diethyleneglycol-interface prepared as well as without surface modification. Due to a lack of contrast, TEM images of nanocomposites containing small SiO_2 are not shown.

In the case of ZrO_2 in epoxy resin, the DEG-surface modification results in the best dispersion quality (Figure 5.12b) compared to the large agglomeration of unmodified nanoparticles (Figure 5.12a). This corresponds to the observed optical transparencies in Figure 5.11b and d. Nanocomposites with diol-modified ZrO_2 nanoparticles show sub micron size particle agglomerates and finally the epoxy end groups causes strongly phase separated materials. In the case of SiO_2 nanocomposites, there are considerable differences of the observations compared to ZrO_2 nanocomposites as shown in Figure 5.13. The best results in homogeneity could be observed for the epoxide end group modification followed by the diol- modification (Figure 5.13c and d). A pronounced tendency to agglomerate was found for the DEG-TMS modification (Figure 5.13b) and even larger for the unmodified systems (Figure 5.13a).

The nanocomposites, filled with 3wt%, 5wt% and 10wt% of differently surface modified nanoparticles have been investigated by SAXS to support and complete the results from the TEM studies. It has to be mentioned that results from SAXS origin from a probe volume in the mm^3 range and are thus considered to be more

Table 5.4: List of the studied surface modifications.

capping agent formula	capping agent	abbreviation
	1-(3-diethylene glycol monomethyl ether) propoxy phosphonic acid	DEG-PPA
	oxiran-2-ylmethyl phosphonic acid	Ep-PPA
	3-(2,3,- dihydroxypropoxy) propyl phosphonic acid	Diol-PPA
	1-(3-diethylene glycol mono methylether) trimethoxysilane	DEG-TMS
	3-glycidoxy propyl trimethoxysilane	Gly-TMS
	-(2,3,- dihydroxypropoxy) propyl trimethoxysilane	Diol-TMS
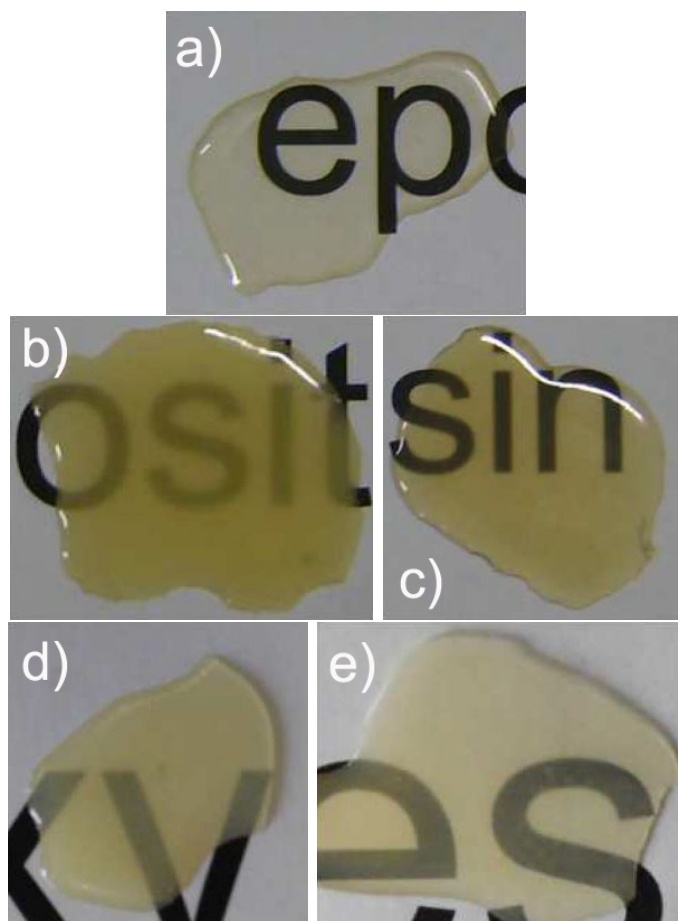
Figure 5.11: Photographs of a) blank epoxy resin and nanocomposite plates containing 5 wt% of b) unmodified and c) DEG-PPA@ZrO$_2$, d) unmodified and e) Gly-TMS@SiO$_2$ nanoparticles.
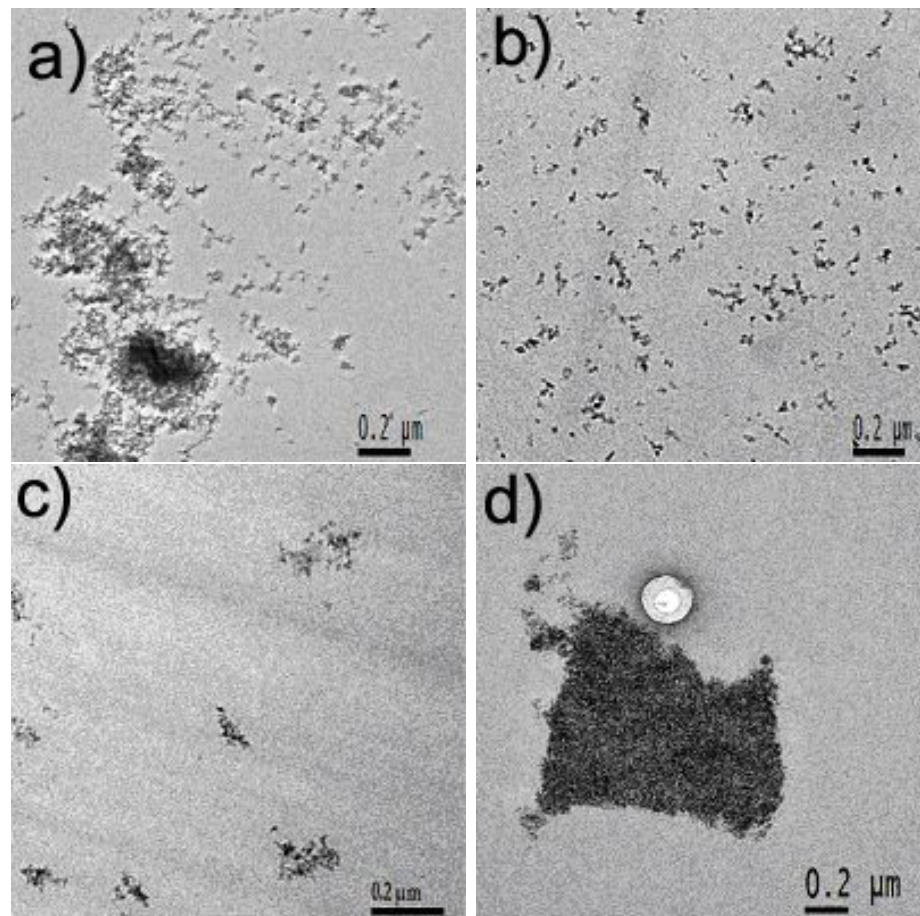
Figure 5.12: Representative TEM-images of ultramicrotome-cuts (100-300 nm thickness) of 5 wt% a) unmodified, b) DEG-PPA, c) Diol-PPA and d) Ep-PPA modified ZrO_2 nanoparticles embedded in epoxy resin.
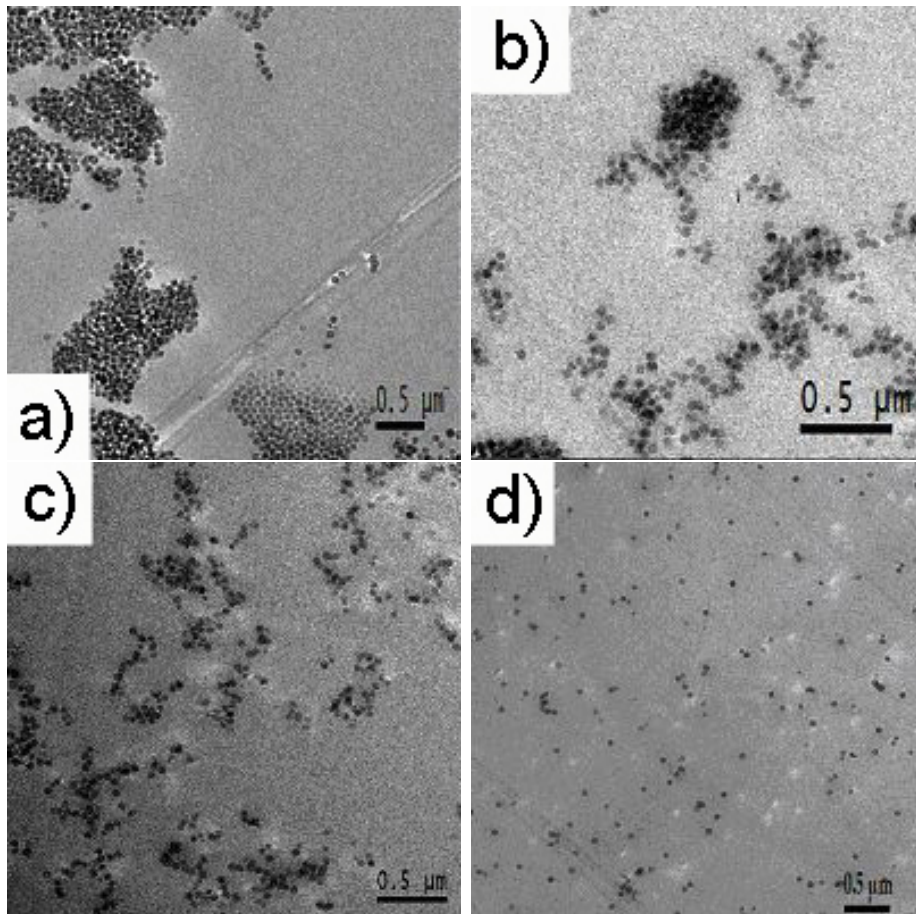
Figure 5.13: Representative TEM-images of ultramicrotome-cuts (100-300 nm thickness) of 5 wt% larger a) unmodified, b) DEG-TMS, c) Diol-TMS and d) Gly-TMS modified SiO$_2$ nanoparticles embedded in epoxy resin.

representative for the bulk material than TEM results with probe volumes in the nm^3-range. The scattering curves with the corresponding fit curves for 5 wt% filler content are shown in Figure 5.14.

From the scattering data, the hard sphere volume fraction η, which is an indicator for the strength of agglomeration of the particles in the matrix, has been calculated with Eq. 5.4 and Eq. 5.5. The results are listed in Table 5.5 and plotted in Figure 5.15 for better visualization. It is visible that the obtained results from SAXS correspond to the observations made in the TEM micrographs. Agglomerations observed in TEM are proven by large values for η obtained by SAXS. This fact is clearly visible for the ZrO$_2$/epoxy systems (Figure 5.15a). DEG-PPA modified particles give the best dispersion quality with η values close to zero which corresponds to single dispersed particles (especially at low filler content of 3 wt% and 5 wt%). Diol-PPA and Ep-PPA@ZrO$_2$, which were expected to enhance the dispersion due to the polymerizable end group, even show agglomerates in TEM, result in high values of η as indicator for high agglomeration tendency. The agglomeration trend for the small SiO$_2$ nanoparticles is complementary to the results from TEM (Figure 5.15b). Low η values were calculated for Gly-TMS and Diol-TMS while DEG-TMS results in high η values. Comparing the agglomeration trends for the small SiO$_2$ (Figure 5.15b) with the trends for the large SiO$_2$ nanoparticle system (Figure 5.15c), it can be concluded that the nanoparticle size also plays a crucial role in finding the optimum surface modification to yield maximum homogeneity. It should be noted that a different scale was chosen for Figure 5.15b and c. Large silica have in general a higher tendency to higher values for the hard-sphere volume fraction compared with the smaller silica nanoparticles, which could be caused by enthalpic reasons [89].

Table 5.5: Hard sphere volume fraction values η for different percentages of surface modified SiO$_2$ and ZrO$_2$ nanoparticles in epoxy resin matrix.

| particle type	filler vol%	hard sphere volume fraction η from SAXS			
		unmodified	DEG-PPA	Ep-PPA	Diol-PPA
small ZrO$_2$	3	0.045	0.001	0.097	0.073
	5	0.009	0.001	0.090	0.076
	10	0.008	0.020	0.090	0.049
	filler vol%	unmodified	DEG-TMS	Gly-TMS	Diol-TMS
small SiO$_2$	3	0.132	0.145	0.060	0.025
	5	0.131	0.143	0.028	0.032
	10	0.121	0.144	0.036	0.042
large SiO$_2$	3	0.174	0.160	0.148	0.099
	5	0.223	0.148	0.121	0.090
	10	0.156	0.188	0.079	0.110
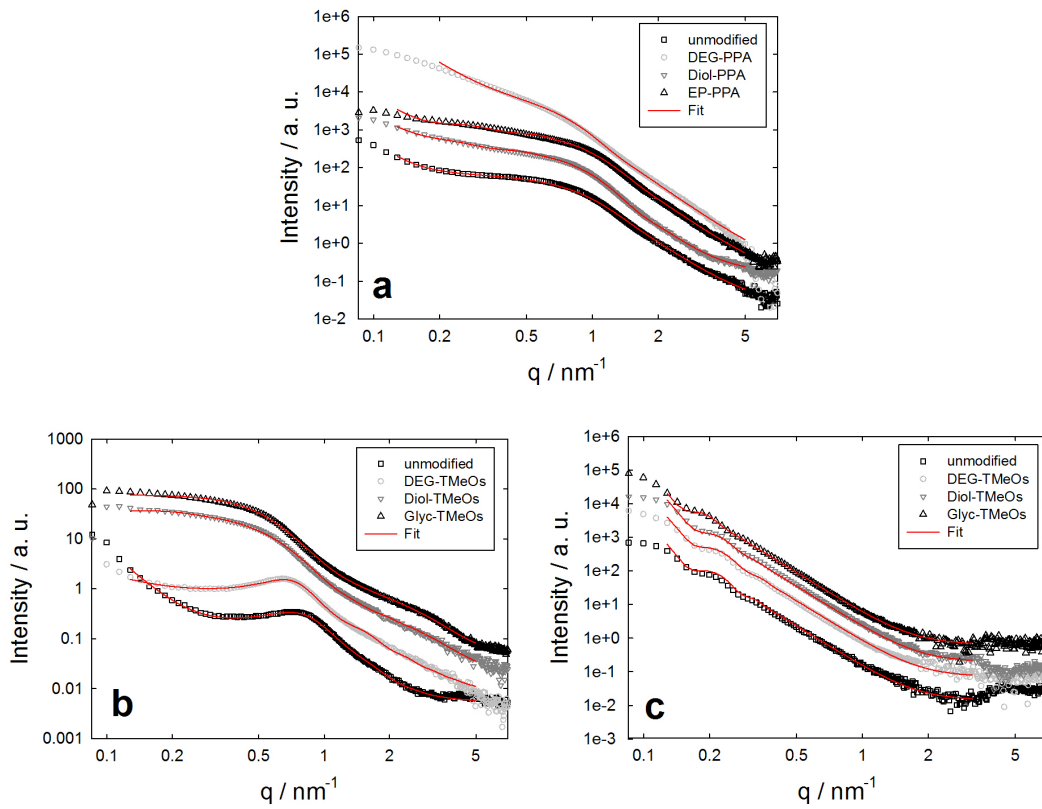
Figure 5.14: SAXS scattering curves, exemplarily shown for a 5 wt% inorganic nanofiller content of epoxy resin nanocomposites containing a) ZrO_2, b) small SiO_2 and c) large SiO_2.
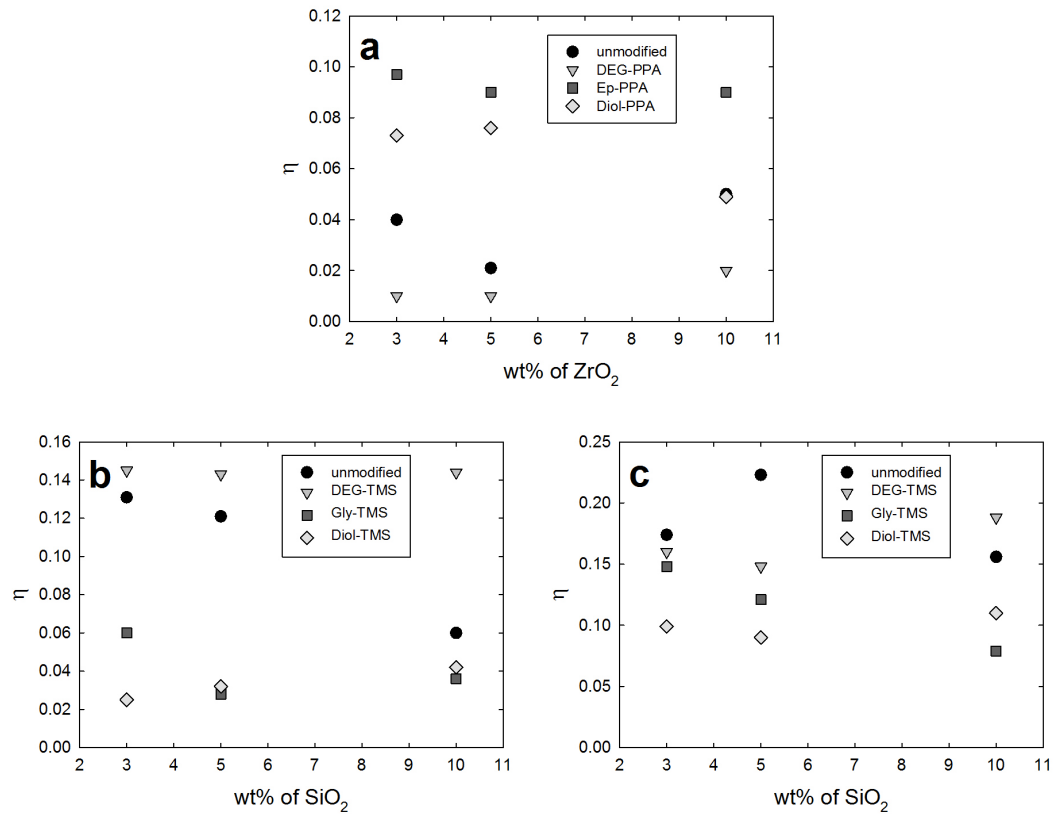
Figure 5.15: Hard sphere volume fraction η of a) ZrO_2 as well as b) small and c) large SiO_2 nanoparticles with different surface modifications and incorporated into the epoxy resin matrix with different weight percentages.

5.3.5 Discussion

The effect of the surface-functionalization on the dispersion of the nanoparticles is directly visible in the TEM studies and proven by SAXS. The question has to be answered, why varying coupling agents causes different behavior of the nanoparticles to agglomerate or disperse. SEM-investigations done by Kang et al. support the necessity of chemical surface tailoring of nanoparticles: Unmodified Stoeber particles incorporated in epoxy resin showed huge agglomeration compared to epoxide or amine modified nanoparticles [166], which react immediately with the surrounding polymer environment and therefore result in separated particles.

Ep-PPA@ZrO_2 was expected to result in high dispersion due to the polymerizable end group as it was the case for SiO_2PS and SiO_2/PMMA systems in chapter 5.1, however, high agglomeration was observed by TEM (Figure 5.12c) and SAXS (Figure 5.15a). One reason can be the presence of a strong interparticle interaction via co-linkage of surface epoxy group. Even though the modification chemically fits to

the epoxy resin matrix, particle-particle interaction can not be avoided. In the case of SiO_2 nanoparticles, the opposite behavior was observed for epoxide modification. This fact can be explained by the different nanoparticle shapes of the two systems. The crystal facet shape of the ZrO_2 nanoparticles can lead to a strong interaction between two facets. One can assume that the possibility of irreversible interparticle co-condensation is higher than for spherical SiO_2 particles, especially for smaller silica. A very homogeneous dispersion is observed for SiO_2 nanoparticles as expected from the compatibility of epoxide groups with the epoxy resin matrix. This result is in good agreement with the conclusion in chapter 5.1 concerning the positive effect of polymerizable end groups on high dispersion. The influence of nanoparticle size on the dispersion is visible at the example of Diol-TMS, as this surface-modifcation results in a well dispersed SiO_2/epoxy system for small particles whereas larger particles lead to slight inhomogeneity as shown in Figure 5.13d. This effect can be related to particle curvature effects as observed for ZrO_2.

In general, the hard-sphere volume fraction tend to be higher for silica, especially in the case of larger silica, than for zirconia nanoparticles when looking at the different scales in Figure 5.15a-c. One reason can be a higher tendency of silica to agglomerate than zirconia. The agglomeration of SiO_2 nanoparticles can be supported by their spherical shape which eases dense sphere packing. This effect for uniform spherical silica particles could be observed in past studies, even if organic modifications were used [174]. Nanoparticles try to minimize their surface energy via agglomeration. This effect seems to be higher in the case of SiO_2 and enthalpy can thereby play an important role, which is commonly a crucial parameter for the dispersion of nanoparticles in polymers [89]. It can be explained as well why the η values for small SiO_2 nanoparticles are generally lower compared to the larger SiO_2 nanoparticles. One can summerize that SiO_2 nanoparticles can be more densely packed than the irregular shaped ZrO_2 nanocrystals and thus, if agglomeration can be observed, the η values are higher for the SiO_2 system.

The surface-modifcation with DEG-PPA and DEG-TMS, which are expected to interact physically with epoxy resin, results in opposite behavior of the respective nanoparticle system. Homogeneously dispersion of the ZrO_2 nanoparticles in the epoxy resin could be observed (Figures 5.12b and 5.15a) while highly agglomerated SiO_2 nanoparticles were visible in the epoxy resin nanocomposite (Figures 5.13b and 5.15b, c). A possible reason could be that the dispersibility enhancement effect could not overcompensate a possible interparticle-co-condensation via residual surface silanol groups in case of the silica.

This allows the assumption that the SiO_2 system can be explained by the following rule:

- The stronger the possible particle-matrix interaction, excluding silanol condensation reactions, the more homogeneous the final material (covalent > H-bridges > polar-polar).

In the case of ZrO_2 nanocrystals the opposite behavior was observed, which could

be explained by the rule:

- The particle-particle interaction is predominant to the particle-matrix interaction applying strong interacting groups.

Furthermore, a variation of the agglomeration behavior for one type of modification with increasing filler degree was visible for all nanoparticle/polymer systems (Figure 5.15). This can be related to the interplay of two different counteractive phenomena. On the one hand, higher filler degree increases the viscosity, which leads to an increase of the shear force at the same stirring speed and thus breaks agglomerates. On the other hand, the possibility of two interacting particles increases in thick suspensions and thereby enhances the formation of agglomerates. This effect can occur if the particle-particle interaction dominates the particle matrix interaction. A study in literature on the shear thickening effect of silica nanoparticles in PEO points out the complex viscosity changing behavior with suspension concentration. It has been observed that the viscosity drastically increases for higher filler degrees above 7 %, depending on the nanoparticle size and polymer radius of gyration [157]. Therefore, possible dispersion minima or maxima in the agglomeration curves could be observed, depending on which of these two effects is predominant and how strong the matrix-particle interaction is compared to the particle-particle-interaction. A higher particle-particle interaction, and thus stronger agglomeration, is favored for plane structures or, in the case of large nanoparticles, for less curvature of the particles. The correlation between agglomeration, size and viscosity shear force effect can be investigated for the example of large Gly-TMS@SiO$_2$. The strong interacting Gly-TMS may lead to higher agglomeration at low filler degrees. The hard-sphere volume fraction η decreases for this system with increasing filler content, which can be caused by the viscosity shear force effect as this effect should be stronger for larger particles. Kamibayashi et al. found out that different sizes of particles result in different viscosities of the suspensions, changing the agglomeration behavior [157]. The obtained data are considered to be the result of a complex interplay of the various described phenomena.

5.3.6 Conclusion

The agglomeration behavior of SiO$_2$ nanoparticles in two different size ranges, in a lower (6-10 nm) and upper (60-70 nm) range, and ZrO$_2$ nanoparticles with a 22 nm spherical equivalent diameter was studied in epoxy resin matrices using different surface modifications. Unmodified nanoparticles as well as particles with varying coupling agents such as diethyleneglycol- 1,2-diol group- and epoxide group have been prepared to study the effect of different interaction strength between particle surface and surrounding matrix in the epoxy resin curing process. From TEM and SAXS data one can conclude that the dispersion quality is given by the interplay of several effects in these complex systems. On one hand surface groups like epoxides

allow a covalent interaction with the matrix, which should lead to a better dispersion of the particles. On the other hand also homo-linkage between the particles resulting in agglomeration can occur. This allows the assumption that the effect of a higher interacting matrix particle system compared to interactions within a particle-particle system is important when tuning the nanoparticle surface to reach maximum homogeneity. This effect can be seen in analogy to the copolymerization parameters in macromolecular chemistry, whereas in this case, polymerizable groups are present on the nanoparticle surface representing nanoparticles as one type of monomer. However, one should not underestimate the influence of the nanoparticle nature and shape. In the case of ZrO_2, the overall interparticle interaction can become very high between two crystal facets due to the high contact area compared to the interaction between two spheres as in the case of SiO_2. Therefore, low interacting modifications such as DEG for ZrO_2 give an optimum on homogeneity in the material as the particle-matrix interaction is predominant. Stronger interacting moieties lead to higher agglomeration due to a dominating particle-particle interaction, as it has been demonstrated for epoxide end groups. Furthermore, suspension concentration effects can lower the agglomeration if the viscosity increases and thus the shear forces. On the other hand the probability of two particles agglomerating can be raised. These effects are expected to depend strongly on the nanoparticle nature, especially on their size. The dispersion of the nanoparticles within the epoxy resin has been measured and thus been discussed in this chapter by comparing the different modified nanoparticle composite systems.

Considering these effects, the dispersibility of oxide nanoparticles could be tuned applying organosilanes and organophosphonic acids to produce homogeneous nanocomposites via low shear force and thus lower energy effort. However the optimum surface modification has to be found and modified for each system. Therefore, SAXS and TEM studies support the development and investigation of well defined and novel nanocomposite systems.

5.4 The effect of concentration, size and surface chemistry of zirconia and silica nanoparticle on the bulk properties of epoxy resin nanocomposites

Compared to the previous chapter 5.3, where different surface-functionalizations and their effect on the structural properties of the epoxy resin nanocomposite were investigated, now the focus was not only on structural, but also on thermomechanical and mechanical properties of these nanocomposites containing DEG@SiO_2 and DEG@ZrO_2 nanoparticles as inorganic building blocks.

Epoxy resin nanocomposites were prepared by curing bisphenol-F with an aliphatic

amine containing oxide nanoparticles as inorganic nanofillers. Both types of nanoparticle, amorphous, spherical SiO_2 and crystalline, non spherical ZrO_2, were prepared in two different size ranges, one around 5 nm and the other around 50 nm, to investigate the influence of size on the dispersion in the nanocomposites. The two nanoparticle systems were surface-functionalized with novel diethylene glycol based capping agents to increase the compatibility with the epoxy matrix. Anchor groups, phosphonic acid for zirconia and trialkoxysilane for silica, were used to attach the organic functions to the nanoparticle surface. To determine the homogeneity of the distribution of surface-modified inorganic nanofillers in the organic matrix up to 5.8 vol% in case of silica and 2.34 vol% in case of zirconia, the nanocomposites were investigated by small-angle X-ray scattering and transmission electron microscopy. Hardness tests and differential scanning calorimetry helped to define the influence of the increasing nanofiller content on mechanical properties or thermomechanical properties.

This chapter is based on the publication of Sajjad et. al. [S3].

5.4.1 Introduction

Due to the promising outlook of generating new properties of polymeric materials, the development of inorganic-organic polymer nanocomposites by merging organic polymers and inorganic fillers in one material expanded fast in this research field [175]. One method, which has been extensively used to tailor the properties of organic-inorganic composites, is the sol-gel process [176].

Several studies prove the enhanced overall stability and mechanical properties of polymers by incorporation of metal and metal oxide nanoparticles [162, 177, 178]. One aim is the homogeneous dispersion of the nanofillers in the polymer matrix, which thus contributes to theses considerably improved mechanical and thermal properties of the inorganic-organic nanocomposites. This is achieved using an appropriately modified interface [179]. Inorganic moieties can be effectively incorporated in the organic matrix via covalent linkage [134], which is achieved by the modification of the particle surface applying coupling agents. Thereby, interaction is forced up and thus dispersibility of the nanofillers within the matrix is promoted. Additionally, the incorporation of polymerizable end groups in the coupling agents offers increased interfacial adhesion through copolymerization [180]. These two effects are advantageous for the improvement of mechanical properties.

Conventional molecules for surface modifications of metal oxides are polymeric surfactants like poly(ethylene oxides) (PEO), [181] poly(vinyl pyrrolidones) (PVP), [182] ionic surfactants like organic sulfates of sulfonates or capping agents consisting of an anchor group like alkoxysilanes [180, 183] and chlorosilanes, organophosphorous acids or carboxylic acids [12, 15, 97, 174, 184].

In literature, epoxy resin inorganic-organic nanocomposites usually contain un-

modified silica particles or clays as fillers [168, 185]. Partially these particles were also surface-modified with aliphatic amines, alkyl-chain-bearing surfactants, and silane capping agents containing alkyl-spacer and epoxy end groups, or PEO-based modifying agents in which the polymer chain interacts with the inorganic surface by weak chemical interactions [167, 186]. SiO_2-Stöber-particles were chosen as model systems because of the excellent control of size and size distribution during synthesis. Due to these properties Stöber-particles are ideal candidates for nanocomposite preparation and the systematic studies for structure-property relationship [187, 188]. Zirconia nanoparticles were choosen to investigate the enhancement of hardness and other mechanical properties and thermal stability of classical thermoplastics, especially for coating applications [189, 190]. Only a few literature reports can be found about the preparation and characterization of epoxy-zirconia nanocomposites. A recent study by Medina et. al. shows a significant increase in the mechanical properties of epoxy with the addition of zirconia [162].

In this chapter, the synthesis and characterization of nanocomposite materials with two types of nanoparticles incorporated into an epoxy matrix is presented in detail. Capping agents built up by a diethylene glycol group were attached to the nanoparticle surface by covalent bonds and therefore contributed to a good interaction between particle and matrix. The main goal of this chapter was the systematic investigations of structure-property relationships in epoxy resin nanocomposites depending on the composition, size and morphology of the nano building blocks.

5.4.2 Experimental

Bisphenol-F-diglycidyl ether (BFDGE) was purchased from Organica Feinchemie GmbH. Diethylenetriamine was distilled before AQ3 use, water was deionized, and methanol was purified using a PureSolv (Innovative Technology Inc.) solvent purification system. All other chemicals and solvents (HPLC grade) were purchased from Sigma Aldrich and ABCR and were used without further purification.

Nanoparticles syntheses

The detailed experimental procedures are included in the thesis of Feichtenschlager [120] and the publication of Sajjad et. al. [S3]. Silica nanoparticles were prepared in two different sizes according to literature known procedures applying and tailoring the Stöber process resulting in small [67, 191] and large nanoparticle [68] containing colloidal sols. The smaller silica nanoparticles exhibited DLS diameters of 9±2 nm and the larger particles of 72±10 nm. Small and large zirconia nanoparticle powders were prepared applying hydrothermal conditions according to literature known procedures [69, 70]. The smaller zirconia nanoparticles exhibited a spherical equivalent diameter of 22±4 nm and the larger particles of 66±1 nm as measured by DLS.

The synthesis of the capping agents - DEGPPA and DEGTMS - and the procedures of the surface functionalization of the nanoparticles are also described in detail in the work of Sajjad et. al. [S3] and the thesis of Feichtenschlager [120]. Silica nanoparticles were modified using a quasi $in-situ$ modification approach starting from the as prepared silica particle sol. Zirconia nanoparticles were modified using a post-modification approach in accordance to a procedure described in literature for titanium dioxide nanoparticles [15].

Preparation of epoxy resin nanocomposites

Amine cured bisphenol-F-based epoxy resin was prepared by a standard procedure described in literature [172]. Bisphenol-F-diglycidylether (BFDGE) (2.0 g, 7.03 mmol) was molten at 70 °C and the particle powder was added, followed by magnetic stirring at 750 rpm in a flat bottom 15 mL glass vessel for 2 h. Diethylenetriamine (DETA) (0.2 g, 1.94 mmol) was afterwards added to the reaction mixture, which was immediately cast on a silicone grease coated stainless steel plate and cured at 120 °C for 16 h to give sample plates of 1.2-1.5 mm thickness and 3-5 cm diameter.

The stoichiometrical ratio of epoxide groups to amine group was selected to be 2.6 to obtain thermoset materials, via the variation of the molar ratio of BFDGE / DETA.

Nanocomposite materials consisting of 1.7 vol%, 2.9 vol%, 5.8 vol% (corresponding to 3 wt%, 5 wt% and 10 wt%) of small and large silica and 0.67 vol%, 1.12 vol%, 2.34 vol% (corresponding to 3 wt%, 5 wt% and 10 wt%) of small and large zirconia were prepared.

Characterization

Ultra microtome-thin-cuts with a thickness of about 100 nm were performed on "Ultra cut E" (Leica) instrument at room temperature. Transmission electron microscopy (TEM) images were recorded on a JEOL JEM-100CX and on a FEI TECH-NAI G20 transmission electron microscope.

Small angle X-ray-scattering (SAXS) measurements were performed under vacuum in transmission geometry using a rotating anode X-ray generator with a pinhole camera (Nanostar, Bruker-AXS) with Cu K_α radiation monochromatized and collimated from crossed Goebel mirrors and a 2D position sensitive detector (Vantec 2000). Measurements were carried out at two different distances (13 cm and 108 cm) to cover a wide q range. All SAXS patterns were radially averaged and corrected from background scattering to obtain the scattering intensities in dependence on the scattering vector $q = 4\pi/\lambda\sin\theta$, where 2θ is the scattering angle and $\lambda =0.1542$ nm the X-ray wavelength.

Temperature modulated DSC thermograms were recorded with a TA Instrument DSC - Q2000 in a nitrogen gas flow of 50 mL min^{-1} with a heating rate of 3 K min^{-1}, an amplitude of ±0.5 K and a period of 60 s for all materials. The T_g of the

filled epoxy was characterized as the midpoint of the change in specific heat from DSC scans.

Vickers hardness measurements were done with a load of 0.98 N. At maximum load a dwell time of 30 s was chosen.

5.4.3 Results and Discussion

Structural investigation of nanoparticles and their surface functionalization

The prepared silica particles were amorphous while the zirconia powders consisted of about 100 % crystalline monoclinic ZrO_2. Both particle types have been synthesized in the lower (about 5 nm) and upper (about 50 nm) nano range to investigate size effect of nanofillers in nanocomposite formation. TEM images shown in Figure 5.16 display crystal-facet-shaped small zirconia nanocrystals (Figure 5.16a) and the polycrystalline large zirconia nanoparticles (Figure 5.16b), both with aspect ratio of about two. The prepared silica particles as presented in the Figures 5.16c and d had a spherical shape. Size analysis was carried out manually if the contrast was not sufficient enough for an automatic evaluation. In case of the irregularly shaped zirconia, the equivalent circle diameter is given in Table 5.6 for a better comparison with spherical silica particles. The size distribution of all synthesized nanoparticles is rather uniform, which was also confirmed by DLS measurements.

SAXS was additionally used to determine the particle size. The SAXS intensities and fit curves are shown in Figure 5.17. The fit curves describe spheres with a Gaussian size distribution [36]. As in the SAXS curves peaks are visible, which are due to agglomeration, a structure factor has to be introduced. In the hard-sphere model, the Percus-Yevick approximation [42] allows the quantification of the agglomeration behavior with a mean distance of the spheres D_{HS} and the amount of filled volume, the hard-sphere volume fraction η [43, 77]. The larger the tendency to agglomerate, the higher the value of η. The hard-sphere model in SAXS was used not only for spherical silica, but also for platelet-shaped zirconia nanoparticles: The diameters obtained from SAXS (from the hard-sphere model) and TEM (equivalent circle diameter) are in perfect coincidence [S1]. However, one has to admit that the use of the hard sphere model for platelet-shaped particles is only a first approximation, and the intensities do not generally factorize into a product of structure factor and form factor for polydisperse objects with an ellipsoidal shape [192]. The fit parameters for SAXS (size and distribution width of spherical particles as well as distance and hard sphere volume factor) are summarized in Table 5.6 together with the size obtained by DLS and TEM.

It should be noted that the wiggles in the SAXS intensities of the large silica particles towards very low q-values are due to the form factor of spheres and only observed in the case of extremely narrow size distributions. This directly confirms the quality of the Stöber process. For large zirconia particles, two peaks are observed and were fitted with two Gaussian size distributions. The reason is that the large
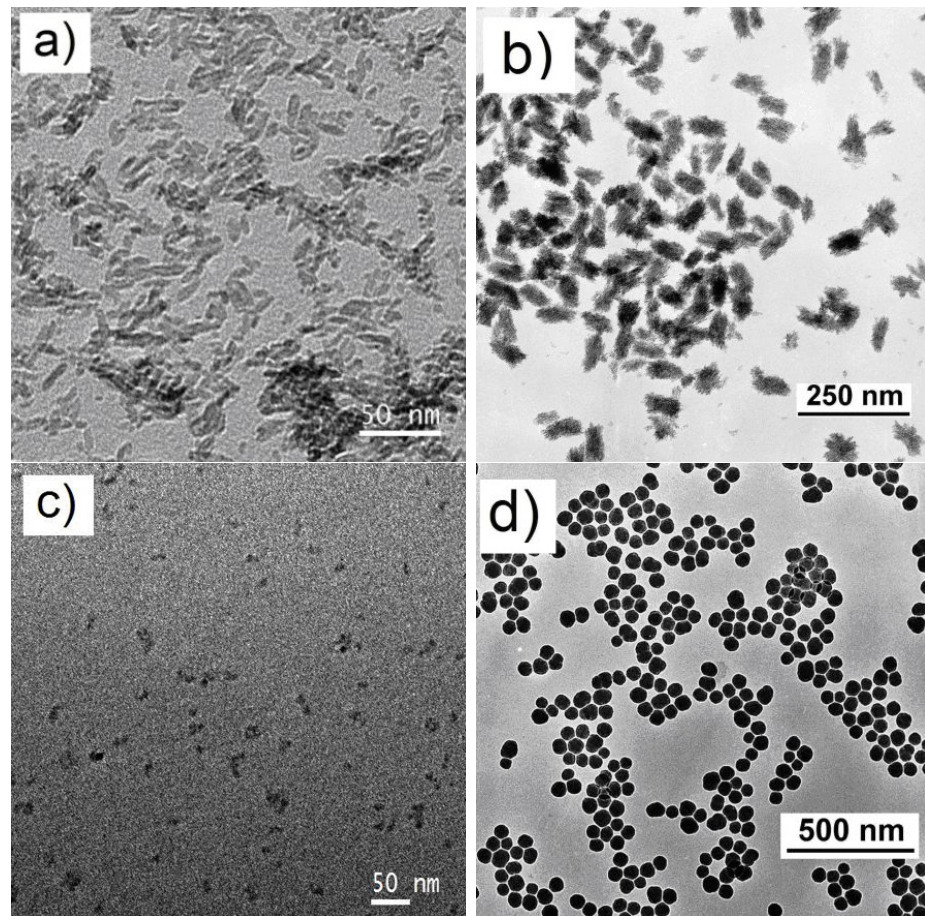
Figure 5.16: TEM micrographs of small (a) and large (b) ZrO_2, and small (c) and large (d) SiO_2 nanoparticles.

zirconia particles are built up of smaller subunits, which is also visible in the TEM image Figure 5.16b.
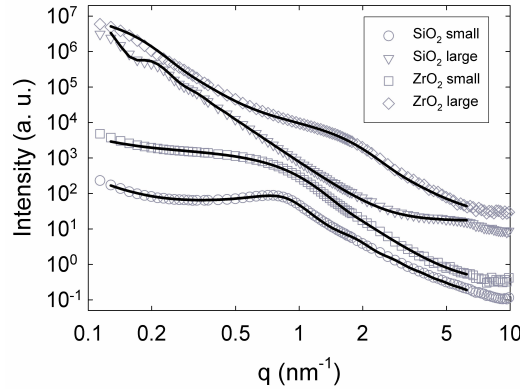

Figure 5.17: Experimental SAXS profiles $I(q)$ (symbols) and fitting curves (solid lines) using the numerical approach with spheres with a Gaussian size distribution and a hard-sphere model for the structure factor. The profiles are shifted vertically for better visibility.

Table 5.6: Fitting parameters of SAXS profiles and particle size from DLS (from mass weighted size distribution, error from peak width) and TEM (error from standard deviation) for neat SiO_2 and ZrO_2.

particle type	particle diameter d_{SAXS} [nm]	Gaussian distribution width	hard-sphere volume fraction η	sphere to sphere distance D_{HS} [nm]	particle diameter d_{TEM} [nm]	particle diameter d_{DLS} [nm]
SiO_2 small	5.4	±0.85	0.13	6.5	5±1	9±2
SiO_2 large	58.0	±3.80	0.13	69.0	61±7	72±19
ZrO_2 small	6.0	±0.65	0.02	6.7	6±1	22±8
ZrO_2 large	34.0	±3.70	0.05	41.0	38±12	66±19

The distance of hard spheres is slightly larger than their size, which is attributed to some intermediate material and the asymmetry of particles. Silica nanoparticles exhibit a higher tendency to agglomerate than zirconia nanoparticles, which is visible by the higher hard sphere volume fraction observed for the nanocomposites in this case (Figure 5.21). This is possibly due to enthalpic reasons, which is commonly seen as a crucial parameter for the dispersion of nanoparticles in polymer [89]. The surface energy of silica nanoparticles in solution is probably relatively high in comparison to zirconia, supported by their spherical shape, whereas large zirconia particles are more porous clusters built up from smaller units (Figure 5.16). The

agglomeration of silica nanoparticles should therefore reduce the surface and thus leads to a gain in enthalpy, which is much less pronounced in the case of zirconia.

For the incorporation of the inorganic metal oxide particles (polar) into the bisphenol-F-based epoxy resin matrix, the particles have been surface modified with phosphonic acid (anchor group for ZrO_2) and trimethoxysilane (anchor group for SiO_2) capping agents. The two capping agents used are listed in Table 5.7. Silane capping agents of the type R-SiX3 (X = -halogen, -alkoxy) covalently bind to the silica surface [10, 12] while phosphonic acids covalently bind to zirconia surfaces analogously as to titania [193].

Structural investigation of the nanocomposites by SAXS

The prepared epoxy-resin nanocomposite samples, having a thickness of 1.2-1.5 mm, appeared all macroscopically homogeneous, translucent in the case of all used silica particles and transparent in the case of surface-modified zirconia nanoparticles (Figure 5.18). Surface modification seems to result in a more transparent material, whereas neat unmodified particles lead to more turbid nanocomposites.

The sample turbidity can be attributed to different agglomeration behavior of the inorganic particles in the organic matrix and was verified by TEM on different ultra microtome thin cuts of the nanocomposite samples (Figure 5.19). Zirconia particles (Figure 5.19a and c) are obviously better dispersed than silica nanoparticles (Figure 5.19b and d). Surface modified ZrO_2 nanoparticles (Figure 5.19c) show no agglomeration, whereas the effect of the surface modification on SiO_2 nanoparticles is much less pronounced and large agglomerates are still visible (Figure 5.19d). The TEM images of nanocomposites containing small SiO_2 nanoparticles are not shown due to the poor quality caused by the small size of the nanoparticles and the low contrast between epoxy resin and amorphous SiO_2.
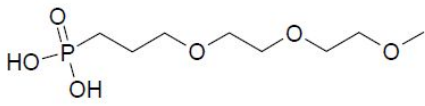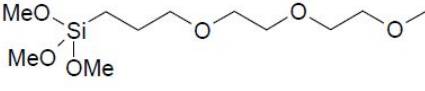
Even a higher percentage of surface-functionalized zirconia nanoparticles (2.34 vol%) resulted in homogeneous and transparent materials and is thus considered as the most promising system in this work for technical applications such as transparent coatings due to its good adhesive properties.

The scattering intensities with the corresponding fit curves for the nanocomposites with different vol% filler content are shown in Figure 5.20. The data support the fact that zirconia nanoparticles are nearly not agglomerated and exhibit a much better dispersion than silica nanoparticles. The agglomeration behavior, described by the hard sphere volume fraction and calculated from the SAXS scattering profiles for both particle types is shown in Figure 5.21 and numerical values are listed in Table 5.8). Neither the surface-functionalization of SiO_2 particles nor the amount of nanoparticles affect the agglomeration significantly. However, the size of the particles shows a clear influence as high values for η were obtained for large nanoparticles. This is a clear sign for the higher possibility of a larger particle to interact with a neighbour particle than with the polymer chains.

Table 5.7: Organophosphorus coupling agents used for the surface modification of ZrO$_2$.

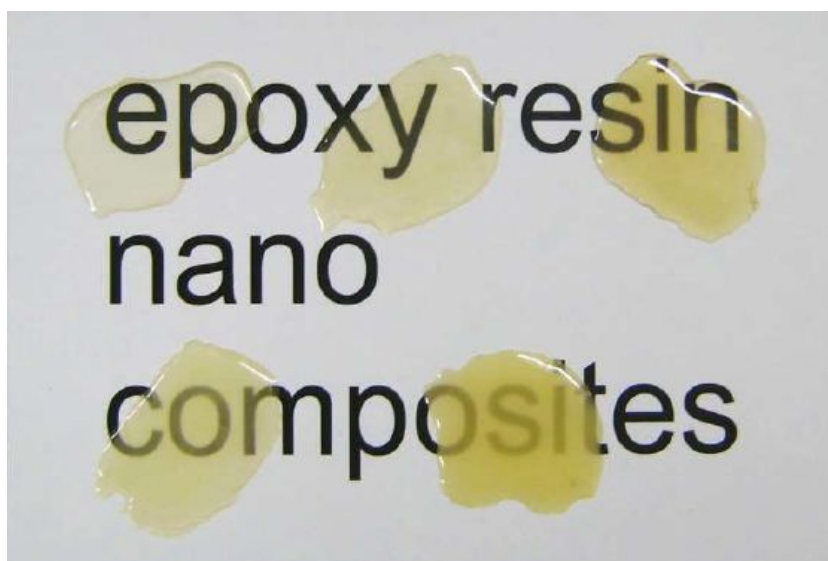| capping agent formula	capping agent	abbreviation
	diethylene glycol monomethyl ether phosphonic acid	DEGPPA
	diethylene glycol monomethyl ether trimethoxysilane	TMSPPA

Figure 5.18: Zirconia-epoxy-resin nanocomposite samples (1.2-1.5 mm thickness): upper row from left to right: neat matrix, 0.67 vol% DEGPPA@ZrO$_2$ small, 1.12 vol% DEGPPA@ZrO$_2$ small; lower row from left to right: 0.67 vol% neat ZrO$_2$ small, 1.12 vol% neat ZrO$_2$ small.
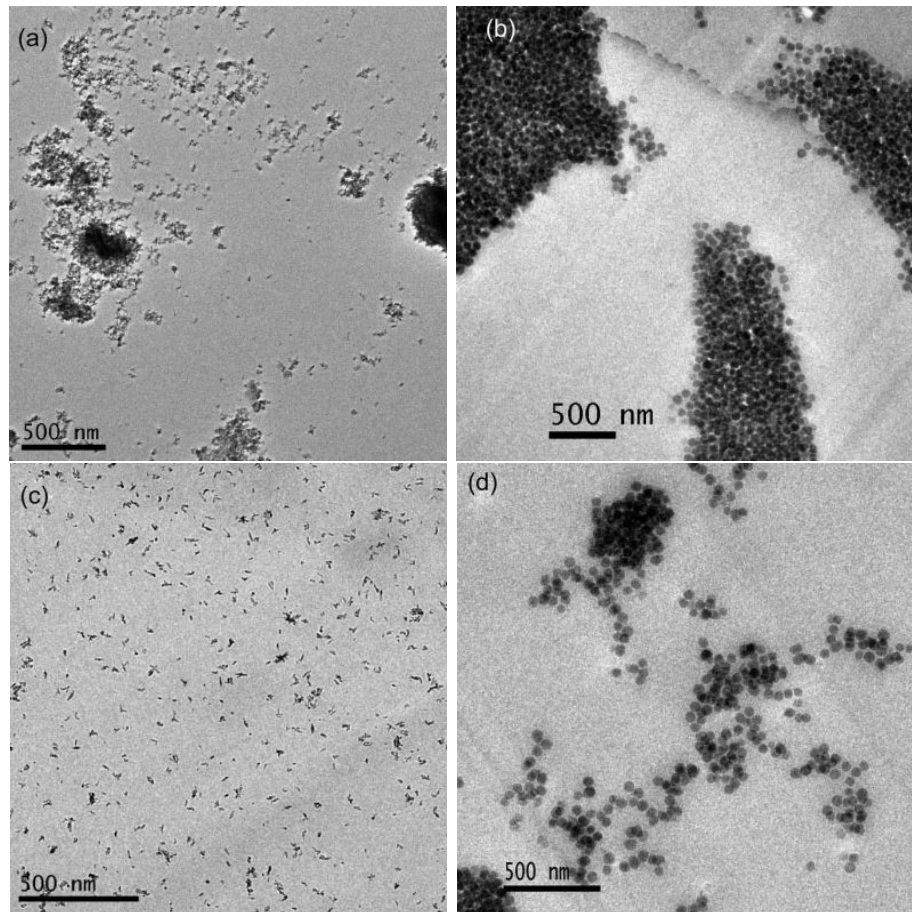
Figure 5.19: Representative TEM micrographs of ultramicrotome cuts of epoxy resin nanocomposites containing 3 wt% inorganic fractions: (a) unmodified ZrO_2 small; (b) unmodified SiO_2 large; (c) DEGPPA@ZrO_2 small; (d) DEGTMS@SiO_2 large.
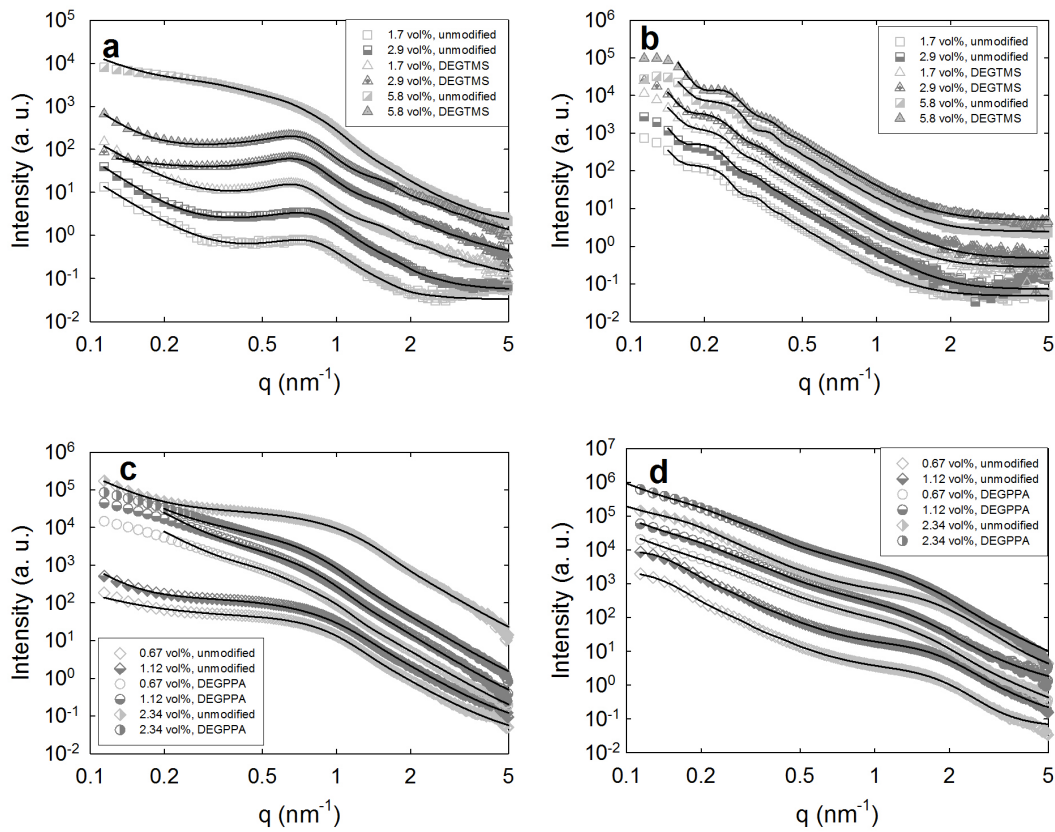
Figure 5.20: Experimental SAXS intensities (symbols) and fit curves (solid lines) are shown for different vol% inorganic nanofiller content of epoxy resin nanocomposites containing (a) small SiO_2; (b) large SiO_2; (c) small ZrO_2; (d) large ZrO_2. The profiles are shifted vertically for better visibility.
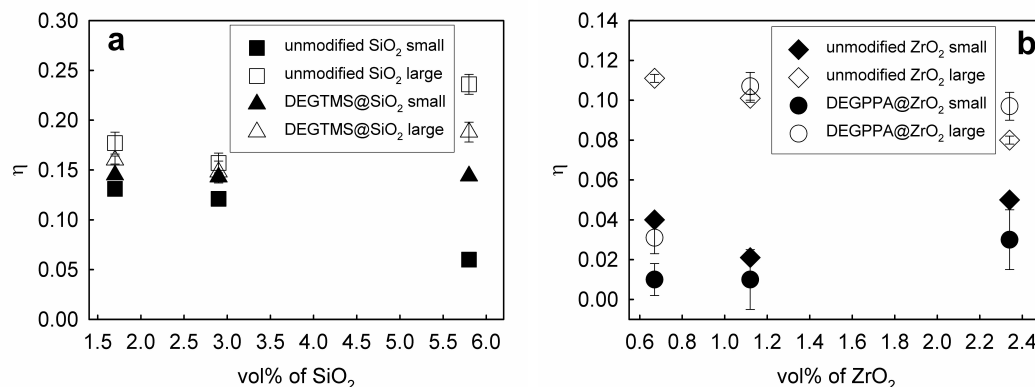
Figure 5.21: Hard-sphere volume fraction η for unmodified and modified SiO_2 particles (a) and ZrO_2 particles (b) for different amounts of particles embedded in epoxy resin. Note that the scale of the ordinate is different in (a) and (b). The error is the fit error at a confidence interval of 0.95 and does not include uncertainties from the choice of the hard-sphere model.

Table 5.8: Hard sphere volume fraction values η for different percentages of unmodified and surface modified SiO_2 and ZrO_2 nanoparticles in epoxy resin matrix

particle type	filler vol%	η of unmodified	η of DEGPPA
small ZrO_2	0.67	0.040	0.010
	1.12	0.021	0.010
	2.34	0.050	0.030
large ZrO_2	0.67	0.111	0.031
	1.12	0.101	0.107
	2.34	0.080	0.097
	filler vol%	η of unmodified	η of DEGPPA
small SiO_2	1.7	0.132	0.145
	2.9	0.131	0.143
	5.8	0.060	0.144
large SiO_2	1.7	0.174	0.160
	2.9	0.223	0.148
	5.8	0.236	0.188

Differently, there is a considerable influence of the surface-functionalization on the hard sphere volume fraction for ZrO_2 particles: In particular for small ZrO_2 doped nanocomposites capped with DEGPPA no agglomeration is observed, and also for large particles, the tendency to agglomerate is strongly reduced for the lower amount

of particles within the matrix. Only for the high amount of zirconia particles, no difference between unmodified and modified particles was found.

The two types of nanoparticles, SiO_2 and ZrO_2, obviously show different agglomeration behavior inside the polymer matrix, even for similar volume percentage. Zirconia particles show less agglomeration in general, and small zirconia particles with surface-functionalization are perfectly randomly distributed in the matrix. Due to the better distribution within the matrix, we restricted ourselves to investigate the thermal and mechanical properties only of epoxy-resin nanocomposites containing modified SiO_2 and ZrO_2 particles.

Thermo-mechanical and mechanical behavior of modified nanocomposites

The effects of the filler size and filler content on the glass transition temperature T_g of the polymer composites were studied by DSC and are shown in Figure 5.22. A decrease of T_g was observed with increased filler content. There is only a slight decrease for small particles, but a considerable higher decrease for large ones. The T_g of the nanocomposites with zirconia particles is less affected by increasing filler content in comparison to the silica/composite system. Considering the same volume fraction of the two nanofillers, it is obvious that the decrease in T_g is less in case of the zirconia/epoxy system as compared to the decrease in case of the silica system. The change in T_g for nanofiller composites is often and, in addition, quite controversially discussed in literature. Several authors have reported an increase of T_g as a function of the filler loading [194, 195] whereas others have observed the opposite [196, 197]. Some authors have suggested that phase separation is responsible for the decrease which is due to the lack of adhesion between the filler and the epoxy groups. Other authors have related this decrease to the increase in free volume as unrestrained epoxy molecular chains move easily upon heating. Becker et al. attributed the reduction of T_g to a possible lower crosslink density around clay particles, maybe due to the perturbing effects of the clay, even if the presence of the clay encourages higher conversion of epoxy [198]. Thus, the clay may change the chemistry of the reaction. A negative effect on T_g was observed for epoxy resin filled with carbon black nanoparticles, which is attributed to increasing chain mobility due to the dramatically increasing interfacial area between fillers and polymer matrix [195]. In the study of Huang et al, the decrease of T_g is related to the reduced crosslinking density in the vicinity around the silica nanoparticle [199]. One possible reason can be entropic reasons: Whereas small nanoparticles can easily be incorporated into the polymer, larger nanoparticles lead to a polymer chain expansion and a loss of entropy, which is called "stretching free energy cost" [89]. This is seen as the main reason for the nondispersibility of larger nanoparticles [89]. The entropic contribution of the polymer has been extensively discussed in literature [200]. On the one hand the higher penalty in the entropic contribution should lead to a higher agglomeration of larger nanoparticles (a higher hard sphere volume factor, Figure 5.21). On the other hand it should change the flow characteristics in the

surrounding of these large nanoparticles so that the chain mobility is increased and the glass transition shifts towards lower temperatures.

Another explanation can be the influence of nanoparticles on the curing behavior of the composite. Whereas the small particles do nearly not hinder the development of the network to a large extent, larger nanoparticles are stronger obstacles. Therefore, an important parameter is the ratio of particle diameter to the radius of gyration R_g of the uncured resin. Assuming a R_g value of about 10 nm, it can be expected that in the uncured network the statistical arrangement of the molecules is much more disturbed in the case of larger nanoparticles, having a size of about five times higher [201]. Furthermore, if one considers the higher tendency of SiO_2 to agglomerate even in the surface modified state (Figure 5.19d), regions with very low interparticle distances inside the agglomerates can exist. It was proposed by Chen et al. for layered silica that an interphase forms between the silicate layers which lead to a shift of T_g to lower temperatures [202]. Similar to the silica layers, this could also be the case within the agglomerates in the materials discussed in this work.
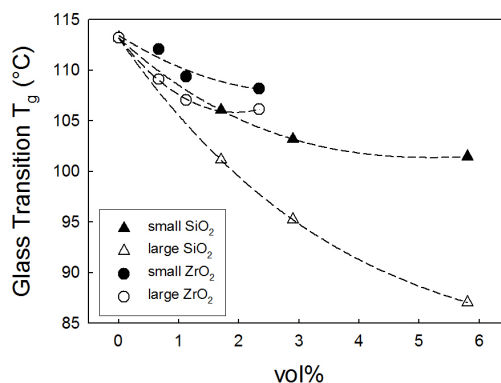
Figure 5.22: Glass transition temperature T_g of modified epoxy nanocomposites with different filler content.

The hardness impression did not show cracks at the edges. The hardness increases with increasing nanoparticle content up to 142 % for the sample containing 5.6 vol% large silica nanoparticles as shown in Figure 5.23. The zirconia nanocomposites show a significant increase in hardness. In the case of both nanoparticle types, the effect is more pronounced for large particles than for small ones, in particular at higher filler content. This is due to the fact that hardness is dependent on the flow properties of the polymeric matrix. High local stresses are induced for hardness. Thus, it is expected that small nanoparticles are less effective as obstacles, whereas the opposite is the case for larger nanoparticles. In the case of a similar size of particle and domain range of the polymer coil, unique interaction behavior of inorganic and organic parts can take place manifesting in unexpected effects on the mechanical property of such

nanomaterials [200, 203]. An extended interfacial region in case of large particles is additionally one of the reasons for large effect on hardness in both cases.
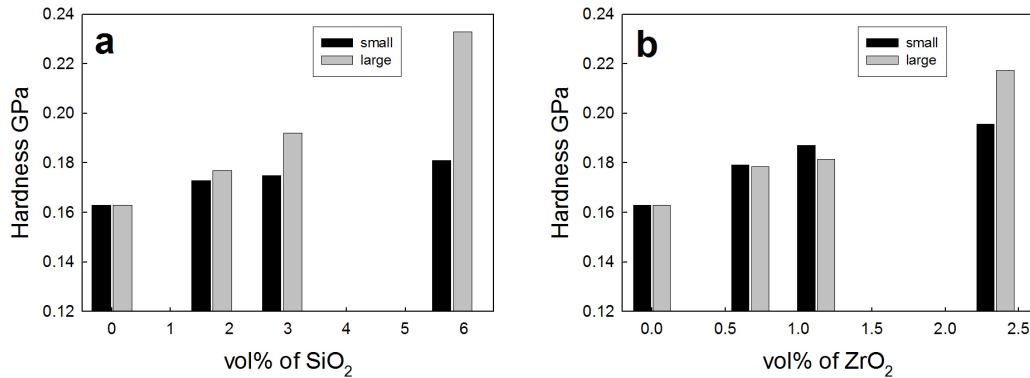
Figure 5.23: The effect of a) DEG-TMS modified SiO_2 and b) DEG-PPA modified ZrO_2 nanoparticles on the hardness of epoxy nanocomposites.

5.4.4 Conclusion

Epoxy nanocomposite films with SiO_2 and ZrO_2 nanoparticles were prepared via $in-situ$ curing using novel capping agents to enhance the dispersion quality. The strong bonding of this surface modification sustains the high temperature curing conditions. The inorganic moieties were homogeneously dispersed throughout the matrices and composite films retained good optical transparency. In the case of ZrO_2 nanocrystals the composite materials were highly homogeneous at the nanoscale, whereas in particular large spherical SiO_2-nanoparticles showed higher agglomeration. Modifying their surface with immobilized oligo ethylene glycol-chains, transparent epoxy resin nanocomposites were synthesized for variable inorganic contents. The addition of nanoparticles leads to a decrease in glass transition temperature, which is less pronounced for small zirconia than large silica nanoparticles. The hardness also increased for all investigated nanocomposites systems with increasing nanoparticle content. In this case, the incorporation of the larger nanoparticles leads tendencially to higher values compared with small particles.

6 The structure of feather keratin

In the first part of this chapter, the stability of feather keratin was confirmed by scanning the rachis of a blue and a white peacock feather along the whole length of the fiber. The second part describes different $in-situ$ SAXS measurements to determine a more detailed image of the arrangement of the keratin proteins within the filament.

6.1 Keratin homogeneity in the tail feathers of Pavo cristatus and Pavo cristatus mut. alba

The keratin structure in the cortex of peacock's feathers is studied by X-ray diffraction along the feather, from the calamus to the tip. It changes considerably over the first 5 cm close to the calamus and remains constant for about 1m along the length of the feather. Close to the tip, the structure loses its high degree of order. We attribute the X-ray patterns to a shrinkage of a cylindrical arrangement of β-sheets, which is not fully formed initially. In the final structure, the crystalline beta-cores are fixed by the rest of the keratin molecule. The hydrophobic residues of the beta core are locked into a zip-like arrangement. Structurally there is no difference between the blue and the white bird.

This chapter is based on the publication [S4].

6.1.1 Introduction

Recently the evolutionary development of feathers, the transition from Reptilia to Aves, and the associated capacity of flying [204, 205, 206, 207, 208] have received considerable attention. The evolutionary question is paralleled by the chemical one, the dichotomy between "hard" alpha-keratin in mammalia, and "soft" feather beta-keratins in reptiles and birds [209]. Concerning the nomenclature, there is some confusion in the literature. Astbury [210] stretched alpha-keratin to what he called a beta-form. Obviously their alpha- and beta- keratins have the same chemical composition, differing only in structure like two phases under stress. The feather beta-keratin is chemically different, but gives similar diffraction patterns to Astbury's stretched alpha [25].

The increased interest in feathers in general has led Weiss and Kirchner [211] to investigate one particular type in one particular bird, the tail covert feathers of the

peacock, both blue and white. The chemical, biochemical and mechanical differences between the blue and the white animal are but little. Pavo cristatus and Pavo cristatus mut. alba belong to the same species, the latter is a subspecies and not an albino form. White parents beget white offspring, blue parents blue offspring. The tail feathers are not used for flying but serve for sexual display. For that purpose they are long and thin, mechanically speaking they are slender beams. They consist of an outer cortex in the form of a circular hollow self-similar cone, filled by a low density foam, the medulla. Both are made of the same keratin, which is subsequently called peacock keratin. In what precise sense this is identical to commonly called beta-keratin or not, is a delicate question [212]. Chemically however, Weiss and Kirchner [211] have ascertained that the composition of our peacock keratin is identical to the F-keratin from Larus novae-hollandiae (Silver gull) [213]. Polarized light microscopy, Figure 6.1, reveals that the cortex is not uniform in the radial direction, but is a multilayer structure. This has been anticipated on the diffraction level by Busson et al. [214].
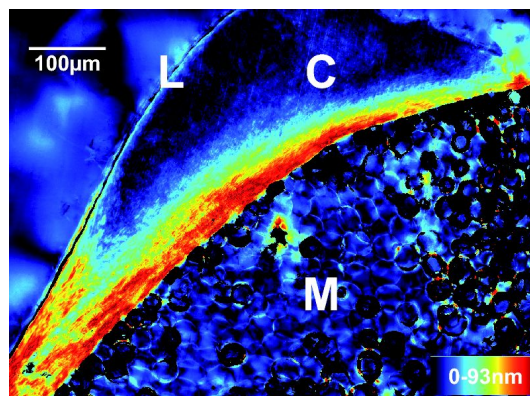
Figure 6.1: Polscope (Cri Abrio System, L.O.T. Oriel, Germany) image of a rachis cross-section. Below the diagonal the foamy medulla structure (M) can be seen. It is surrounded by the cortex (C) of varying thickness, appearing moon-shaped. This is sub-structured into layers. Towards the top left, the cortex is covered by protective, presumably lipid, layer (L). Birefringent retardation (0-93 nm) is colour coded.

Each such feather (Figure 6.2A) of about 2 mm diameter at the base and 1m length is produced once a year, amounting to a production rate of about 1 cm/day during the winter-spring growth period. The diameter of the feather keeps increasing (Figure 6.2B), which amounts to ever increasing production volumes per day. Although the geometry changes considerably, the quality of the material produced remains surprisingly uniform. Weiss and Kirchner [211] showed that Young's modulus of the cortex varies at most ten percent between tip and calamus, say between November and March. The purpose of this note is to check how the mechanical

constancy is based on structural constancy. Is the keratin and its structural arrangement the same between tip and calamus? Does the diffraction pattern change? The structure of the feather keratin molecule is not perfectly known. Moreover, the arrangements of the crystallized β-sheets [215] concerns from proline to proline only 31 amino acids (3.3 kDa) of the 98 amino acids (9.8 kDa) of the entire molecule. If, and how the rest of the molecule, after all two thirds and consisting of a 20 amino acids long N-terminus and a 47 amino acids long C-terminus, are crystallized and leave a mark on the diffraction pattern has remained open to speculation.
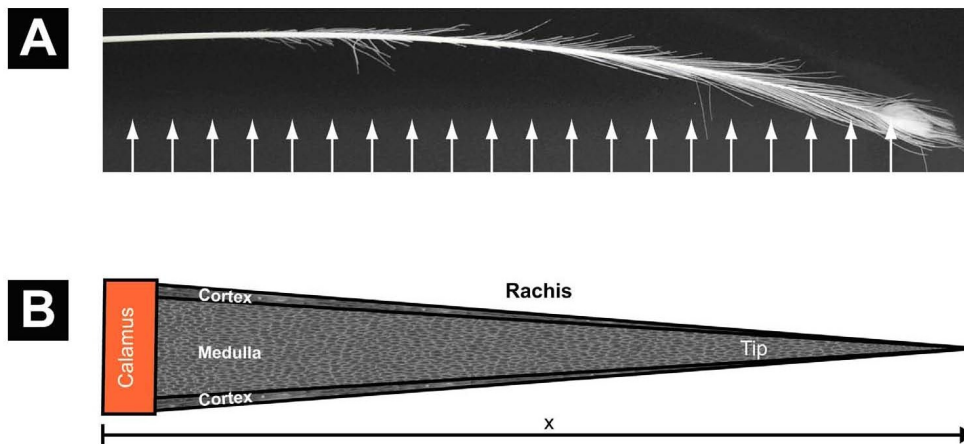
Figure 6.2: (A) The tail cover feather of Pavo cristatus sub. alba subjected to X-ray investigation. The arrows indicate approximately the multiple beam positions. (B) Sketch of the conical shape of the rachis. Both outer diameter and cortex thickness decrease linearly from the calamus to the tip, forming a self-similar cone filled by the medulla. Diffraction patterns were taken from the cortex only.

Avian feathers are strongly textured, the axes of the fibrous protein and of the rachis being parallel. Early X-ray diffraction favoured an arrangement of pleated sheets [216] with a helical structure [217, 218]. The structure of the molecule was identified from X-ray diffraction patterns of a seagull feather [29] as a helical arrangement of four repeating units per turn with a pitch length of 9.5 nm. Two twisted β-sheets are aligned along a perpendicular diad in a left-handed way, whereas the twist in the sheets is opposite to the one of the helix [29]. Fraser and Parry [219] showed that within each β-strand a well-defined oscillation in hydropathy exists, which is consistent with the residues alternating between inner and outer surfaces of the residues. These authors refined the original model and proposed two possible configurations for hairpin turns in the β-sheets and a high concentration of hydrophobic residues in the interface between the sheets related by the diad [215].

In one of the models, there is a strong interaction of the two components within the helix with a smaller distance of arginine sidechains of only 0.4 nm, whereas in their complementary model the distance is 0.68 nm [215]. Due to this smaller distance, which facilitates dimerisation, they favoured the first model, but they concluded that a stabilizing influence from the formation of disulfide linkages is rather unlikely as the cysteine residues are not close enough. The longitudinal texture of swan, goose, and ostrich feathers was studied by synchrotron radiation along the feather from the calamus to the tip [220]. The observed decrease of half-width of three specific reflections (i.e. a higher axial alignment of the keratin molecules with respect to the feather axis) was related to an increase of the Young's modulus for the two flying birds [220]. This was the starting point for the present work. We focus on a precise determination of the structure along the length of a peacock's feather, between the calamus and the tip with the eye of the feather.

6.1.2 Experimental

The tail covert feathers of a white and a blue peacock were obtained commercially (Claude Nature, Paris, France). Different feathers of the same peacocks were used in Weiss and Kirchner (Weiss and Kirchner, 2010a) and the present research. Feathers were stored at 24°C in a laboratory environment of 45% rel. humidity before testing. Small angle X-ray scattering (SAXS) measurements were performed with Cu K_α radiation from a rotating anode generator (Nanostar, BRUKER AXS) equipped with a pinhole camera and an area detector (VANTEC 2000). The samples were mechanically cleaned from the medulla foam, cut into stripes of about 4 cm in length and single strips were measured at a sample to detector distance of 14 cm. The exposure time for each pattern was 1800 seconds and the beam diameter at the sample was 0.5 mm. The distance of the measured spots was reduced to 5 mm for the piece close to the calamus for higher positional resolution. The SAXS intensity patterns were averaged to obtain the scattering intensity $I(q)$, where $q = (4\pi/\lambda)sin\theta$ is the scattering vector, 2θ the angle between incident and diffracted beam, and $\lambda = 0.1542$ nm the X-ray wavelength. Precisely, the two-dimensional X-ray patterns were evaluated according to the inserts in Figure 6.3, left image: For the lateral (equatorial) and the axial (meridional) reflections, the intensity was projected to the respective axes (q_x in equatorial direction, q_z in meridional direction, where the latter coincides with the long axis of the filament and the length of the rachis). To determine the intensity distribution with respect to the azimuthal angle χ, the 2D-patterns were integrated in the regime of each of the reflections, respectively. Background correction was performed by integrating the same regions without sample, subtracting these integrated intensities and taking into account the absorption of the respective sample. The intensities of the reflections were fitted with Gaussian functions to determine the maxima and the half-widths in reciprocal space and then converted into distances and distributions in real space. Differently,

for the intersheet distance/interchain distance reflection, the center of gravity of the peak was evaluated, as the shape of the reflection was more rectangular than Gaussian.

Four reflections of the diffraction patterns exemplarily shown in Figure 6.3 were evaluated:

- (A) The axial reflection of the fourth layer line. It corresponds to the length of the repeating units, about 9.5 nm, which is the pitch of the helix.

- (B) The first lateral (equatorial) reflection. It corresponds to the distance between packed filaments.

- (C) The intense axial reflection from the tenth layer line. From its splitting the approximate radius of the helix can be determined by searching for the first maximum of the appropriate Bessel function [221] $J_n(2\pi Q r_{cyl})$. Q is the position of the maximum in reciprocal space and r_{cyl} the radius of the cylinder. The order n of the Bessel function, $n = 2$, follows from the selection rule for feather keratin ($l = n + 4m$, Fraser et. al. [29], with $l = 10$ being the layer line index, for possible integers n and m). Fraser et al. [29] observed that this reflection is absent in keratin denaturated by steam; they attributed it therefore to the outer parts of the molecule, which are less stable than the central crystalline beta-core.

- (D) The broad equatorial peak. It was attributed to the interchain distance [217] or the intersheet distance [29]. We follow here the latter interpretation, evaluated the centre of gravity Q of this reflection and converted it to a radius r_{core} by using the second maximum of the Bessel function of zero order, $J_0(2\pi Q r_{core})$. The intersheet distance is then twice this value, $2\ r_{core}$.

The justification to use two different radii for the structure, r_{core} and r_{cyl}, is that Fraser et al. [29] observed the tenth reflection only in the native, unsteamed keratin. As mentioned above, they argued that it stems from the outer parts of the molecule, as the pleated sheet portions of the molecule are more resistant to denaturation due to the regular two-dimensional arrays of hydrogen bonds. The two different radii correspond therefore to the radius of the crystalline beta core and the outer parts of the molecule, respectively [29].

For clarity the evaluated reflections (A), (B), (C), (D) as well as the offset angle between the axial and the lateral reflection are marked in the left part of Figure 6.3. The central part shows the distances in real space inserted into the structure proposed by Fraser and Parry [219]. All error bars in Figures 6.4-6.8 are the sum of fit errors and the positional uncertainty (the finite sample thickness divided through sample-to-detector distance). Errors of wavelength and detector resolution were neglected, as they are either small or do not shift the maximum of the peaks considerably.
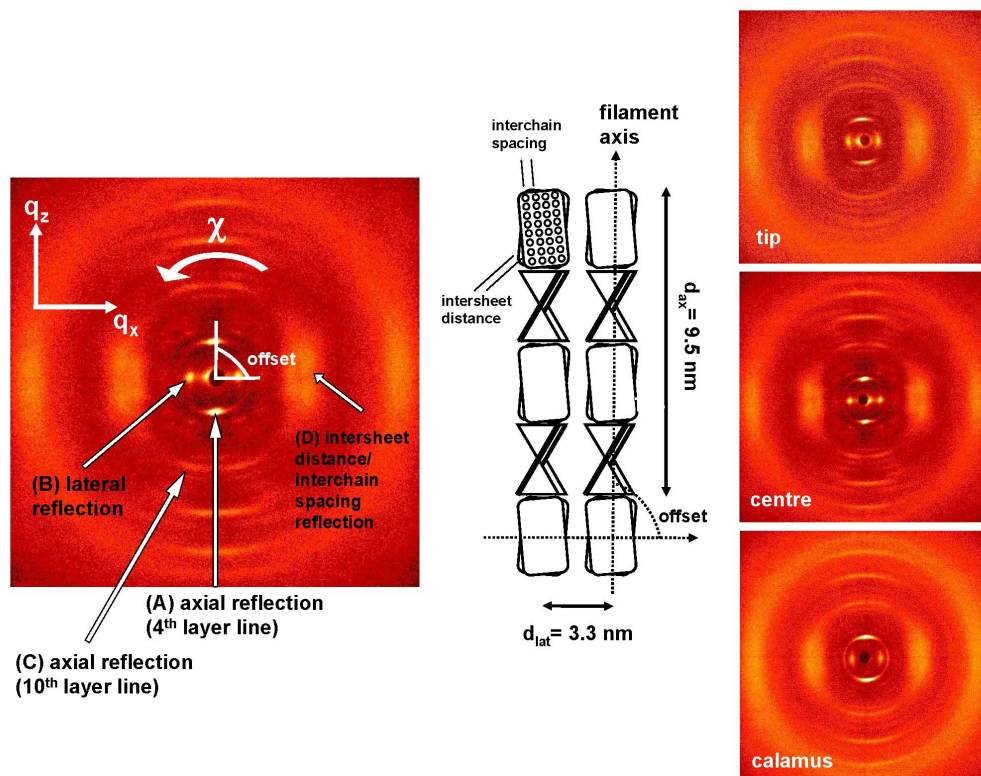
Figure 6.3: The four reflections analyzed, (A), (B), (C), (D), are indicated on a typical diffraction pattern. Corresponding real space arrangement proposed by Fraser and Parry [219] for avian keratin. Three typical scattering images along the length of a white peacock feather, from the regions close to the calamus, the centre and close to the tip.

6.1.3 Results

Three examples of scattering images are shown at the right of Figure 6.3. These are for the white peacock, one from the region close to the calamus, one in the centre and one close to the tip of the feather. The images clearly show the higher orientation with respect to the filament axis in the centre region (which covers most of the feather's length), as the azimuthal spread of these reflections is significantly smaller. Evaluation of the axial (A) and the lateral reflection (B) leads to Figure 6.4: the triangles, the distances in axial direction, are obtained from the 4th layer line (A). Four times this value is the length of the repeating unit of about 9.5 nm. The lateral packing (circles) is obtained from the lateral reflection (B). Gray symbols are for the blue, open symbols for the white peacock. The abscissa is divided into two parts to allow for the strong change in the region close to the calamus. The ordinate has two separate regions for the respective reflections. The lateral packing distance decreases over the first 50 mm from the calamus, whereas the axial distance first increases and then decreases again. This means that the pitch of the helical structure increases first and then decreases, whereas concomitantly the lateral distance in the perpendicular direction continuously shrinks.

Figure 6.5 shows the mean misorientation angle (the intensity spread of the reflection with respect to the azimuthal angle χ, described by the Gaussian half-width) for the axial (A) and lateral (B) reflections. Their cause is the misorientation between keratin filaments and rachis axis. Over the first 50 mm the misorientation angle of the structure decreases, but remains unchanged for most of the length, between 30 and 800 mm. Near the tip, the half-widths increase again. The spread in the azimuthal angle (B) is mainly controlled by the mosaicity of the structure. This suggests that the two strands forming the helix increasingly align with the filament and rachis axis and form a highly oriented structure beyond about 50 mm from the calamus.

Another significant change concerns the angle between the first axial (A) and lateral (B) reflections, Figure 6.6. It stems from the orientation of the keratin filaments along the long and the perpendicular axis, respectively. The angle strongly decreases over the first 50 mm of the rachis, beyond it remains constant at a value of 90°. This clearly indicates that the arrangement of the filaments at first is not perpendicular to their long axis, but differently inclined, until the length axis of the filament is perfectly perpendicular to their arrangement in the lateral direction.

Due to the helical structure, the 10th layer line (C) is split. From the distance between the maxima an approximate radius of the cylindrical helix can be found by searching for the maximum of the appropriate Bessel function [221]. Figure 6.7 shows this cylinder radius r_{cyl} along the length of the feather evaluated from the tenth layer line. It first increases and then decreases to a final value of r_{cyl}=1.6 nm, where twice this value - the cylinder diameter - is slightly smaller than the cylinder distance from the first lateral reflection (Figure 6.3).

The core radius r_{core}, where twice this value is the intersheet distance, was ob-
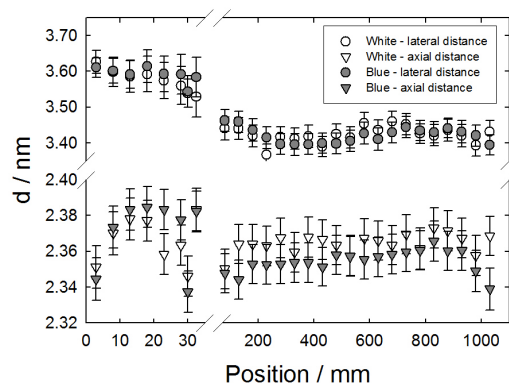
Figure 6.4: Positional change of the fourth layer axial reflection (axial - triangles) and the first lateral reflection (lateral - circles) along the length of the rachis of the feather: Open symbols, white peacock, gray symbols, blue peacock. Note that the abscissa is broken to allow for the strong change in the region close to the calamus, the positions 0-30 mm.

tained from the diffuse and broad lateral reflection (D) and is shown in Figure 6.8, also by searching the corresponding maximum of the appropriate Bessel function as described in chapter 6.1.2. It is constant along the whole length of the rachis. The alternative interpretation as interchain distance [217] leads to the same conclusion that the crystalline core beta structure is nearly identical over the whole length of the rachis.

6.1.4 Discussion

The X-ray diffraction data show that over the 50 mm close to the calamus the degree of order increases, but the final stable structure is only reached beyond this point. In particular, a significant shrinkage of the cylinder radius from 1.8 to 1.6 nm is observed (Figure 6.7). This is consistent with the shrinkage of the lateral distance between filaments to approximately 3.4 nm, roughly twice the value of the cylinder radius of the filaments (Figure 6.4, circles). Simultaneously, an orientational change of the filaments from an obtuse angle to a perfect perpendicular geometry is observed (Figure 6.6). Also the misorientation angle of the filaments with respect to the length axis of the rachis decreases considerably (Figure 6.5). However, only a small decrease of only 1% of the length of the repeat unit (the pitch of the helix in axial direction) was observed (Figure 6.4, triangles). The pitch, which is four times the d-spacing of the fourth layer line, is 9.5 nm and agrees well with the value measured in seagull feather keratin [29]. Likewise, the intersheet distance (twice the value of r_{core}, Figure 6.8) remains also nearly constant.

For the structural development we propose therefore the model of Figure 6.9: Dur-
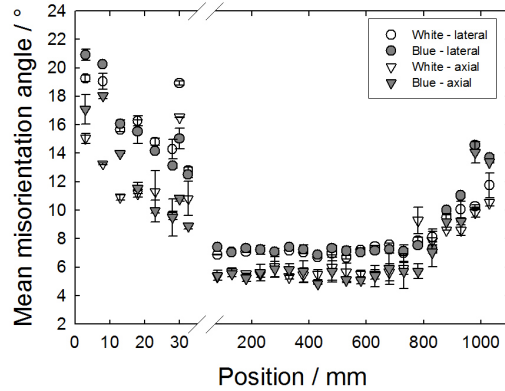
Figure 6.5: Mean misorientation angle along the length of the feather, i.e. the Gaussian half-width of the azimuthal spread of the axial reflection from the axial fourth layer line, (axial - triangles), and the first lateral reflection, (lateral - circles). Open symbols, white peacock, gray symbols, blue peacock. The abscissa is broken to allow for the strong change in the region close to the calamus, positions 0-30 mm.
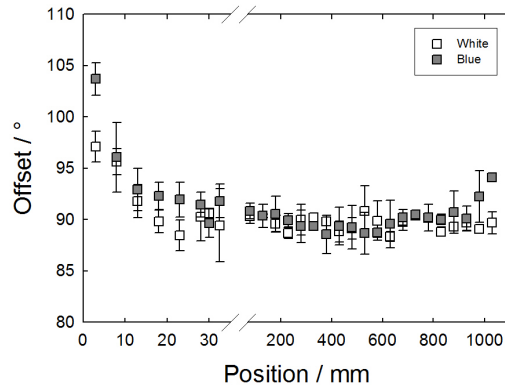
Figure 6.6: Offset angle between the axial reflection (A) (length direction of keratin filament) and the lateral reflection (B) (perpendicular direction of the keratin filament). Open symbols, white peacock, gray symbols, blue peacock. The abscissa is broken to allow for the strong change in the region close to the calamus, positions 0-30 mm.
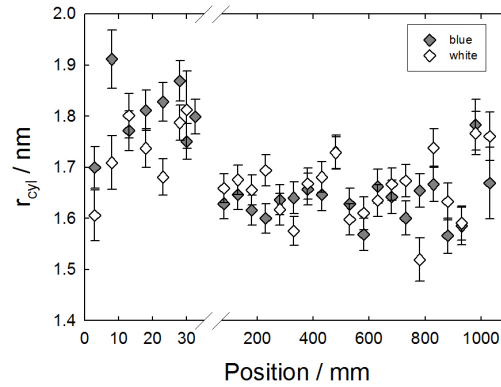
Figure 6.7: Cylinder radius evaluated from the axial tenth layer line (C). Open symbols, white peacock, gray symbols, blue peacock. Note the expanded scale near the calamus, positions 0-30 mm.
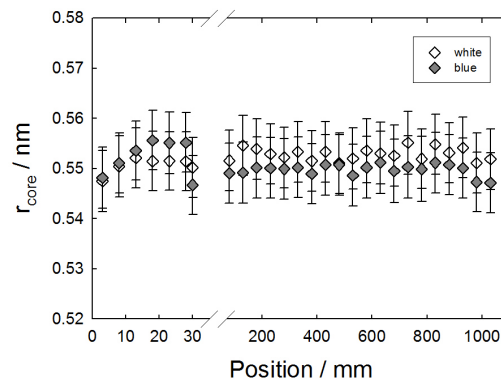
Figure 6.8: Core radius r_{core} (half the value of the intersheet distance) from the broad lateral reflection (D). Open symbols, white peacock, gray symbols, blue peacock. Note the expanded scale near the calamus, positions 0-30 mm.
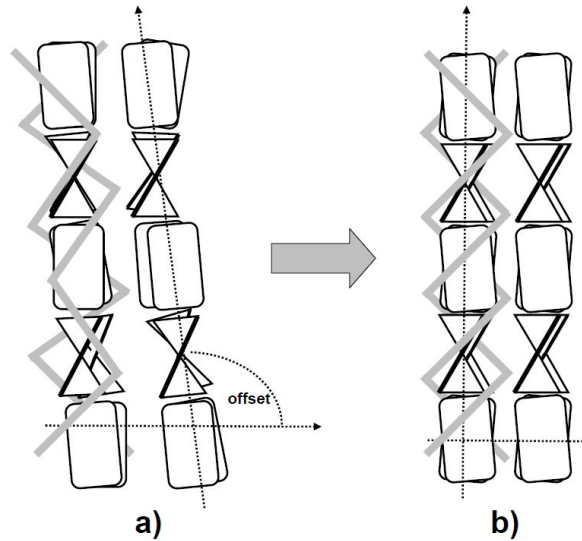
Figure 6.9: Structural change from the calamus to the central region: Close to the calamus, (a), the β-sheets are misoriented with respect to the filament axis. Away from the calamus, (b), they are increasingly aligned and form a highly oriented structure with filament axis and lateral packing being perfectly perpendicular. The grey bars symbolize the outer parts of the molecule, which are not organized in pleated sheets. Both the diameter of the filaments and their distance decreases.

ing growth, the pairs of β-sheets forming the filament are already present, but their initial orientation with respect to the helix is not well fixed over the first 50mm from the calamus. Beyond they fall into a highly aligned and oriented structure. The half-widths of both the axial and lateral reflections decrease. The strong increase in alignment is accompanied by only a small shortening of the axial repeat unit, and no change of the intersheet distance. This leads to the conclusion that topologically the crystalline beta structure of the strands is formed early on. Only some small rotations are needed to fix the structure in a zip-like mechanism, where the sidechains perfectly interleave along the filament axis [215]. The high concentration of hydrophobic residues between the two strands and their interaction is important for the assembly process. They stabilize the final structure [215].

The main shrinkage appears in the so-called "matrix", the portion of the molecule not forming the core beta structure. It may be speculated that these outer portions of the molecule, 67 of 98 amino acids, surround the crystalline core beta structure and lead to a contraction of the structure as a whole. Since the shrinkage is deduced from the tenth layer line (C), known to be sensitive to denaturation [29], we suspect that it can be attributed to the end parts of the molecule. The 10% "matrix" shrinkage is accompanied by a change of the offset angle between the filament axis

and the lateral packing of the filaments. It changes from 100° to 90° within the first 50 mm from the calamus. One can imagine a structure with a hard and stiff crystalline core of 31 amino acids (3.3 kDa) wrapped into the 67 amino acids (6.5 kDa) of the tails.

6.1.5 Conclusion

The structural development of the keratin filament within a peacock's feather is studied by X-ray diffraction along the length of the feather, from the calamus to the tip, where the eyes are located. The structure changes considerably over the first 50 mm and then remains constant over almost the total length (1 m) of the feather. Close to the tip, the structure loses its high crystallinity, probably because there the cortex function ceases to be mechanical, but serves to organize the optical eye patterns. We propose an explanation based on structural models in the literature [29, 215, 219]. Whereas the crystalline core is nearly unchanged (first a small increase and then a decrease of the helical pitch), the distance between neighbouring filaments decreases significantly. Concomitantly, the cylinder radius decreases if evaluated from the tenth layer line, which is nearly absent in denatured keratin. This leads to the interpretation that the inner crystalline core is very stable, whereas the outer portions of the molecule possibly surround the inner core and stabilize the structure as a whole. Concomitantly with the shrinkage, also visible by the decrease of the distance between the filaments, the angle between the filament axis and the lateral packing approaches the perfect perpendicular arrangement of 90°. It may be speculated that this structure resembles stiff columns built up from small crystallographic units, which are joined together and stabilized by the tails of the molecules wrapped around them, the "matrix". This might increase the bending resistance of the structure. Finally, it is worth noting that for quill embroidery [222] artisans use only strips cut from the central part (30 to 80 cm) of the feather.

6.2 The lateral and axial structure of feather keratin

Feather keratin is a highly conserved protein of 98 amino acids synthesized intracellularly in aves. In the cortex of the tail covert feathers of the peacock it forms a crystalline structure. We suggest that the structure is linked by disulfide bonds between the nine cysteines of the molecule. The molecule is probably not embedded in a noncrystalline matrix, but parts of the molecule act as stiff crystalline fibers and others form a less ordered material surrounding the crystalline core. $In-situ$ tension and compression tests as well as rotation experiments were performed to investigate the changes in axial and lateral structure and therefore, based on these X-ray diffraction data from *Pavo cristatus* feathers, to develop a revised model

for the molecular assembly of F-keratin, which integrates biochemical structure and mechanical experiments.

6.2.1 Introduction

From the biological point of view, the F-keratin molecule is small (98 amino acids, 9.8 kDa) compared with other molecules such as collagen, which can consist of up to 600-3000 amino acids. Chemically its most prominent feature is the presence of 9 cysteins and the complete absence of relatively large amino acids such as Tryptophan. Fully stretched this protein would take up a length of 35 nm. Evolutionary, it is a lately invented protein, from 200-180 Million years ago, when skin and agumentae of reptiles transformed into feathers. Mechanically it is not superior to bone, which existed before. In avae, unlike bone, it is renewed annually by molting. Unlike bone, once produced, it cannot be repaired, being biologically an inert matter.

From the structural point of view, feather keratin is extremely conservative between species and within one animal [S4]. The quantitative biochemical analysis of peacock feather keratin can be found in the work of Weiss and Kirchner [222] and is presented in Figure 6.10, which agrees with the composition of seagull keratin [213] and allows also the conclusion that the sequence of 98 amino acids is the same as in the seagull. For the underlined block, Fraser and Parry proposed a crystallographic arrangement of beta-barrels and relegate both N-terminus (from alanine to glutamic acid, positions 1 to 20 in Figure 6.10) and the C-terminus (from, glutamine to cysteine, positions 52 to 98 in Figure 6.10) to an amorphous matrix, akin to the situation in silk [215]. Despite the biological importance of the molecule, its spatial structure has not yet been determined. So far all attempts [29, 215] have been guided by the idea that its structure and microstructure are similar to silk. The existing model is mainly based on calculations described by Fraser et. al. [29], who concluded from polarized infra-red spectra that 28% of residues sit in an antiparallel chain pleated sheet conformation. The calculated number of chains in the repeating units of Fraser et al. is 4, and the number of residues per chain is 8 [29]. Therefore, they assigned the observed signals to the most conserved central 32 amino acids (21-51), underlined in Figure 6.10. The crucial point in the model of Fraser et. al. is that the authors expect the pleated sheet portions of the molecules to be more stable due to the regular two dimensional array of hydrogen bonds [29]. However, the molecule contains a total of 9 cysteins, of which only 2 sit at positions 22 and 26 within the presumably crystalline part of the molecule, visualized by gray shading in Figure 6.10 [213]. The other 7 are located at positions 1, 6, 9 and 18 of the N-terminus, and 88, 95 and 98 of the C-terminus. The high activation energy (1.78 eV) and small activation volume (0.83 nm^3) of plastic deformation [223] rules out hydrogen bonds and indicates breaking of disulfide bonds formed somewhere between cysteins. We propose therefore that the geomatrical arrangement of the cysteines has an important mechano-chemical role and is not a purely random distribution

within the amino acids sequence. They link the molecules to form a macroscopic material and to provide a certain but limited plasticity. This is different than in other biological materials: In silk, thought to consist of 25 vol% of stacks of beta-sheets embedded in some matrix [224], the beta-blocks provide strength and the matrix provides toughness [225]. In F-keratin, the central 32 amino acids supposedly stacked in beta-barrels, have tentatively been placed in a matrix made up of N- and C-termini. The implied structural similarity between silk [225] and F-keratin is not reflected in a mechanical similarity, though: Young's moduli are 22GPa for silk and 3GPa for F-keratin, the yield stresses are 3 GPa at 50% strain [226], and 100 MPa at 5%, respectively. There is little functional similarity between silk and F-keratin, also cellular production and function of the two are very different. These observations deemphasize the role of a matrix, even questions its existence.
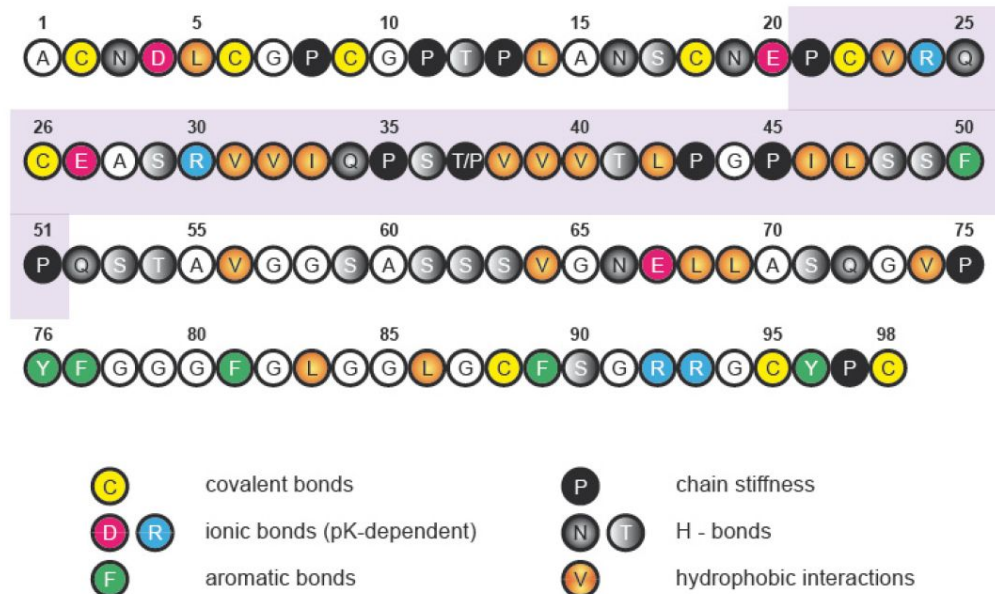
Figure 6.10: Sequence of amino acids of the feather keratin.

Based on previous mechanical work [222, 223] on the tail covert feathers of the peacock, *Pavo cristatus* and *Pavo cristatus mut. alba*, further structural and mechanical work, obtained by $in-situ$ small-angle X-ray scattering, is presented. Our research focused on the role of the N- and C-termini emphasize the role of the cysteines. $In-situ$ experiments also allow to compare the strain at the nanoscopic level with the macroscopic one. This enables to reveal a possible hierarchical structure as found for many biological tissues. In particular, the experiments may elucidate the absence or presence of a matrix.

6.2.2 Experimental

The rachis was broken in liquid nitrogen and then coated with a 3.5 nm layer of gold/palladium alloy for characterization by scanning electron microscopy using a Zeiss Supra 55 VP microscope equipped with two secondary and one backscatter electron detector. Images were recorded with a gun accelaration voltage of 2.00 kV, using a magnification of times 100 to 10^5 and a resolution of 200 nm - 200 μm.

For the X-ray experiments, the samples were measured in vacuum in transmission geometry using a rotating anode X-ray generator with a pinhole camera (Nanostar, Bruker AXS) and CuK$_\alpha$ radiation monochromatized and collimated from crossed Goebel mirrors. The X-ray patterns were recorded with a 2D position sensitive detector (Vantec 2000) at a sample to detector distance of 13 cm. Measurements were performed first with a beam perpendicular to the length axis of the rachis, the preferred orientation of the structure, which is called "fiber geometry". Then, the sample was rotated for 90° and images were taken parallel to the length axis of the rachis ("parallel geometry"). For the fiber geometry, intensities were projected to the z-axis (length axis of the fiber in real space and in reciprocal space). For the parallel geometry, intensities were radially averaged. Both intensities were corrected from background scattering to obtain the scattering intensities either in dependence on q_z, the component of the scattering vector in z-direction, or in dependence on the absolute value of the scattering vector $q = 4\pi/\lambda \sin\theta$, where 2θ is the scattering angle and $\lambda = 0.1542$ nm the X-ray wavelength. In a second experiment, X-ray patterns were taken in perpendicular geometry $in-situ$ during loading in a self-constructed test equipment. For the tension experiments, a sample geometry of 40 mm length and 2.5 mm width was chosen with the thickness being the natural grown rachis of about 0.1 mm. The samples were glued with epoxid resin between two copper plates, clamped with both ends, which led finally to a gage length of d(0) = 27.5 mm. For the compression geometry, the gage length was reduced to 6 mm to avoid kinking. The time required to take one X-ray image was 300 seconds, and about 20 load steps could be measured up to the fracture of a sample. The macroscopic strain was measured from the cross-head displacement. For a crystalline structure such as the rachis of feather keratin, the distance of the repeating units could be calculated from the position of the peak maximum in reciprocal space e.g. for the axial reflection by $d_{ax} = 2\pi/q_{max,ax}$. The nanoscopic strain ϵ_{nano} in the respective direction is then obtained by the shift of the position of the respective reflection with load or stress:

$$\epsilon_{nano}(\sigma) = \frac{d_{ax}(\sigma) - d_{ax}(0)}{d_{ax}(0)} \tag{6.1}$$

Differently, the macroscopic strain is obtained from the crosshead displacement D of the tension test equipment by

$$\epsilon_{macro}(\sigma) = \frac{D(\sigma) - D(0)}{D(0)} \tag{6.2}$$

A compliance correction was not required as its effect is significantly less than 1%.

6.2.3 Results

The first part concerns the longitudinal structure of the peacock feather, which is discussed on the basis of the results from the $in - situ$ tension/compression experiments. The second part is based on the rotation experiment and SEM measurements to characterize the lateral arrangement of the keratin filaments.

Axial structure of the keratin

The strain evaluation focuses on the two reflections with the highest intensities, which are the so-called 4th layer line (the first strong reflection in axial direction, with the distance of 2.4 nm, which is one fourth of the axial repeating unit of about 9.5 nm [29]) and perpendicular to it, the first lateral reflection (the repeating distance in lateral direction), both described in detail in chapter 6.1.2. The change of these two distances, the axial and the lateral distance, allows the calculation of the nanostrain. The nanostrain is the normalized measure of deformation at the molecular level. It is shown in Figure 6.11 in dependence on the macrostrain, the deformation of the whole sample at the mm-level. A slight anisotropy between tension and compression can be observed. The increase of the nanoscopic strain in axial direction after exceeding a macroscopic strain of 0.05 percent in compression is the consequence of macroscopic buckling of the sample. This was also visible by a close inspection by the naked eye. The nanoscopic buckling is visible in the broadening of the half width at half maximum (mean misorientation angle) of the lateral as well as the axial reflection shown in Figure 6.12. Due to the vanishing intensity of the axial reflection during compression, only a few data points could be plotted.

Also the intensities of the axial and lateral reflection behave surprisingly under load. Indeed, Figure 6.13 shows that the intensity of the longitudinal peak decreases with increasing deformation during the tension test and compression. This could be interpreted as an increase in lateral order. The opposite behavior, a decrease in intensity, was observed for the axial nanostrain. This decrease indicates an increasing disorder, both in tension and compression during loading.

In cooporation with our partners from the Leibniz Institute of New Materials, Ingrid Weiss and Helmut Kirchner, the arrangement of amino acids was modeled taking restrictions from biochemistry into account. The N-terminus could be arranged in a hairpin configuration as shown in Figure 6.14. This could be possible due to a turn caused by the proline-threoline-proline (Pro-Thr-Pro) configuration and would therefore generate two new cysteines pairing that are linked by disulfide bonds. One has to be aware that two cysteines, on positions 9 and 26, are still not bonded and are available for further linking.

The crystalline β-core, consisting of several prolines, can be formed by 2 turns in a S-shaped configuration as presented in Figure 6.15 and therefore differs from the pleated β-sheets proposed by Fraser et. al. [29]. Mechanically, this arrangement
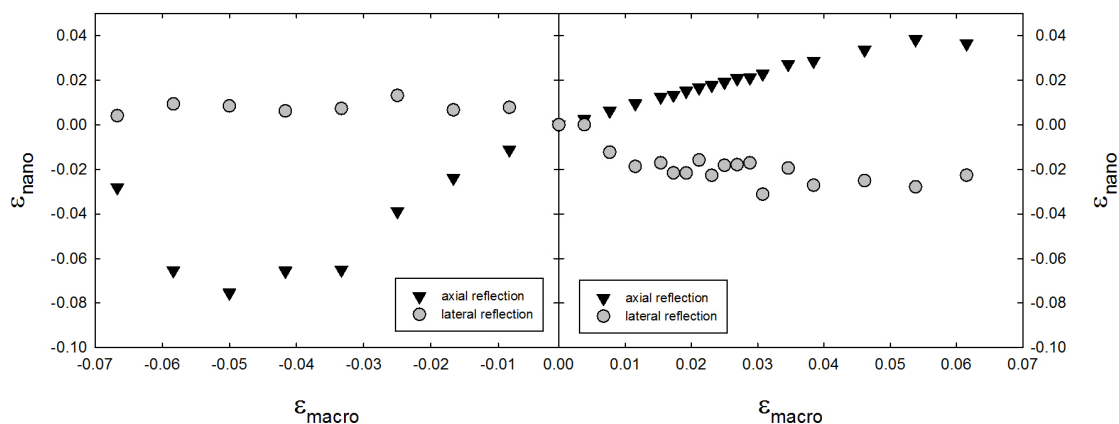
Figure 6.11: Nanoscopic axial and lateral strains, as calculated from the shifts of the strong 2.45 nm axial reflection, the "fourth layer line" (triangles), and the first lateral reflection at 3.4 nm (circles). Left part of the figure refers to axial compression, right part to axial tension. The abscissa shows the macroscopic longitudinal strain, ϵ_{macro}, calculated from the macroscopic length change.

could explain the slight compression-tension asymmetry on the nanoscale, as it could be rotated as a whole or the "S" could be differently deformed due to its intrinsic anisotropy.

Chemically remarkable is the amino acid sequence of the C-terminus. In the first part of this terminus (right image in Figure 6.16), the relative abundance of glycines and serines suggests a high flexibility. Due to its geometrically similarity with a rope, it can be suspected that its mechanical function is similar to the function of a rope to be inextensible, but slag in compression. The middle part of the C-terminus (Figure 6.16, middle) contains 3 aromatic rings, which is therefore of interest, as these aromatic rings can be available for possible cross-linking or hooking functions. In the last part of the C-terminus (Figure 6.16) three further cysteines are contained, still available for disulfide bonds, as well as two further aromatic rings.

Lateral order of the keratin filaments

Figure 6.17 shows the 2D X-ray patterns in fiber geometry versus parallel geometry. The strong preferred orientation along the z-axis is visible on the left of Figure 6.17 and in Figure 6.18, and the structure is rotated around this axis of symmetry as can be concluded from the Debye-Scherrer rings on the right of Figure 6.17. Whereas the high number of peaks in Figure 6.18 are the consequence of a pronounced crystallinity and a long range order with a distance of the repeating units of 9.5 nm [S4, 29], the diffuse outer and the relatively sharp inner ring in the right part of Fig-
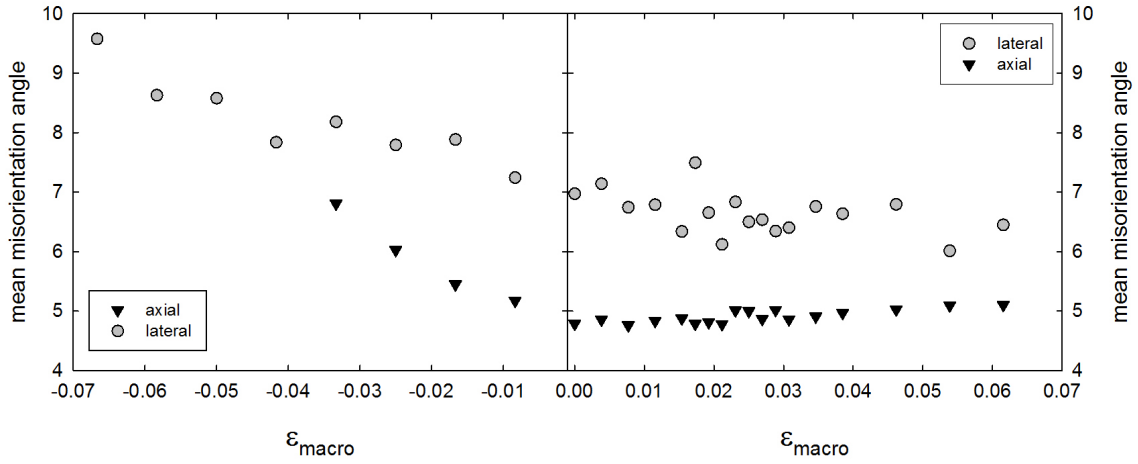
Figure 6.12: Mean misorientation angle (half width at half maximum of the spread of the scattering intensity in azimuthal direction). The axial reflection is given as black triangles and the lateral reflection as gray circles.
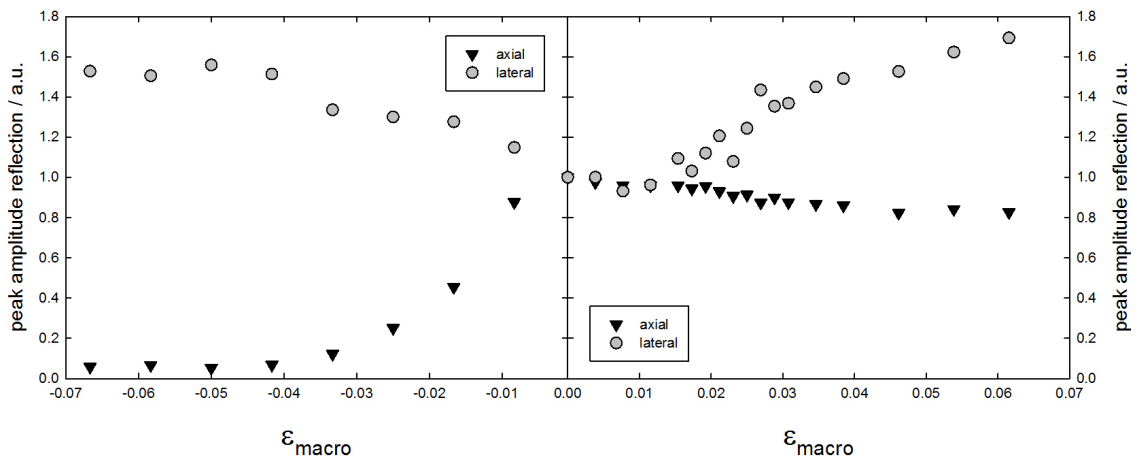
Figure 6.13: Maximum intensity (peak amplitude) of the axial and lateral reflection as function of the macroscopic strain, both in compression (left) and tension (right).
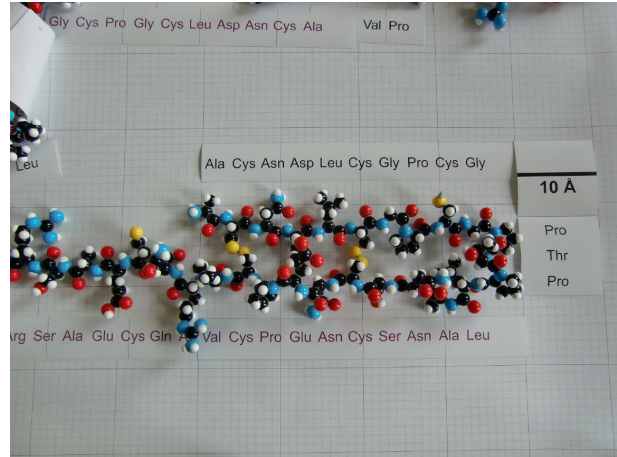
Figure 6.14: Molecular model of the N-terminus of the feather keratin.
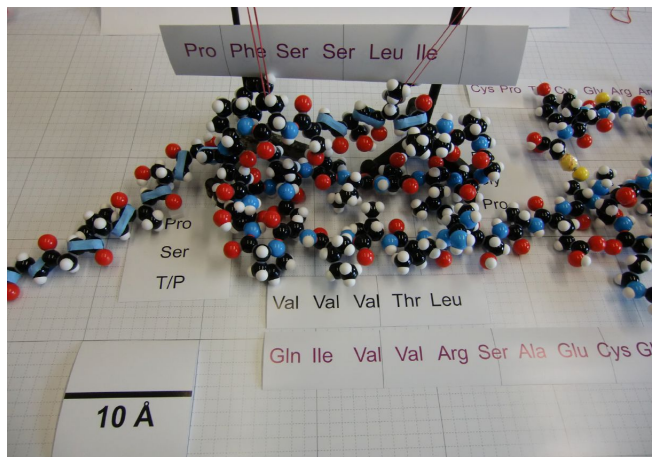
Figure 6.15: Molecular model of the crystalline β-core of the feather keratin.
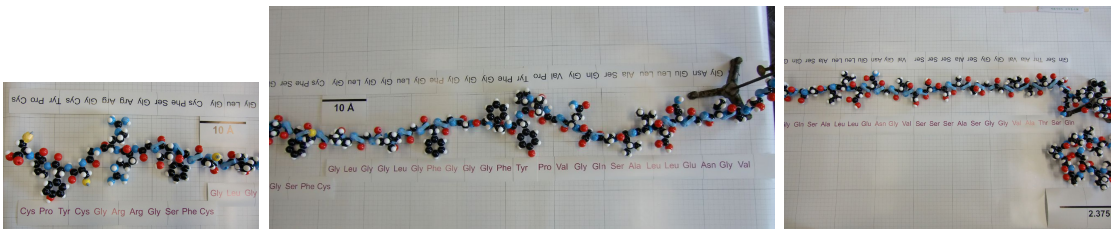
Figure 6.16: Molecular model of the C-terminus of the feather keratin, due to its length shown in three parts. On the left, position 98 with a cysteine at its end is visible, on the right, the connection to a part of the folded crystalline β-core is shown.

ure 6.17 as well as the relative weakness of distinct higher order reflections (visible in Figure 6.18) indicate a short range order with a relative broad distribution of about 1 nm and a slight long range order of units or a weakly ordered one-dimensional chain with a distance of about 3.4 nm in lateral direction.

For SEM imaging, the outer rachis of the peacock feather was broken in liquid nitrogen to obtain fracture surfaces. The feather was manually bent in the liquid nitrogen in two different directions to result in two different fracture surfaces, one with a crack propagating perpendicular to the feather axis and the other propagating along. It is visible in the top of Figure 6.19 that - though one would expect a brittle crack under liquid nitrogen conditions - no straight crack could be achieved. In the contrary, the crack is strongly deflected and the fracture surface appears as many long and extended triangles. In the two figures at the bottom of Figure 6.19 it is clearly visible that there are two layers in the outer rachis with different structure. The outer part has a thickness of about 15 microns and is amorphous as measured by scanning across the thickness with a synchrotron radiation beam [214]. The second part is the crystalline highly structured one [214], with a thickness of approximatly 60 microns. Figure 6.20 is an enlargement of Figure 6.19, where on the tip of the triangle-shaped fracture surface small bundles with a diameter between 50 and 200 nm can be observed, which form a further structural level with a size of about one micron. This lateral organisation is probably the reason for the strong crack deflection even at liquid nitrogen temperature, but further experiments have to investigate this theme more in detail to clarify the specific role of each structural level on the direction of crack propagation.

6.2.4 Discussion

Model for the feather keratin filament

Calculating the initial slope from Figure 6.11, the result is that the initial nanostrain is about 80% of the macrostrain. Taking into account that the material is mainly crystalline but in the cross-section there are additionally less crystalline and even amorphous regions [214], which might contribute less to the elastic behaviour of the composite, two fundamental statements can be made:

1. There is no intermediate hierarchical level in axial direction, so that macrostrain and nanostrain are to a good approximation identical. This is clearly different to the majority of biological structures, such as bone or wood [19, 20, 22], two prominent examples for biological tissues.

2. The material is a molecular crystal, certainly determined here at the level of the beam size with 0.5 mm diameter, but very probably along the total length of the rachis of 1 m, as the structure is nearly identical along the whole rachis [S4].
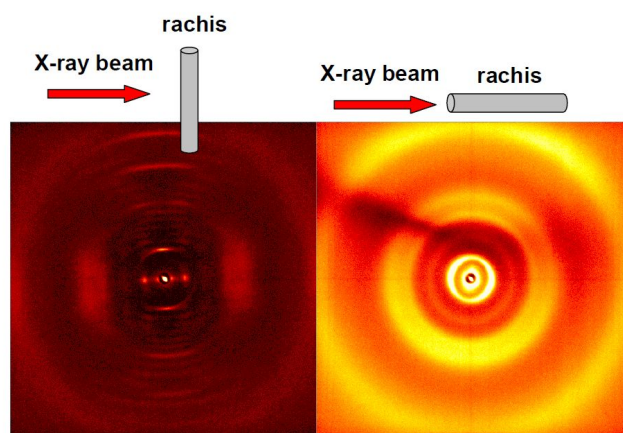
Figure 6.17: Scattering patterns of the feather keratin during rotation from a perpendicular position of the feather to the X-ray beam to a parallel position.
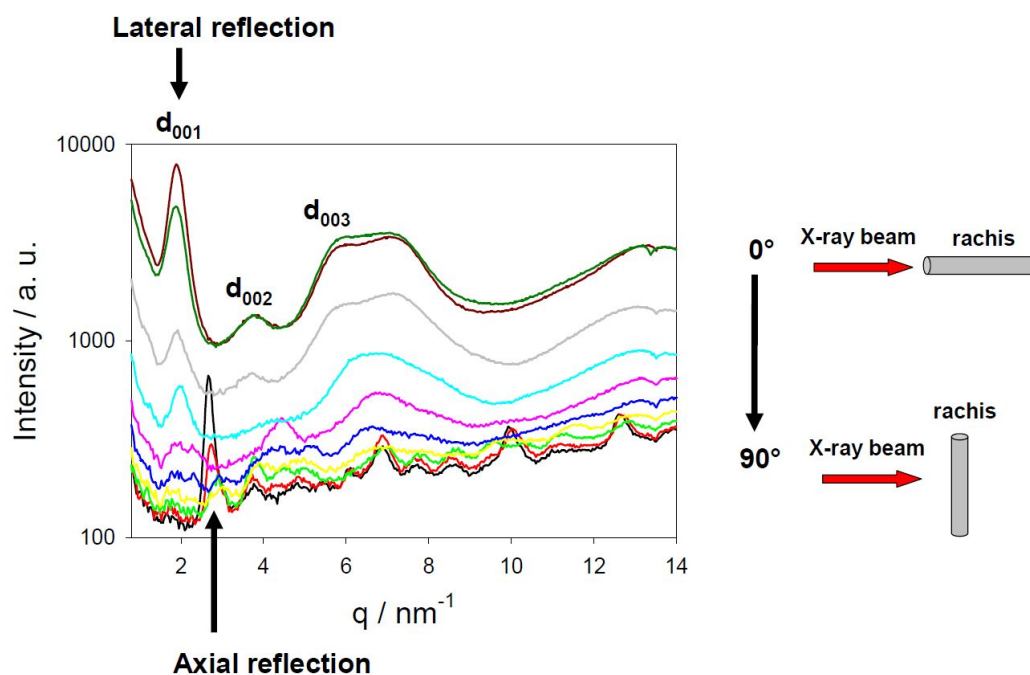
Figure 6.18: Scattering intensities of the lateral structure of the feather keratin during rotation from a perpendicular position of the feather to the X-ray beam to a parallel position in 10 degree steps.
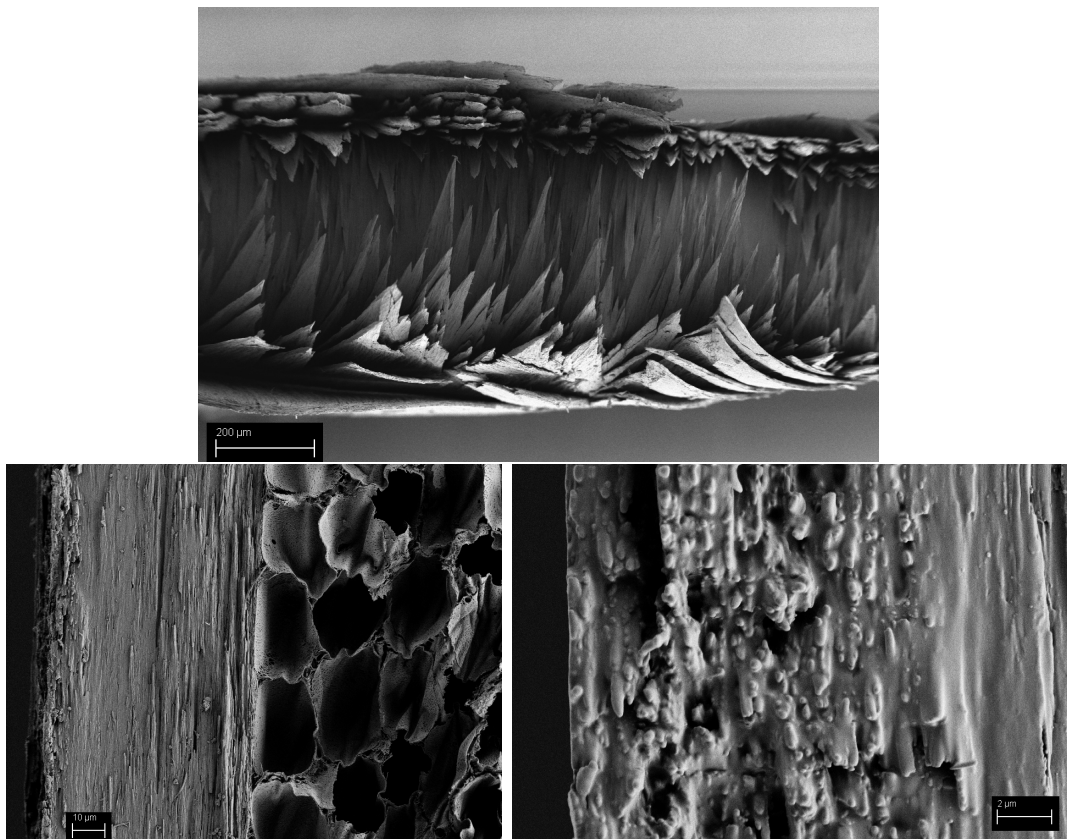
Figure 6.19: SEM images of a peacock feather, broken in nitrogen perpendicular to the feather axis (top) and along the feather axis (bottom left) with an amorphous outer part of the rachis (bottom right).
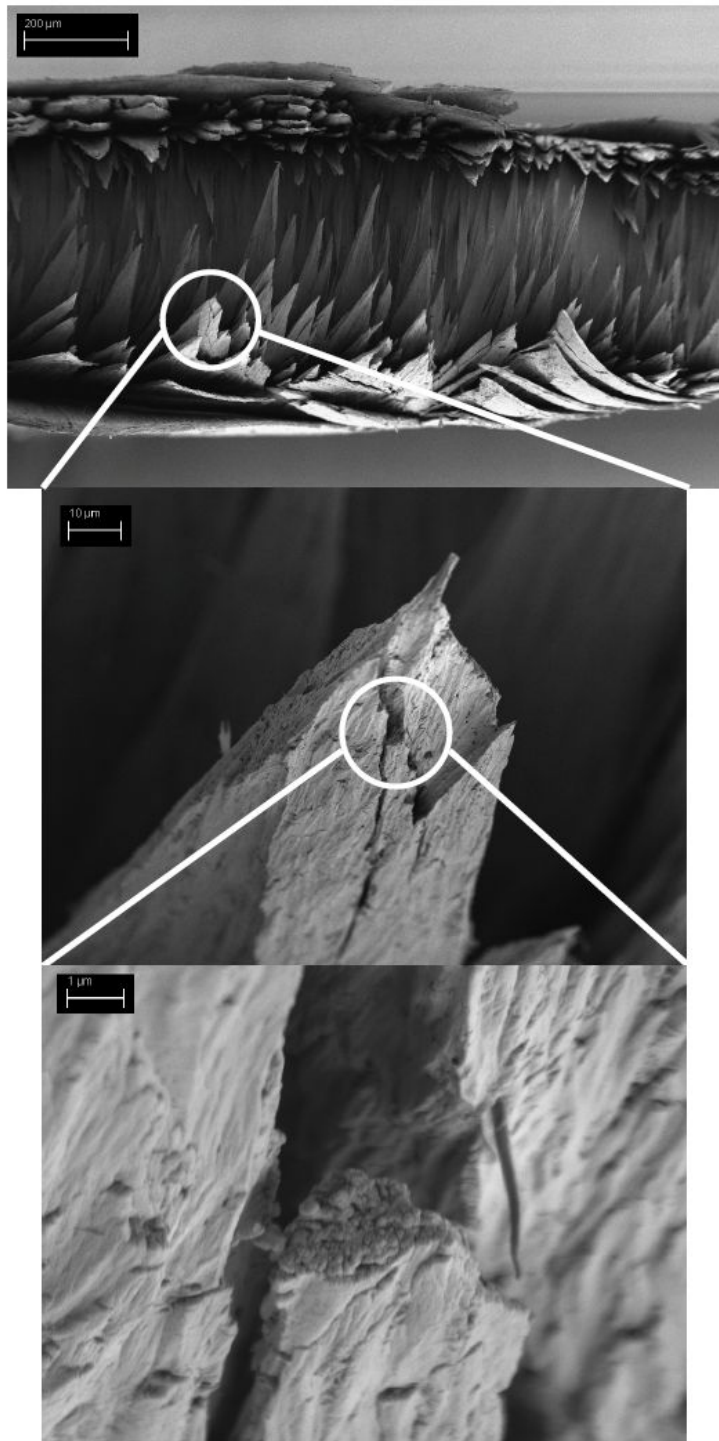
Figure 6.20: SEM imaging of the lateral feather structure.

With the knowledge of the strain in load direction (along the length axis of the rachis) and perpendicular to it, one can calculate the Poisson ratio in tension and compression from the negative ratio of lateral to axial strain. Surprisingly, the Poisson ratio is calculated with about 0.75 in tension and 0.1 in compression, where only the part of the stress-strain curve before macroscopic buckling was taken into account. An explanation for this behavior can be given, when considering the N- and C-termini presented in the Figures 6.14 and 6.16, which are proposed to be crucial for the 3D arrangement. The end segment of the C-terminus can be linked in good accordance with two of the remaining cysteines of the N-terminus, which is shown in Figure 6.21. A strongly linking in axial direction is achieved as 8 of 9 cysteines of the keratin protein are used to form 4 disulfide bonds. Only one of 9 cysteine can be used for lateral linking to another cysteine of a neighboring filament and therefore provide a weak linkage between the filaments in lateral direction. This arrangement of N- and C-termini explains the high Poisson ratio in in tension, as there is now an endless molecule in axial direction and no dense packing of the filaments and it explains the low Poisson ratio in compression and the buckling on the nanoscale supported by the broadening of the peak (the increase of HWHM) in compression (Figure 6.12).
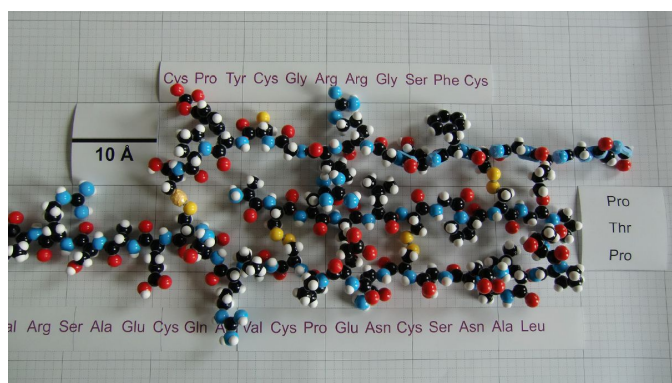
Figure 6.21: Possible model of a link of the end part of C-terminus to the cysteines from N-terminus.

The construction of a model with all amino acids visualizes the structure and helps to understand the 3D steric restrictions, as large residues take more space than small ones. It also indicates the geometry of certain sequences, such as a stiff and angular one (Pro-Thr-Pro in the N-terminus) or obviously soft ones (like the first part of the C-terminus). Furthermore, it helps to clarify the possible occurence of intramolecular or intermolecular disulfide bonds between the hairpin and the end of the C-terminus of the same or next nearest filament. As buckling occured in compression, one can assume that the C-termini link intramolecular within the filament and hardly intermolecular to neighboring filaments. The hooklike activity of aromatic rings, located in the C-terminus, can also not be underestimated, as it

could guide the cysteines to form the disulfide bonds.

Model for the lateral arrangement of the keratin filaments

The rotation experiment allows to investigate the lateral order of the filaments. A slight long range order is observed as visible in Figure 6.18. This experiment supported the view of a 1D folded chain as sketched in Figure 6.18b. Due to the few observed higher order lateral reflections, it may be speculated that the filaments are arranged like a spiral, a so-called "bamboo roll", presented in Figure 6.22c. The bamboo rolls build up the 50-200 nm bundles, which furthermore build up the larger bundles of a diameter of about 1 μm. Therefore, a hierarchical structure is expected in lateral direction.

One can also speculate, how the axial and lateral arrangement of the keratin filaments influences the crack behavior of the peacock feather. A possible interpretation could be the bundle arrangement on the microlevel causing the triangle-shaped fracture. Further investigations have to be made to answer this question.

6.2.5 Conclusion

A peacock feather was investigated by tension and compression tests as well as via rotation with $in - situ$ small-angle X-ray scattering. The tension tests led to the conclusion that a hierarchical structure in axial direction can be excluded, as nanostrain and macrostrain were nearly identical. The structure of the feather can be seen as molecular crystal without any hierarchical levels. Furthermore, the lateral arrangement of the keratin filaments was described by scanning electron microscopy and the rotation experiment by SAXS as built-up of several hierarchies from the nano- to the macrolevel. On basis of the experiments, a modified model is presented, which points out the important role of the termini to build up an endless structure in axial and link these columns in lateral direction. This model leads to the following improvements in comparison to the model proposed by Fraser et. al. [29].

- C- and N-termini are central for building up the structure.

- The hook-like configuration of the N-terminus leads to an endless molecule. Therefore, nanostrain is nearly the same as macrostrain.

- The linkage of the C-terminus with the hook-like N-terminus stabilizes the structure in axial direction. This results in an endless, fiber-like molecule. Furthermore, 8 of 9 cysteine amino acids are required to form disulfide bonds within this configuration.

- The last remaining cysteine is able to link the columns to each other. In lateral direction, several hierarchical levels from the nano- to the macroscale build up the peacock feather.

a)

side view

b)

top view

3.4 nm

c)

"bamboo" roll

~50-200 nm

3.4 nm

d)
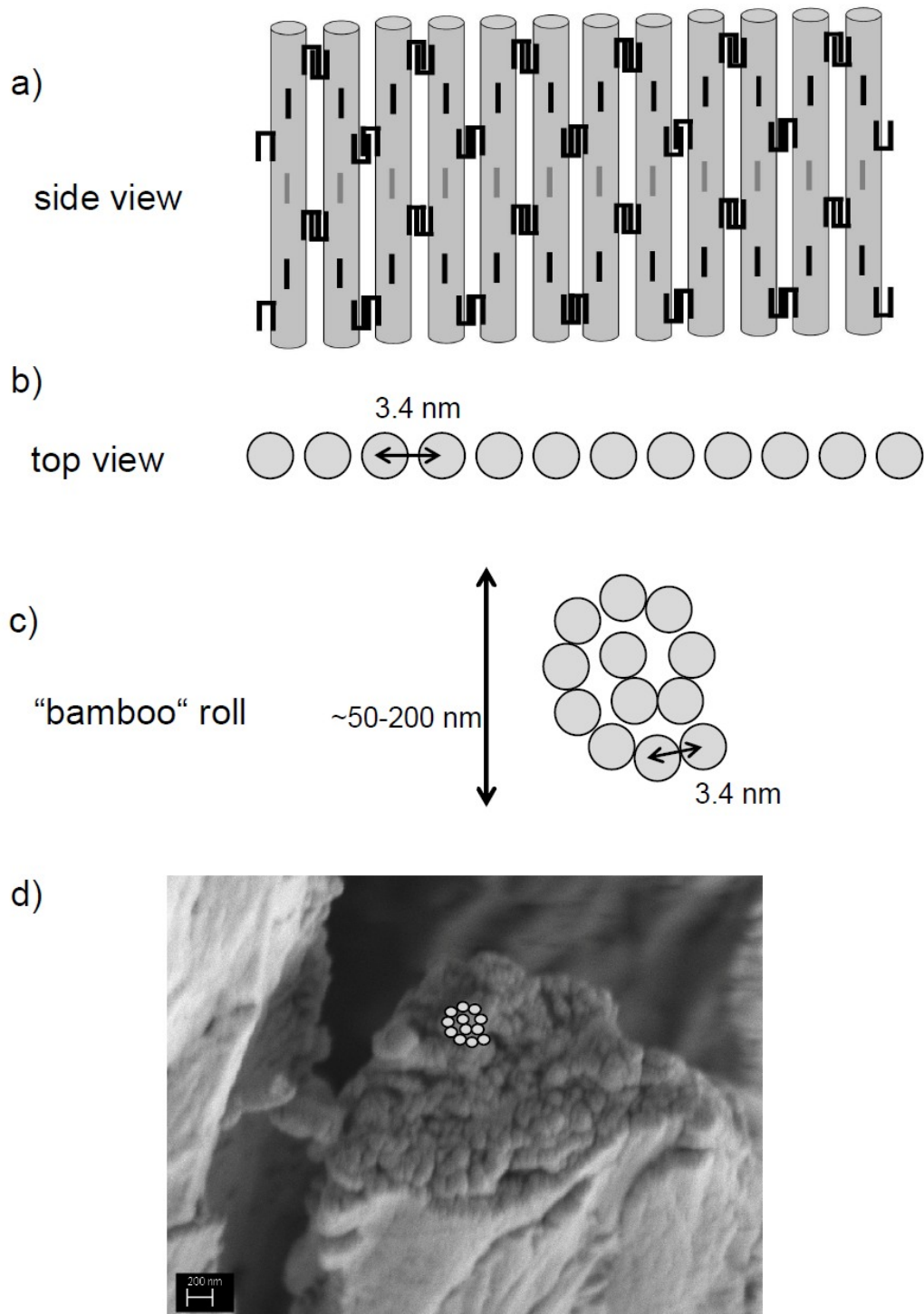
Figure 6.22: Schematic model of the lateral structural level in the feather keratin.

This model is a first approximation of the keratin arrangement, however, further investigations have to be made to shed light on the final structure of the feather keratin protein.

7 Summary

The aim of this thesis was the characterization of nanocomposites and biomaterials by small-angle X-ray scattering to reveal the influence of size and shape of nanosized particles and their interaction with a polymer matrix on the structural and mechanical properties. On the one hand, oxide nanoparticles, SiO_2 and ZrO_2, in different size ranges (5-50 nm) were surface-functionalized for an enhanced dispersion in an organic polymer matrix and in addition, the nanocomposites were investigated by mechanical or thermomechanical tests. On the other hand, feather keratin, consisting of a hydrophobic core and two termini, was studied by several $in-situ$ SAXS experiments as well as scanning electron microscopy to develop a model for the structure and a possible solution for the arrangement of its termini.

The two oxide nanoparticle systems, amorphous, spherical SiO_2 and crystalline, irregular-shaped ZrO_2, were studied in detail by SAXS, TEM, DLS, BET and XRD to determine the "true" size of the nanoparticles. Different nummerical values from the respective method as well as a considerable influence of the nanoparticle type could be found. SAXS and TEM exhibited a nearly perfect coincidence in the results for the size. Large differences were found for the BET method, as large silica exhibited a slight microporosity and zirconia nanoparticles an irregular shape and a high surface roughness. DLS leads to slightly higher values for silica and considerably higher values for zirconia compared to SAXS and TEM, which was attributed to the effect of the hydrodynamic shell. This effect was even more pronounced for the irregular-shaped zirconia than for silica. Last but not least, XRD gave reasonable results for the size of small zirconia and delivered the correct size of the small crystallites, which built up the larger particles consisting of polycrystalline zirconia. As considerable differences between the test methods were found, the respective result for the size of a nanoparticle has to be taken with caution. As shape and porosity have an influence on numerical results, more than one test method is favourable.

A central theme of the thesis was the surface-functionalization of nanoparticles and its effect on the agglomeration behavior. Alkyl chains, often used as coupling agent systems in research, were attached to the surface of the zirconia nanoparticles with a size of 6 nm and were subsequently investigated by SAXS and FTIR. The ordering of these alkyl chains as self assembled monolayers (SAM) at the surface could be disturbed by four co-capping molecules of different shape: An increasing amount of co-capping molecules led to an increased disorder of the SAMs. The disorder in turn causes a blueshift of the C-H vibrational resonances of the dodecyl-chain-methylene-units in the FTIR spectra. The influence of the ordering of the alkyl

chains at the nanoparticle surface was also visible by SAXS as a "zipper" effect with neighboring particles. Thereby, zirconia nanoparticles formed agglomerates due to bilayer formation of the SAMs between the particles. Disorder of the SAMs led to less agglomeration, which could be followed by SAXS as the decrease of the hard-sphere volume fraction, i. e. the decrease of the probability to find an other particle in vicinity. The degree of the disorder depended not only on the amount, but also on the type of the added co-capping agent: The small methyl-moiety showed less disorder for a small amount of co-capping agent and also only a slight disorder of the alkyl chains. The planar pyryl-moiety disturbed the order of the alkyl chains moderately although it is of bulky shape. An explanation for this behavior was that it ordered itself and formed islands, which are alternating with the alkyl chains. The co-capping agent phenyl presented an almost linear trend of disordering with increasing amount. The most effective disordering was obtained by the sterical de-manding tert-butyl-moiety. In conclusion, a clear correlation between blueshift and particle agglomeration was observed by two fundamentally different methods: the spectroscopic method FTIR, which directly probes the molecular surface structure and the structural method (SAXS), which determines the degree of agglomeration of the nanoparticles.

Varying surface-functionalizations had not only influence on the agglomeration be-havior but also on the dispersion of the nanoparticles in the polymer matrices. It was found that the interplay between nanoparticles, surface-functionalization and poly-mer is crucial for a homogeneous material. Unmodified and modified silica and zir-conia nanoparticles were embedded in three different polymer matrices, polystyrene, PMMA and epoxy resin, and systematically investigated by SAXS and TEM.
First, silica nanoparticles were functionalized with dodecyl chains and incorporated into PS and PMMA. A high tendency to agglomerate was found compared with unmodified silica, whereas surface-functionalizations with polymerizable end groups enhanced significantly the dispersion of the particles. This enhancement was shown for dodecyl- and phenyl-moieties with polymerizable end groups such as Styr- for PS and methacryloyl for PMMA. A further effect visible for silica in PS and PMMA was the enhanced tendency of larger nanoparticles to agglomerate compared with small ones. Enthalpic reasons correlated to a stronger interaction between parti-cles than between particles and polymer, however the relation of particle radius to radius of gyration of the polymer played a crucial role for the dispersion of the par-ticles. Therefore, an optimum choice of the capping agent molecule, the size of the nanoparticles and the polymer itself and its radius of gyration are important for a homogeneous dispersion of the nanofillers in these polymer matrices.
Second, zirconia nanoparticles were surface-functionalized with two different capping agents of varying spacer length but the same polymerizable end group, methacrylate, and then incorporated in PMMA. A nearly homogeneous distribution was obtained for the modified zirconia nanoparticles proben by TEM photographs and SAXS measurements, however, a shorter spacer length leads to even better dispersion.

Mechanical tests prove the enhanced hardness of these nanocomposites, especially for a nanofiller content of 10 wt%, wherefore the complex relation between size of the nanoparticles, their surface-functionalization, agglomeration and possible viscosity shear forces during preparation were responsible.

Third, a comparison of varying surface-functionalizations on the dispersion of the nanoparticles, was also performed for silica and zirconia in epoxy resin. The dispersion of the nanoparticles depended on an interplay of several effects in these systems. Polymerizable end groups such as epoxides were used to link covalently with the matrix, however, in the case of zirconia nanoparticles, high agglomeration was observed due to a homo-linkage between the particles. The interparticle interaction between the crystal facet shaped zirconia was more dominant compared to the particle-matrix interaction. Therefore, a low interacting modification such as diethyleneglycol on the surface of zicronia was favored to obtain high homogeneous nanocomposites. Contrary to that, the capping agent diethyleneglycol did not have any effect on an enhanced dispersion of the silica particles. An enhanced interparticle interaction was also observed for large silica nanoparticles with less curvature, however, small silica nanoparticles modified with capping agents using polymerizable end groups were highly dispersed in epoxy resin.

Fourth, the effect of different filler content on the thermomechanical and mechanical properties of epoxy resin nanocomposites was investigated in detail for diethyleneglycol modified silica and zirconia nanoparticles. The glass transition temperature decreased due to the addition of nanoparticles, however, the decrease depended on the type and size of particles. The hardness increased with increasing nanoparticle content for all investigated systems, especially with the incorporation of large nanoparticles.

A peacock feather was also characterized with small-angle X-ray scattering to determine the structure of the complex protein keratin. The scan along the feather axis allowed to identify changes in the structure over the first 50 mm, while the rachis remained stable over the whole length (ca. 1 m). Close to the calamus, the crystalline core of the molecule was nearly unchanged, however, the distance between the filaments decreased significantly. Similarly, the cylinder radius also decreased, which can be interpreted that the inner crystalline core is very stable, whereas the outer portions of the molecule surround the inner core and therefore, stabilize the structure over the whole feather length. According to this shrinkage, the filament axis arranged perfectly perpendicular to the lateral packing. The results from $in-situ$ tension and compression tests by SAXS of the peacock feather allowed to propose a modified model of the keratin protein. The advantage of this new model is that the N- and C-termini of the protein are now included in the model. Furthermore, the model gives a mechanism to form an endlessly columnar structure, which explains that macrostrain and nanostran are nearly equal in the tension and comprassion experiment. The rotation experiment as well as the SEM measurements let to the conclusion that in lateral direction many hierarchical levels exist.

7.1 Main conclusions

The final conclusions of this thesis are summarized in the following:

- The type and shape of nanoparticles as well as other parameters such as possible porosity lead to different numerical values for the size of the nanoparticles by different measurements methods. Therefore, the combination and comparison of different measurement techniques is helpful to find the "true" values.

- Alkyl chains build a self-assembled monolayer on the surface of crystal-faceted zirconia nanoparticles, which enhances the agglomeration behavior of the particles or diminishes it in case of the addition of co-capping agents. Two fundamentally different methods, FTIR spectroscopy probing the molecular surface structure and the structural method SAXS determing the degree of agglomeration, both allow to follow the effect of the co-capping agent on the order of the SAMs.

- The optimum choice of surface-functionalization for the respective type of nanoparticles to prepare homogeneous nanocomposites is strongly dependent on the polymeric matrix: The reason is that the matrix can either interact chemically (e. g. by polymerizable groups) or physically (e. g. controlled by varying spacers) with the nanoparticles.

- Mechanical properties of the nanocomposites such as hardness are enhanced by homogeneously dispersed nanoparticles, depending on their size and type.

- Peacock feather keratin arranges into a stable position during the first 50 mm of feather growth due to a probably shrinkage of the outer portions of the molecule surrounding the inner crystalline core. It remains stable over a length of 1 m.

- No hierarchical levels within the feather keratin were found in axial direction, as macrostrain and nanostrain from SAXS coincide in $in-situ$ tension tests. Differently, rotation experiments in SAXS as well as SEM revealed different hierarchical levels in lateral direction.

List of Figures

List of Tables

List of articles included in the thesis

[S1] S. Pabisch, B. Feichtenschlager, G. Kickelbick, H. Peterlik, *Chem. Phys. Lett.* 521 (2012) 91-97.

[S2] B. Feichtenschlager, S. Pabisch, H. Peterlik, G. Kickelbick, *Langmuir*, in print, DOI: 10.1021/la2023067

[S3] M. Sajjad, B. Feichtenschlager, S. Pabisch, J. Svehla, T. Koch, S. Seidler, H. Peterlik, G. Kickelbick, *Polym. Int.* 61 (2012) 274-285.

[S4] S. Pabisch, S. Puchegger, H. O. K. Kirchner, I. M. Weiss, H. Peterlik, *J. Struct. Biol.* 172 (2010) 270-275.

List of further publications

[P1] M. Bendova, M. Puchberger, S. Pabisch, H. Peterlik, U. Schubert, *Europ. J. Inorg. Chem.* 15 (2010) 2266-2275.

[P2] J. Svehla, S. Pabisch, B. Feichtenschlager, D. Holzmann, H. Peterlik, G. Kickelbick, *Macromol. Mater. Eng.* in print, DOI: 10.1002/mame.201100191

References

[1] H. Presting, U. König, *Mater. Sci. Eng. C* 23 (2003) 737-741.

[2] G. Kickelbick, *Prog. Polym. Sci.* 28 (2003) 83-114.

[3] C. Sanchez, B. Julián, P. Belleville, M. Popall, *J. Mater. Chem.* 15 (2005) 3559-3592.

[4] L. S. Schadler, L. C. Brinson, W. G. Sawyer, *JOM* 59 (2007) 53-60.

[5] T. Liu, I. Y. Phang, L. Shen, S. Y. Chow, W.-D. Zhang, *Macromolecules* 37 (2004) 7214-7222.

[6] B. J. Ash, R. W. Siegel, L. S. Schadler, *Macromolecules* 37 (2004) 1358-1369.

[7] M. W. Rowell, M. A. Topinka, M. D. McGehee, H. J. Prall, G. Dennler, N. S. Sariciftci, L.-B. Hu, G. Gruner, *Appl. Phys. Lett.* 88 (2006) 233506.

[8] C. J. Lomoschitz, B. Feichtenschlager, N. Moszner, M. Puchberger, K. Mueller, M. Abele, G. Kickelbick, *Langmuir* 27 (2011) 3534-3540.

[9] G. Kickelbick, *Introduction to hybrid materials*, Wiley-VCH, Weinheim (2007).

[10] M. L. Hair, C. P. Tripp, *Colloids Surf.* 105 (1995) 95-103.

[11] L.-H. Lee, *J. Colloid Interface Sci.* 27 (1968) 751-760.

[12] S. Onclin, B. J. Ravoo, D. N. Reinhoudt, *Angew. Chem., Int. Ed.* 44 (2005) 6282-6304.

[13] A. P. Philipse, A. Vrij, *J. Colloid Interface Sci.* 128 (1989) 121-136.

[14] A. Y. Fadeev, R. Helmy, S. Marcinko, *Langmuir* 18 (2002) 7521-7529.

[15] G. Guerrero, P. H. Mutin, A. Vioux, *Chem. Mater.* 13 (2001) 4367-4373.

[16] A. Ulman, *Chem. Rev.* 96 (1996) 1533-1554.

[17] M. Szekeres, J. Tóth, I. Dékány, *Langmuir* 18 (2002) 2678-2685.

[18] M.-A. Neouze, U. Schubert, *Monatsh. Chem.* 139 (2008) 183-195.

References

[19] R. Weinkamer, P. Fratzl, *Mat. Sci. Eng. C* 31 (2011) 1164-1173.

[20] J. W. C. Dunlop, P. Fratzl, *Annu. Rev. Mater. Res.* 40 (2010) 1-24.

[21] U. Wegst, M. Ashby, *Philos. Mag.* 84 (2004) 2167-2181.

[22] P. Fratzl, R. weinkamer, *Prog. Mater. Sci.* 52 (2007) 1263-1334.

[23] M. Heim, L. Römer, T. Scheibel, *Chem. Soc. Rev.* 39 (2010) 156-164.

[24] F. H. Silver, J. W. Freeman, G. P. Seehra, *J. Biomech.* 36 (2003) 1529-1553.

[25] W. T. Astbury, T. C. Marwick, *Nature* 130 (1932) 309-310.

[26] R. D. B. Fraser, D. A. D. Parry, *J. Struct. Biol.* 173 (2011) 391-405.

[27] R. O. Prum, A. H. Brush, *The Quaterly Review of Biology* 77 (2002) 261-295.

[28] D. Voet, J. G. Voet, C. W. Pratt, *Fundamentals of Biochemistry*, Wiley (1999) 124-158.

[29] R. D. B. Fraser, T. P. MacRae, D. A. D. Parry, E. Suzuki, *Polymer* 12 (1971) 35-56.

[30] Ch. Kittel, *Einführung in die Festkörperphysik*, Oldenbourg Wissenschaftsverlag GmbH (2006).

[31] N. W. Ashcroft, N. D. Mermin, *Festkörperphysik*, Oldenbourg Wissenschaftsverlag GmbH (2001).

[32] B. E. Warren, *X-ray diffraction*, New York: Dover Publisher (1990).

[33] B. D. Cullity, *Elements of X-Ray Diffraction*, Massachusetts: Addison-Wesley Publishing Company (1978).

[34] H. M. Rietveld, *J. Appl. Cryst.* 2 (1969) 65-71.

[35] A. L. Patterson, *Phys. Rev.* 56 (1939) 978-982.

[36] H. Peterlik, P. Fratzl, *Monatsh. Chem.* 137 (2006) 529-543.

[37] P. Fratzl, *J. Appl. Cryst.* 36 (2003) 397-404.

[38] D. I. Svergun, M. H. J. Koch, *Curr. Opin. Struc. Biol.* 12 (2002) 654-660.

[39] A. Guinier, G. Fournet, *Small-Angle Scattering of X-Ray*, John Wiley & Sons Inc. (1955).

[40] O. Glatter, O. Kratky, *Small-Angle X-ray Scattering*, New York: Academic Press (1982).

152

[41] L. A. Feigin, D. I. Svergun, *Structure Analysis by Small-Angle X-ray and Neutron Scattering*, New York: Plenum Press (1987).

[42] J. K. Percus, G. Yevick, *J. Phys. Rev.* 110 (1958) 1-13.

[43] D. J. Kinning, E. L. Thomas, *Macromolecules* 17 (1984) 1712-1718.

[44] O. Glatter, *J. Appl. Cryst.* 10 (1977) 415-421.

[45] O. Glatter, *J. Appl. Cryst.* 13 (1980) 577-584.

[46] L. Demeestere, J. Mast, *Diagnostic Pathology* 4 (2009) 5.

[47] J. Nebesářová, M. Vancová, *Microsc. Microanal.* 13 (2007) 248-249.

[48] K. Furuya, *Sci. Tech. Adv. Mat.* 9 (2008) 014110.

[49] L. Reimer, *Transmission Electron Microscopy*, Springer-Verlag (1984).

[50] J. I. Goldstein, J. L. Costley, G. W. Lorimer, S. J. B. Reed, *Scanning Electron Microscopy*, O. Johari, ed., liT Research Institute, Chicage, IL, vol. 1 (1977)

[51] B. J. Berne, R. Pecora, *Dynamic Light Scattering*, John Wiley (1975).

[52] S. Brunauer, P. H. Emmett, E. Teller, *J. Am. Chem. Soc.* 60 (1938) 309-319.

[53] M. A. Hernández, F. Rojas, V. H. Lara, *J. Porous Mat.* 7 (2000) 443-454.

[54] P. R. Griffiths, J. A. de Haseth, *Fourier Transform Infrared Spectrometry*, Chemical Analysis Series 83 (1986).

[55] W. Jiskoot, D. J. A. Crommelin, *Methods for Structural Analysis of Protein Pharmaceuticals*, AAPS Press, Arlingtion (2005) pp. 131-166.

[56] R. Y. Kannan, H. J. Salacinski, P. E. Butler, A. M. Seifalian, *Acc. Chem. Res.* 38 (2005) 879-884.

[57] V. Goertz, N. Dingenouts, H. Nirschl, *Part. Part. Syst. Charact.* 26 (2009) 17-24.

[58] J. Moonen, C. Pathmamanoharan, A. Vrij, *J. Colloid Interface Sci.* 131 (1989) 349-365.

[59] D. J. Tobler, S. Shaw, L. G. Benning, *Geochim. Cosmochim. Acta* 73 (2009) 5377-5393.

[60] D. L. Green, J. S. Lin, Y.-F. Lam, M. Z.-C. Hu, D. W. Schaefer, M. T. Harris, *J. Colloid Interface Sci.* 266 (2003) 346-358.

References

[61] S. Connolly, S. N. Rao, D. Fitzmaurice, *J. Phys. Chem. B* 104 (2000) 4765-4776.

[62] Y. Li, I. Akiba, S. Harrisson, K. L. Wooley, *Adv. Funct. Mater.* 18 (2008) 551-559.

[63] G. Beaucage, H. K. Kammler, S. E. Pratsinis, *J. Appl. Cryst.* 37 (2004) 523-535.

[64] H. K. Kammler, G. Beaucage, R. Mueller, S. E. Pratsinis, *Langmuir* 20 (2004) 1915-1921.

[65] A. Rizzuti, C. Leonelli, A. Corradi, E. Caponetti, D. Chillura Martino, G. Nasillo, M. L. Saladino, *J. Dispersion Sci. Technol.* 30 (2009) 1511-1516.

[66] J. L. Shi, C. W. Lu, C. L. Kuo, Z. X. Lin, T. S. Yen, *Ceram. Int.* 18 (1992) 155-159.

[67] W. Stöber, A. Fink, E. Bohn, *J. Colloid Interface Sci.* 26 (1968) 62-69.

[68] A. M. Lipski, C. J. Pino, F. R. Haselton, I. W. Chen, V. P. Shastri, *Biomaterials* 29 (2008) 3836-3846.

[69] Y. Murase, E. Kato, *J. Am. Ceram. Soc.* 84 (2001) 2705-2706.

[70] D. Carrière, M. Moreau, P. Barboux, J.-P. Boilot, O. Spalla, *Langmuir* 20 (2004) 3449-3455.

[71] M. D. Abramoff, P. J. Magelhaes, S. J. Ram, *Biophotonics International* 11 (2004) 36-42.

[72] U. Kätzel, M. Vorbau, M. Stintz, T. Gottschalk-Gaudig, H. Barthel, *Part. Part. Syst. Charact.* 25 (2008) 19-30.

[73] D. Svergun, *J. Appl. Cryst.* 26 (1993) 258-267.

[74] J. Brunner-Popela, O. Glatter, *J. Appl. Cryst.* 30 (1997) 431-442.

[75] B. Weyerisch, J. Brunner-Popela, O. Glatter, *J. Appl. Cryst.* 32 (1999) 197-209.

[76] J. Brunner-Popela, R. Mittelbach, R. Strey, K.-V. Schubert, E. W. Kaler, O. Glatter, *J. Chem. Phys.* 110 (1999) 10623-10632.

[77] J. S. Pedersen, *Adv. Colloid Interface Sci.* 70 (1997) 171-210.

[78] M. Kotlarchyk, S. H. Chen, *J. Chem. Phys.* 79 (1983) 2461-2469.

[79] J. S. Pedersen, *J. Appl. Cryst.* 27 (1994) 595-608.

[80] G. Beaucage, D. W. Schaefer, *J. Non-Cryst. Solids* 172 (1994) 797-805.

[81] G. Beaucage, *J. Appl. Cryst.* 28 (1995) 717-728.

[82] G. Beaucage, *J. Appl. Cryst.* 29 (1996) 134-146.

[83] S. Trabelsi, A. Janke, R. Hässler, N. E. Zafeiropoulos, G. Fornasieri, S. Bocchini, L. Rozes, M. Stamm, J.-F. Gérard, C. Sanchez, *Macromolecules* 38 (2005) 6068-6078.

[84] A. Rawle, *Surf. Coat. Int.* 86 (2003) 58-65.

[85] J. K. Bailey, M. L. Mecartney, *Colloids Surfaces* 63 (1992) 151-161.

[86] W. D. Pyrz, D. J. Buttrey, *Langmuir* 24 (2008) 11350-11360.

[87] V. M. Gun'ko, V. I. Zarko, R. Leboda, E. Chibowski, *Adv. Colloid Interface Sci.* 19 (2001) 1-112.

[88] A. Aerts, L. R. A. Follens, M. Haouas, T. P. Caremans, M.-A. Delsuc, B. Loppinet, J. Vermant, B. Goderis, F. Taulelle, J. A. Martens, C. E. A. Kirschhock, *Chem. Mater.* 19 (2007) 3448-3454.

[89] M. E. Mackay, A. Tuteja, P. M. Duxbury, C. J. Hawker, B. Van Horn, Z. Guan, G. Chen, R. S. Krishnan, *Science* 311 (2006) 1740-1743.

[90] K. S. W. Sing, D. H. Everett, R. A. W. Haul, L. Moscou, R. A. Pierotti, J. Rouquerol, T. Siemieniewska, *Pure Appl. Chem.* 57 (1985) 603-619.

[91] J. Kohlbrecher, SASfit: http://kur.web.psi.ch/sans1/SANSSoft/sasfit.html

[92] Wolfram Research, Inc., Mathematica, Version 8.0, Champaign, IL (2010).

[93] G. Kickelbick, *Prog. Polym. Sci.* 28 (2002) 83-114.

[94] A. Badia, S. Singh, L. Demers, L. Cuccia, G. R. Brown, R. B. Lennox, *Chem. Eur. J.* 2 (1996) 359-363.

[95] P. Fiurasek, L. Reven, *Langmuir* 23 (2007) 2857-2866.

[96] A. O'Donnell, K. Yach, L. Reven, *Langmuir* 24 (2008) 2465-2471.

[97] C. Yee, G. Kataby, A. Ulman, T. Prozorov, H. White, A. King, M. Rafailovich, J. Sokolov, A. Gedanken, *Langmuir* 15 (1999) 7111-7115.

[98] A. Badia, L. Demers, L. Dickinson, F. G. Morin, R. B. Lennox, L. Reven, *J. Am. Chem. Soc.* 119 (1997) 11104-11105.

[99] M. Fukuto, R. K. Heilmann, P. S. Pershan, A. Badia, R. B. Lennox, *J. Chem. Phys.* 120 (2004) 3446-3459.

References

[100] R. H. Terrill, T. A. Postlethwaite, C.-H. Chen, C.-D. Poon, A. Terzis, A. Chen, J. E. Hutchinson, M. R. Clark, G. Wignall, J. D. Londono, R. Superfine, M. Falvo, C. S. Johnson, E. T. Samulski, R. W. Murray, *J. Am. Chem. Soc.* 117 (1995) 12537-12548.

[101] L. Chen, J. Xu, J. D. Holmes, M. A. Morris, *J. Phys. Chem. C* 114 (2010) 2003-2011.

[102] Y. Min, M. Akbulut, K. Kristiansen, Y. Golan, J. Israelachvili, *Nat. Mater.* 7 (2008) 527-538.

[103] C. D. Bain, G. M. Whitesides, *J. Am. Chem. Soc.* 110 (1988) 6560-6561.

[104] C. D. Bain, G. M. Whitesides, *Science* 240 (1988) 62-63.

[105] C. D. Bain, G. M. Whitesides, *J. Am. Chem. Soc.* 110 (1988) 3665-3666.

[106] C. D. Bain, J. Evall, G. M. Whitesides, *J. Am. Chem. Soc.* 111 (1989) 7155-7164.

[107] C. D. Bain, G. M. Whitesides, *Angew. Chem.* 101 (1989) 522-528.

[108] J. P. Folkers, P. E. Laibinis, G. M. Whitesides, *Langmuir* 8 (1992) 1330-1341.

[109] P. E. Laibinis, R. G. Nuzzo, G. M. Whitesides, *J. Phys. Chem.* 96 (1992) 5097-5105.

[110] M. C. Prado, B. R. A. Neves, *Langmuir* 26 (2010) 648-654.

[111] E. Glogowski, J. He, T. P. Russell, T. Emrick, *Chem. Commun.* (2005) 4050-4052.

[112] S. Kubowicz, J. Daillant, M. Dubois, M. Delsanti, J.-M. Verbavatz, H. Mohwald, *Langmuir* 26 (2010) 1642-1648.

[113] A. Rezaee, L. C. Pavelka, S. Mittler, *Nanoscale Res. Lett.* 4 (2009) 1319-1323.

[114] Y.-C. Lin, B.-Y. Yu, W.-C. Lin, S.-H. Lee, C.-H. Kuo, J.-J. Shyue, *J. Colloid Interface Sci.* 340 (2009) 126-130.

[115] C. Gentilini, L. Pasquato, *J. Mater. Chem.* 20 (2010) 1403-1412.

[116] Y. Sahoo, H. Pizem, T. Fried, D. Golodnitsky, L. Burstein, C. N. Sukenik, G. Markovich, *Langmuir* 17 (2001) 7907-7911.

[117] W. Gao, L. Dickinson, C. Grozinger, F. G. Morin, L. Reven, *Langmuir* 12 (1996) 6429-6435.

156

[118] W. Gao, L. Dickinson, C. Grozinger, F. G. Morin, L. Reven, *Langmuir* 13 (1997) 115-118.

[119] B. Feichtenschlager, C. Lomoschitz, G. Kickelbick, *J. Colloid Interface Sci.* 360 (2011) 15-25.

[120] B. Feichtenschlager, PhD thesis, Vienna University of Technology (2011).

[121] W. G. Golden, C. D. Snyder, B. Smith, *J. Phys. Chem.* 86 (1982) 4675-4678.

[122] R. G. Snyder, H. L. Strauss, C. A. Ellinger, *J. Phys. Chem.* 86 (1982) 5145-5150.

[123] R. Helmy, A. Y. Fadeev, *Langmuir* 18 (2002) 8924-8928.

[124] M. Salmeron, *Tribol. Lett.* 10 (2001) 69-79.

[125] M. L. Schilling, H. E. Katz, S. M. Stein, S. F. Shane, W. L. Wilson, S. B. Ungashe, G. N. Taylor, T. M. Putvinski, C. E. D. Chidsey, S. Buratto, *Langmuir* 9 (1993) 2156-2160.

[126] J. T. Woodward, A. Ulman, D. K. Schwartz, *Langmuir* 12 (1996) 3626-3629.

[127] D. Francová, G. Kickelbick, *Monatsh. Chem.* 14 (2009) 413-422.

[128] D. M. Spori, N. V. Venkataraman, S. G. P. Tosatti, F. Durmaz, N. D. Spencer, S. Zuercher, *Langmuir* 23 (2007) 8053-8060.

[129] D. A. Offord, J. H. Griffin, *Langmuir* 9 (1993) 3015-3025.

[130] B. Vercelli, G. Zotti, G. Schiavon, S. Zecchin, A. Berlin, *Langmuir* 19 (2003) 9351-9356.

[131] A. Badia, L. Cuccia, L. Demers, F. Morin, R. B. Lennox, *J. Am. Chem. Soc.* 119 (1997) 2682-2692.

[132] A. J. Crosby, J.-Y. Lee, *Polym. Rev.* 47 (2007) 217-229.

[133] A. C. Balazs, T. Emrick, T. P. Russell, *Science* 314 (2006) 1107-1110.

[134] G. Kickelbick, U. Schubert, *Monatsh. Chem.* 132 (2001) 13-30.

[135] F. R. Kogler, T. Koch, H. Peterlik, S. Seidler, U. Schubert, *J. Polym. Sci.: Part B: Polym. Phys.* 45 (2007) 2215-2231.

[136] C. Chevigny, F. Dalmas, E. Di Cola, D. Gigmes, D. Bertin, F. Boué, J. Jestin, *Macromolecules* 44 (2011) 122-133.

References

[137] M. M. Demir, P. Castignolles, Ü. Akbey, G. Wegner, *Macromolecules* 40 (2007) 4190-4198.

[138] A.-S. Robbes, J. Jestin, F. Meneau, F. Dalmas, O. Sandre, J. Perez, F. Boué, F. Cousin, *Macromolecules* 43 (2010) 5785-5796.

[139] P. J. Costanzo, F. L. Beyer, *Macromolecules* 40 (2007) 3996-4001.

[140] N. Jouault, F. Dalmas, S. Said, E. Di Cola, R. Schweins, J. Jestin, F. Boué, *Macromolecules* 43 (2010) 9881-9891.

[141] A. Camenzind, T. Schweizer, M. Sztucki, S. E. Pratsinis, *Polymer* 51 (2010) 1796-1804.

[142] P. S. Chinthamanipeta, S. Kobukata, H. Nakata, D. A. Shipp, *Polymer* 49 (2008) 5636-5642.

[143] R. Krishnamoorti, R. A. Vaia, *J. Polym. Sci., Part B: Polym. Phys.* 45 (2007) 3252-3256.

[144] V. V. Ginzburg, *Macromolecules* 38 (2005) 2362-2367.

[145] H. Liu, D. Liu, F. Yao, Q. Wu, *Bioresource Technology* 101 (2010) 5685-5692.

[146] Y. Hu, G. Gu, S. Zhou, L. Wu, *Polymer* 52 (2011) 122-129.

[147] J. A. Johnson, D. W. Jones, *J. Mater. Sci.* 29 (1994) 870-876.

[148] D. Shaosheng, W. Yuezhen, Z. Zhiqian, *J. Appl. Polym. Sci.* 72 (1999) 1335-1339.

[149] K. Matsuyama, K. Mishima, *J. Supercrit. Fluids* 49 (2009) 256-264.

[150] L. Shanghua, *Nanotechnology* 20 (2009) 185607.

[151] F. Bellezza, A. Cipiciani, M. A. Quotadamo, *Langmuir* 21 (2005) 11099-11104.

[152] K. Ikemura, T. Endo, *Dent. Mater. J.* 29 (2010) 109-121.

[153] C. A. Traina, J. Schwartz, *Langmuir* 23 (2007) 9158-9161.

[154] Z. Wu, H. Han, W. Han, B. Kim, H. Ahn Kyung, K. Lee, *Langmuir* 23 (2007) 7799-7803.

[155] P. Kohli, G. J. Blanchard, *Langmuir* 19 (2000) 695-701.

[156] G. Busca, G. Ramis, V. Lorenzelli, P. F. Rossi, A. La Ginestra, P. Patrono, *Langmuir* 5 (1989) 911-916.

158

[157] M. Kamibayashi, H. Ogury, Y. Otsuba, *J. Colloid Interface Sci.* 321 (2008) 294-301.

[158] Y. Hu, S. Zhou, L. Wu, *Polymer* 50 (2009) 3609-3613.

[159] T. M. Cornsweet, *Science* 168 (1970) 433-438.

[160] O. Becker, G. P. Simon, *Adv. Polym. Sci.* 179 (2005) 29-82.

[161] H. Althues, J. Henle, S. Kaskel, *Chem. Soc. Rev.* 36 (2007) 1454-1465.

[162] R. Medina, F. Haupert, A. K. Schlarb, *J. Mater. Sci.* 43 (2008) 3245-3252.

[163] H. Li, Z. Zhang, X. Ma, M. Hu, X. Wang, P. Fan, *Surf. Coat. Technol.* 201 (2007) 5269-5272.

[164] C. Chen, A. B. Morgan, *Polymer* 50 (2009) 6265-6273.

[165] Y. Zheng, K. Chonung, G. Wang, P. Wei, P. Jiang, *J. Appl. Polym. Sci.* 111 (2009) 917-927.

[166] S. Kang, S. I. Hong, C. R. Choe, M. Park, S. Rim, J. Kim, *Polymer* 42 (2000) 879-887.

[167] L. Mascia, L. Prezzi, B. Haworth, *J. Mater. Sci.* 41 (2006) 1145-1155.

[168] R. Zhao, W. Luo, *Mater. Sci. Eng.* A483-A484 (2008) 313-315.

[169] Y.-C. Chiu, L. Riang, I. C. Chou, C.-C. M. Ma, C.-L. Chiang, C.-C. Yang, *J. Polym. Sci. Part B: Polym. Phys.* 48 (2010) 643-652.

[170] Y. Imai, A. Terahara, Y. Hakuta, K. Matsui, H. Hayashi, N. Ueno, *Eur. Polym. J.* 45 (2009) 630-638.

[171] M. Ochi, D. Nii, Y. Suzuki, M. Harada, *J. Mater. Sci.* 45 (2010) 2655-2661.

[172] P. F. Bruins, *Epoxy Resin Technology*, John Wiley and Sons, New York (1968).

[173] I. M. Kalogeras, A. Vassilikou-Dova, I. Christakis, D. Pietkiewicz, W. Brostow, *Macromol. Chem. Phys.* 207 (2006) 879-892.

[174] M. Szekeres, O. Kamalin, R. A. Schoonheydt, K. Wostyn, K. Clays, A. Persoons, I. Dekany, *J. Mater. Chem.* 12 (2002) 3268-3274.

[175] J. H. Koo, *Polymer Nanocomposites, Processing, Characterization and Applications*, ed by M. Omar, McGraw-Hill Publishers, New York (2006) 51-52.

[176] B. M. Novak, *Adv. Mat.* 5 (1993) 422-433.

References

[177] C. Chen, R. S. Justice, D. W. Schaefer, J. W. Baur, *Polymer* 49 (2008) 3805-3815.

[178] Y. L. Liu, C. Y. Hsu, W. L. Wei, R. J. Jeng, *Polymer* 44 (2003) 5159-5167.

[179] H. L. Tyan, Y. C. Liu, K. H. Wei, *Polymer* 40 (1999) 4877-4886.

[180] M. Saric, H. Dietsch, P. Schurtenberger, *Coll. Surf. A* 291 (2006) 110-116.

[181] D. J. Chaiko, *Chem. Mater.* 15 (2003) 1105-1110.

[182] K. Esumi, K. Ishizuki, H. Otsuka, M. Ono, S. Ichikawa, C. J. Yanase, *Coll. Interface Sci.* 178 (1996) 549-554.

[183] A. Sánchez-Ferer, M. R. Reufer, P. Schurtenberger, H. Dietsch, *Nanotechnology* 21 (2010) 185603.

[184] Y. G. Aronoff, B. Chen, G. Lu, C. Seto, J. Schwartz, S. L. Bernasek, *J. Am. Chem. Soc.* 119 (1997) 259-262.

[185] A. J. Kinloch, R. D. Mohammed, A. C. Taylor, C. Eger, S. Sprenger, D. Egan, *J. Mater. Sci.* 40 (2005) 5083-5086.

[186] H. Miyagawa, M. J. Rich, L. T. Drzal, *J. Polym. Sci. Part B: Polym. Phys.* 42 (2004) 4384-4390.

[187] D. Holzinger, G. Kickelbick, *Chem. Mater.* 15 (2003) 4944-4948.

[188] P. Rittigstein, R. D. Priestley, L. J. Broadbelt, J. M. Torkelson, *Nat. Mater.* 6 (2007) 278-282.

[189] G. Krueger, *Coating* 39 (2006) 169-171.

[190] G. Krueger, *Coating* 39 (2006) 113-115.

[191] M. Litschauer, M. A. Neouze, *J. Mater. Chem.* 18 (2008) 640-646.

[192] L. Arleth, J.S. Pedersen, *Phys. Rev. E* 63 (2001) 061406.

[193] F. Brodard-Severac, G. Guerrero, J. Maquet, P. Florian, C. Gervais, P. H. Mutin, *Chem. Mater.* 20 (2008) 5191-5196.

[194] Y. Sun, Z. Zhang, K. S. Moon, C. P. Wong, *J. Polym. Sci. Part B: Polym. Phys.* 42 (2004) 3849-3858.

[195] Y. M. Cao, J. Sun, D. H. Yu, *J. Appl. Polym. Sci.* 83 (2002) 70-77.

[196] B. J. Ash, L. S. Schadler, R. W. Siegel, *Mater. Lett.* 55 (2002) 83-87.

[197] C. S. Triantafillidis, P. C. LeBaron, T. J. Pinnavaia, *Chem. Mat.* 14 (2002) 4088-4095.

[198] O. Becker, R. J. Varley, G. P. Simon, *Polymer* 43 (2002) 4365-4373.

[199] G. C. Huang, J. K. Lee, *Composites, Part A* 41 (2010) 473-479.

[200] A. C. Balazs, T. Emrick, T. P. Russell, *Science* 314 (2006) 1107-1110.

[201] W. L. Wu, B. J. Bauer, W. Su, *Polymer* 30 (1989) 1384-1388.

[202] J. S. Chen, M. D. Poliks, C. K. Ober, Y. Zhang, U. Wiesner, E. Giannelis, *Polymer* 43 (2002) 4895-4904.

[203] W. R. Caseri, *Mater. Sci. Technol.* 22 (2006) 807-817.

[204] D. E. Alexander, E. Gong, L. D. Martin, D. A. Burnham, A. R. Falk, *PNAS* 107 (2010) 2972-2976.

[205] M. J. Benton, *Nature* 463 (2010) 306-307.

[206] J. Ruben, *PNAS* 107 (2010) 2733-2734.

[207] R. Stone, *Science* 327 (2010) 508-508.

[208] C. Sullivan, D. W. E. Hone, X. Xu, and F. Zhang, *Proc. R. Soc. Lond. B* 277 (2010) 2027-2033.

[209] L. Eckhart, L. Dalla Valle, K. Jaeger, C. Ballaun, S. Szabo, A. Nardi, M. Buchberger, M. Hermann, L. Alibardi, E. Tschachler, *PNAS* 105 (2008) 18419-18423.

[210] W. T. Astbury, H. J. Woods, *Phil. Trans. R. Soc. Lond. A* 232 (1934) 333-394.

[211] I. M. Weiss, H. O. K. Kirchner, *J. Exp. Zool. Part A* 313A (2010) 690-703.

[212] L. Dalla Valle, A. Nardi, P. Belvedere, M. Toni, L. Alibardi, *Developmental Dynamics* 236 (2007) 1939-1953.

[213] I. J. O'Donnell, A. S. Inglis, *Aust. J. Biol. Sci.* 27 (1974) 369-382.

[214] B. Busson, P. Engstrom, J. Doucet, *J. Synchrotron Radiat.* 6 (1999) 1021-1030.

[215] R. D. B. Fraser, D. A. D. Parry, *J. Struct. Biol.* 162 (2008) 1-13.

[216] W. T. Astbury, E. Beighton, *Nature* 191 (1961) 171-173.

[217] R. Schor, S. Krimm, *Biophys. J.* 1 (1961) 467-487.

References

[218] R. Schor, S. Krimm, *Biophys. J.* 1 (1961) 489-515.

[219] R. D. B. Fraser, D. A. D. Parry, *Int. J. Biol. Macromol.* 19 (1996) 207-211.

[220] G. J. Cameron, T. J. Wess, R. H. C. Bonser, *J. Struct. Biol.* 143 (2003) 118-123.

[221] J. Harford, J. Squire, *Rep. Progr. Phys.* 60 (1997) 1723-1787.

[222] I. M. Weiss, H. O. K. Kirchner, *Adv. Eng. Mat.* 12 (2010) 412-416.

[223] I. M. Weiss, K. P. Schmitt, H. O. K. Kirchner, *J. Exp. Zool.* 315 (2011) 266-273.

[224] F. Vollrath, D. Porter, *Polymer* 50 (2009) 5623-5632.

[225] S. Keten, Z. Xu, B. Ihle, M. J. Buehler, *Nat. Mater.* 9 (2010) 359-367.

[226] J. M. Gosline, P. A. Guerette, C. S. Ortlepp, K. N. Savage, *J. Exp. Biol.* 202 (1999) 3295-3303.

Acknowledgement

I am deeply indebted to Prof. Herwig Peterlik for his considerate supervision, for the challenge and the sedolous support as well as all the helpful discussions and suggestions to realize this thesis.

My thanks go to my colleagues from the project:

Bernhard Feichtenschlager, for the good teamwork and for his many ideas of improving the materials and getting the best possible results. Guido Kickelbick for his sedulous input to get the best out of our work. Muhammad Sajjad and Thomas Koch, for doing the mechanical experiments and interpreting the multifaceted results.

Support by the Austrian Science Fund (FWF - Projectno. 20963) is acknowledged. I also want to thank Prof. Schubert for the possibility to work for the Institute of Materials Chemistry at the Vienna University of Technology.

Further words of gratitude go to my working group:

Stephan Puchegger, for his help concerning computational problems and his support evaluating the data from the peacock feather. Not to forget his contribution for improving the taste of tea. Johanna Akbarzadeh, for all the conversations during work and the company during our journeys to schools and conferences (as well as visiting the conference locations). Daniel Gitschthaler and Martina Rohrer, who supported me when having technical or chemical questions. Yvonne Simon for her help and support concerning all organizational questions. Furthermore, my other colleagues from the working group: Ewa, Fritz, Robert, Manuel and Markus.

Special thanks go to my friends and my family:

My dear co-conspirators Barbara, Claudia, Daniela, Fabienne and Gabriele ($\varphi\alpha\kappa$), for all discussions about new fundamental theories concerning life, the universe and everything. Thanks to the pub- and the physicist-"Stammtisch" for numerous discussions during the lunch time and in the evening.

I want to thank my mother for her great support, her patience and helpful company during the last years as well as my whole family for their curiosity in my work. And I want to thank my brother for keeping me up to date with the latest news.

My sincere thank to Christian for his help, his support and for being a part of my life.

Curriculum Vitae

Mag. Silvia Pabisch, Bakk.

Date of birth: 01.03.1983
Place of birth: Waidhofen/Thaya, Austria
Nationality: Austria
Tel.No.:   0043 (0)1 4277 51359
Email: silvia.pabisch@univie.ac.at

Education

09/1997 – 06/2002:	Higher level secondary commercial college, Bundeshandelsakademie Waidhofen/Thaya
10/2002 – 04/2006:	Bachelor student of astronomy, University of Vienna
04/2006:	Bakk. rer. nat. (Astronomy), University of Vienna
10/2003 – 08/2008:	Student of physics, University of Vienna Diploma thesis at the working group Dynamic of condensed systems: Orientation of mesoporous structures
08/2008:	Mag. rer. nat. (Physics), University of Vienna
09/2008 – dato:	Doctoral thesis at the University of Vienna: Increased structural order in nanocomposites: From weakly linked nanoparticles in polymers to highly cross-linked strands in feather keratin

Work experience

03/2006 – 06/2006:	Kaczek Visuals Trading GesmbH: Project staff
04/2007 – 05/2007:	Dynamics of condensed systems, University of Vienna: FWF Project scientist
01/2008 – 03/2008:	Dynamics of condensed systems, University of Vienna: Scientific staff
09/2008 – 08/2010:	Dynamics of condensed systems, University of Vienna: FWF Project scientist
09/2010 – 11/2010:	Dynamics of condensed systems, University of Vienna: Scientific staff
12/2010 – 11/2011:	Institute of Materials Chemistry, Vienna University of Technology: FWF Project scientist
03/2011 – 08/2011:	Supervisor of the course "UE Solid State Physics II – Exercises"
12/2011 – dato:	Dynamics of condensed systems, University of Vienna: FWF Project scientist

Scientific conferences

- 58th ÖPG annual meeting, Leoben, Austria, September 2008
  Poster: Orientation of mesoporous structures
  Poster price 2008

- Joint annual meeting of SPS and ÖPG, Innsbruck, Austria, September 2009
  Poster: Structural characterization of surface-functionalized nanoparticles and nanocomposites by SAXS

- 5th European Silicon Days, Vienna, Austria, September 2009
  Poster: Orientation of mesoporous structures

- Strategic Workshop on Principles and Development of Bio-inspired Materials, Vienna, Austria, April 2010
  Poster: Position-resolved structure of peacock feathers during growth – an X-ray diffraction study

- Materials Science and Engineering, Darmstadt, Germany, August 2010
  Talk: Orientation of mesoporous structures

- 60th ÖPG annual meeting, Salzburg, Austria, September 2010
  Poster: Surface-functionalized nanoparticles in polymer nanocomposites

- 14th International Scientific Conference on Polymeric Materials, Halle (Saale), Germany, September 2010
  Talk: Influence of surface-functionalized nanoparticles on the structural properties of polymer nanocomposites

- 4th Wiener Biomaterialsymposium, Vienna, Austria, November 2010
  Poster: Strukturuntersuchung von beta-Keratin entlang einer Pfaufeder mittels Röntgenkleinwinkelstreuung

- 75th Annual Meeting of the DPG and DPG Spring Meeting, Dresden, Germany, March 2011
  Talk: The structure of keratin in the tail feathers of peacocks

- Joint annual meeting of SPS and ÖPG, Lausanne, Switzerland, June 2011
  Talk: How coupling agent ordering on the surface of zirconia nanocrystals influences their agglomeration

- Euromat 2011, Montpellier, France, September 2011
  Talk: The structure of keratin in the tail feathers of peacocks – an X-ray diffraction study

Publications

- M. Bendova, M. Puchberger, S. Pabisch, H. Peterlik, U. Schubert, *European Journal of Inorganic Chemistry* **2010,** 15, 2266-2275.
Studies on the formation of CdS Nanoparticles from solutions of (NMe4)4[Cd10S4(SPh)16

- S. Pabisch, S. Puchegger, H. O. K. Kirchner, I. M. Weiss, H. Peterlik, *Journal of Structural Biology* **2010**, 172, 270-275.
Keratin homogeneity in the tail feathers of Pavo cristatus and Pavo cristatus mut alba

- S. Pabisch, B. Feichtenschlager, G. Kickelbick, H. Peterlik*, Conference proceedings Polymeric Materials 2010*, **2010**, Halle.
Influence of surface-functionalized nanoparticles on the structural properties of polymer nanocomposites

- M. Sajjad, B. Feichtenschlager, S. Pabisch, T. Koch, S. Seidler, H. Peterlik, G. Kickelbick, *Conference proceedings Polymeric Materials 2010*, **2010,** Halle.
Properties of SiO2/Epoxy – and ZrO2/Epoxy – nanocomposites

- M. Sajjad, B. Feichtenschlager, S. Pabisch, J. Svehla, T. Koch, S. Seidler, H. Peterlik, G. Kickebick, *Polymer International* **2012**, 61, 274-285.
Zirconia and silica nanoparticles as fillers in epoxy resin matrix - the effect of concentration, size and surface chemistry on the bulk properties of nanocomposites

- J. Svehla, S. Pabisch, B. Feichtenschlager, D. Holzmann, H. Peterlik, G. Kickelbick, *Macromolecular Materials and Engineering* **2012**, in print, DOI: 10.1002/mame.201100191 .
Polyester Preparation in the Presence of Pristine and Phosphonic-Acid-Modified Zirconia Nanopowders

- S. Pabisch, B. Feichtenschlager, G. Kickelbick, H. Peterlik, *Chemical Physics Letters* **2012**, 512, 91-97.
Effect of interparticle interactions on size determination of zirconia and silica based systems - A comparison of SAXS, DLS, BET, XRD and TEM

- B. Feichtenschlager, S. Pabisch, H. Peterlik, G. Kickelbick, *Langmuir* **2012**, in print, DOI: 10.1021/la2023067 .
Nanoparticle Assemblies as Probes for Self Assembled Monolayer Characterization: The Correlation between Surface Functionalization and Agglomeration Behavior

- J. Geserick, S. Meyer, M. Puchberger, S. Pabisch, H. Peterlik, O. Bethge, E. Bertagnolli, U. Schubert*, Journal of Materials Chemistry*, submitted
Porous Silica-based Mixed Oxides with Basic Organic Sites Prepared by Sequential Non-Hydrolytic and Hydrolytic Sol-gel Processes

Curriculum Vitae